UC Davis
UC Davis Electronic Theses and Dissertations

Title

Structural Characterization and Physical Properties of Superconducting LaNiGa2 and Antiferromagnetic CeIn3

Permalink

https://escholarship.org/uc/item/6sz539tw

Author

Badger, Jackson Robert

Publication Date

2021

Peer reviewed|Thesis/dissertation

Structural Characterization and Physical Properties of Superconducting LaNiGa$_2$ and Antiferromagnetic CeIn$_3$

By

JACKSON ROBERT BADGER
DISSERTATION

Submitted in partial satisfaction of the requirements for the degree of

DOCTOR OF PHILOSOPHY

in

Chemistry

in the

OFFICE OF GRADUATE STUDIES

of the

UNIVERSITY OF CALIFORNIA

DAVIS

Approved:

_____

Valentin Taufour, Ph.D., Chair

_____

Susan Kauzlarich, Ph.D.

_____

Jesús Velázquez, Ph.D.

2021

i

For always believing in me,
this dissertation is dedicated to my grandmother, Dede
May she rest and always be remembered

"Courage"
- Roger Bennett

Contents

List of Figures

Abstract

In this dissertation, I will describe two experimental studies on two different condensed matter systems. The first study originates from our crystallographic findings on $LaNiGa_2$. After developing a single crystal synthesis method, single-crystal X-ray diffraction results improve upon previous studies by showing that $LaNiGa_2$ crystallizes in a $Cmcm$ unit cell instead of a $Cmmm$ one. As a result of uncovering nonsymmorphic symmetry operations, we show that these directly result in two topological features precisely at the Fermi level. With the previous knowledge that $LaNiGa_2$ breaks time-reversal symmetry within its superconducting state and shows evidence for multi-gap superconducting behavior, we can then directly connect the new crystallographic results, the topological features, and the unique superconducting state.

In the second study, we synthesize and then characterize single crystals of Nd substituted $CeIn_3$. This well-studied heavy-fermion system has previously exhibited fascinating phenomena as its antiferromagnetic ordering is systematically suppressed. In $Ce_{1-x}Nd_xIn_3$ we reveal an interesting interplay between the Kondo lattice coherence and crystal electric field depopulation effects. Wherein we can separate the two features in electrical resistivity measurements in the most disordered substitution range of $x = 0.4 - 0.5$. We also reveal a comprehensive phase diagram between the two antiferromagnetic ordering.

In addition to these two studies, I also provide an overview of relevant concepts and experimental techniques. The purpose of this overview is to provide incoming graduate students a starting point to begin to understand what principles are relevant to the condensed matter systems discussed in this dissertation and how to perform specific experimental techniques to study said principles. Within the experimental section, I also provide some "experimentalist's insights" on the techniques I have used extensively throughout my graduate work.

Acknowledgements

I would like to first start by thanking Valentin Taufour. I am forever grateful to you for accepting me into your group and allowing me to work in and help build out the lab. Since that time, you have always been highly supportive of me and taught me so much. I am also incredibly grateful for your patience because you had to explain so much, and often multiple times, to me since I have not taken a physics course since my freshman year of undergrad. I know I am your first Ph.D. graduate student, but I certainly know that many more are to follow because of your tutelage. I am excited to build out the Taufour alumni network!

Secondly, I would like to thank Peter Klavins. I always thought of you as a dear mentor to me, and I will cherish those times we spent trying to fix random broken things in the lab. You also showed me that there is always some fun to be had in the lab, despite things not working the way they are supposed to.

I would also like to thank my committee, Susan Kauzlarich and Jesús Velázquez. I am very grateful for your support when I chose to work in Valentin's group in the Physics department. Especially Susan for allowing me to 'join' your group while Valentin's paperwork to join the chemistry graduate group was sifting through the bureaucracy.

Thank you to everyone within the Taufour group for the constructive and informative conversations, especially Rahim. When you all asked me questions, I may have seemed

grumpy at certain times, but I always thoroughly enjoyed taking the time to teach, help you, and learn from you all.

Thank you to everyone within the UC-Davis chemistry department for your varied support throughout the years. Especially Brad Wolf for answering all of my random questions and being a good friend.

Thank you for the good memories to everyone I shared a beer with throughout my time at UC-Davis. Here's to more beers and fun times in the future.

I would also like to thank my family — Mom, Dad, Carson, Macklan, Bob, and cousins — for their eternal support and belief that I could finish my doctoral degree. I certainly would not have been able to complete this work without it.

Lastly, thank you, Kelly Boudwin. Thank you for initially supporting and loving me from afar and then deciding that Sacramento was a fun spot to live. The last couple of years living in Sacramento with you have been some of my favorites, despite the pandemic. Every day with you is an utter joy, and I am looking forward to our life without graduate school.

This dissertation contains two works that are currently under review. But some of the work that I will present has been published in the following articles:

- K. P. Devlin, N. Kazem, J. V. Zaikina, J. A. Cooley, J. R. Badger, J. C. Fettinger, V. Taufour, and S. M. Kauzlarich. $Eu_{11}Zn_4Sn_2As_{12}$: A Ferromagnetic Zintl Semiconductor with a Layered Structure Features Extended Zn_4As_6 Sheets and Ethane-like Sn_2As_6 Units. Chemistry of Materials **30**, 7067 (2018).

- H. Jin, J. Badger, P. Klavins, J.-T. Zhao, and V. Taufour. Stabilization of $CeGe_3$ with Ti and O featuring tetravalent Ce ions: $(Ce_{0.85}Ti_{0.15})Ge_3O_{0.5}$. Journal of Alloys and Compounds **863**, 158354 (2021).

- I. Vinograd, S. P. Edwards, Z. Wang, T. Kissikov, J. K.Byland, J. R. Badger, V. Taufour, and N. J. Curro. Inhomogeneous Knight shift in vortex cores of superconducting FeSe. Phys. Rev. B **104**, 014502 (2021).

Other published manuscripts that I have worked on but are not mentioned in this dissertation:

- M. Marple, J. Badger, I. Hung, Z. Gan, K. Kovnir, and S. Sen. Structure of Amorphous Selenium by 2D ^{77}Se NMR Spectroscopy: An End to the Dilemma of Chain versus Ring. Angewandte Chemie International Edition **56**, 9777 (2017).

- C. J. Perez, K. P. Devlin, C. M. Skaggs, X. Tan, C. E. Frank, J. R. Badger, C.-J. Kang, T. J. Emge, S. M. Kauzlarich, V. Taufour, G. Kotliar, S. H. Lapidus, and M. Greenblatt. Measured and simulated thermoelectric properties of $FeAs_{2-x}Se_x$ ($x = 0.30 - 1.0$): from marcasite to arsenopyrite structure. Mater. Adv. **1**, 1390 (2020).

- Z. E. Brubaker, J. S. Harvey, J. R. Badger, R. R. Ullah, D. J. Campbell, Y. Xiao, P. Chow, C. Kenney-Benson, J. S. Smith, C. Reynolds, J. Paglione, R. J. Zieve, J. R.Jeffries, and V. Taufour. Pressure-induced suppression of ferromagnetism in itinerant ferromagnet $LaCrSb_3$. Phys. Rev. B **101**, 214408 (2020).

Chapter 1

Introduction

The past century and a half of human history have been scattered with technological developments that have rapidly progressed society. Many of these technologies have allowed humanity to prosper and to achieve extraordinary feats. More specifically, novel technologies have allowed our capabilities to expand exponentially and beyond our wildest imaginations within the Information Age. For example, the computational power behind the pinnacle of scientific and engineering achievement, the Apollo missions to the moon, is now dwarfed by the computational power within your average mobile phone [1]. Therefore discovering and understanding these new technologies is vital to the continued development of our society as a whole. Furthermore, as highlighted by a 2011 United States Department of Energy report, this progress is especially critical towards curbing anthropogenic climate change [2].

These novel technological developments are driven by the discovery of new materials and unique condensed matter states. As evidence by the fact that the aforementioned average mobile phone now contains at least 70 of the 83 nonradioactive stable elements [3]. The metals that make smartphones "smart" are mostly rare-earth metals (yttrium, scandium, and the lanthanides). These metals not only allow us to have access to the internet at our

fingertips, but materials with these elements are also found throughout society in televisions, computers, head-phones, and other such modern-day 'necessities.' As a result, discovering new materials containing these elements and comprehensively understanding the fundamental principles behind such systems, will continue to progress technology and society forward.

At a fundamental level, this work is best accomplished from an interdisciplinary perspective. Wherein experts across various fields collaborate to use their knowledge to elucidate every aspect of an exotic system. Generally, this works by solid-state chemists discovering new materials and performing experiments to learn about the structural and physical properties. Condensed matter physicists follow up this work by conducting high-level experiments to better understand fundamental principles behind the more unique systems. And then, materials scientists lead the charge behind uncovering the practical properties of the most promising materials. Overall, as our collective understanding of specific characteristics and materials continues to grow, we can bridge the experimental results with comprehensive microscopic models that can accommodate and predict every detail of the state. With these models, we can then drive technological advances. Today this is most evident in the ongoing development towards discovering and understanding "quantum materials" like those used in fault-tolerant quantum computing systems.

This dissertation will describe two experiments where I use my background as a chemist to better understand two vastly different condensed matter systems. The first pertains $LaNiGa_2$. Previous work on polycrystalline $LaNiGa_2$ revealed that the superconducting state broke time-reversal symmetry - a rare phenomenon only observed in ~ 25 known systems [4]. Additionally, the superconducting state showed evidence for multi-gap behavior. Our discovery of a single-crystal synthesis route shows that previous structural work on $LaNiGa_2$ was incorrect. And that with this new structural information, we can tie together

the unique properties of the unconventional superconducting state. I also provide an outlook about how our work can be employed to discover future materials with similar properties.

The second project is about Nd substituted $CeIn_3$. This well-studied heavy fermion system has shown fascinating phenomena as its antiferromagnetic ordering is suppressed with hydrostatic pressure, magnetic fields, and/or chemical substitution. We show that by systematically substituting Nd into the parent compound, we can separate the Kondo lattice coherence features and the crystal electric field (CEF) depopulation effects. Thus far, this behavior has never been observed in any study on $CeIn_3$ nor the related $CeMIn_5$.

Before diving into the two projects, I first start by describing fundamental principles related to each material. Then I dive into specific experimental details about how to grow single crystals, obtain structural properties, and perform some physical property measurements.

Chapter 2

Background of Concepts

Copyright permission has been obtained and granted to use figures 2.2(a), 2.5, 2.6, 2.7, 2.8, 2.10, 2.13, 2.14(b), and 2.15. Figures 2.3, 2.9, 2.12, and 2.14(a) were obtained from open access sources.

2.1 Concepts related to LaNiGa$_2$

2.1.1 Unconventional Superconductivity

Superconductivity has been hotly studied for over a century, and numerous people have dedicated their entire careers towards uncovering all of the intricacies of this phenomenon. Consequently, the topic is vast with countless books and articles dedicated to explaining all the nuances ranging from physical properties to microscopic theories. To begin to understand unconventional superconductivity we must first understand conventional superconductivity. Here I first start by briefly covering BCS theory (named after the authors John Bardeen, Leon Cooper, and Robert Schrieffer) and then cover the basics of unconventional superconductiv-
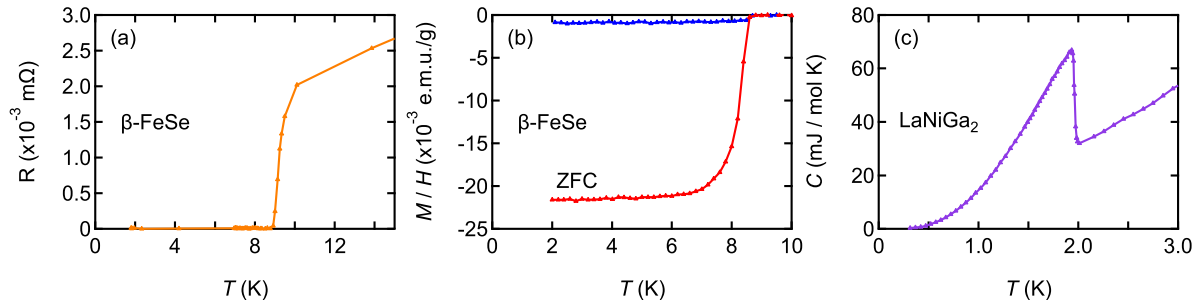
Figure 2.1: Experimental signatures of superconductors. (a) Electrical resistivity ($\rho(T)$) measurement on β-FeSe shows when the resistance drops to zero. (b) Magnetic susceptibility ($M(T)/H$) measurements (ZFC and FC) on β-FeSe that show the diamagnetic response when the external magnetic field is expelled. (c) Heat capacity ($C(T)$) measurement on LaNiGa$_2$ which shows the second-order phase transition. Despite both β-FeSe and LaNiGa$_2$ being unconventional superconductors, all superconductors show these essential experimental signatures.

ity. More can be read about other complexities from superconductivity (both conventional and unconventional) in [5, 6].

From a historical standpoint, the first superconductors discovered were basic elements such as mercury, tin, and niobium [6]. Elemental superconductors were discovered because they exhibited three main phenomena upon entering the superconducting state: exhibited zero electrical resistance, expelled small external magnetic fields (Meissner effect), and displayed a second-order phase transition. Subsequently, new superconductors could be identified by observing each of these phenomena through different experimental techniques: electrical resistivity measurements can show the sharp drop to zero resistance, magnetic susceptibility measurements can reveal the superconductor to exhibit a diamagnetic response by expelling the external magnetic field, and thermodynamic heat capacity measurements can show the second-order phase transition at the critical temperature, T_{sc}. All of these experimental signatures are shown in Fig. 2.1 and 3.23.

After these physical characteristics were discovered, many theoreticians started to develop

5

microscopic theories to cohesively explain this unique state. Eventually, this led to BCS theory and the establishment of 'conventional superconductivity' [7]. This theory built off of previous discoveries and models and eventually led John Bardeen, Leon Cooper, and John Robert Schrieffer to collectively win the Nobel Prize in Physics. The BCS theory established that upon a material entering the superconducting state, an energy gap opens near the Fermi level (Fig. 2.2). This energy gap differs in nature from an insulator's energy gap because the gap occurs due to the electron-lattice interactions in an insulator. In a superconductor, however, the energy gap opens because of the condensation of electron-electron pairing.

BCS theory explains that this electron-electron coupling occurs indirectly through phonon-mediated channels. When electrons pair (Cooper pairs), a small energy gap opens up and makes the superconducting ground state more energetically favorable. Since electrons are fermions, the pairs must anticommute either through the spin or orbital channel. The BCS ground state has spin-singlet Cooper pairs between electrons of opposite spin and wavevectors: $(k \uparrow, -k \downarrow)$. Consequently, the antisymmetric spin-singlet state is also accompanied by a symmetrical orbital wave function to preserve the antisymmetry of the total wave function. This pairing symmetry leads to a total angular momentum of $L = 0$. Which then gives rise to the colloquial name s-wave pairing for BCS superconductors [8]. Outside of successfully explaining all aspects of BCS superconductors, another lasting consequence of this theory is that it established the importance of electron-electron pairing and the associated Cooper pairing and energy gap symmetry.

One effect of BCS theory was that the energy gap (Δ) was found to be isotropic (nodeless) in k-space and that the temperature dependence of the gap function $\Delta(t)$ ($t = T/T_{\text{sc}}$) should be the same for each conventional superconductor (Fig. 2.2) [7]. Consequently all conventional superconductors must have a BCS gap of $2\Delta/k_B T_{\text{sc}} = 1.76$ [5, 7]. Since the
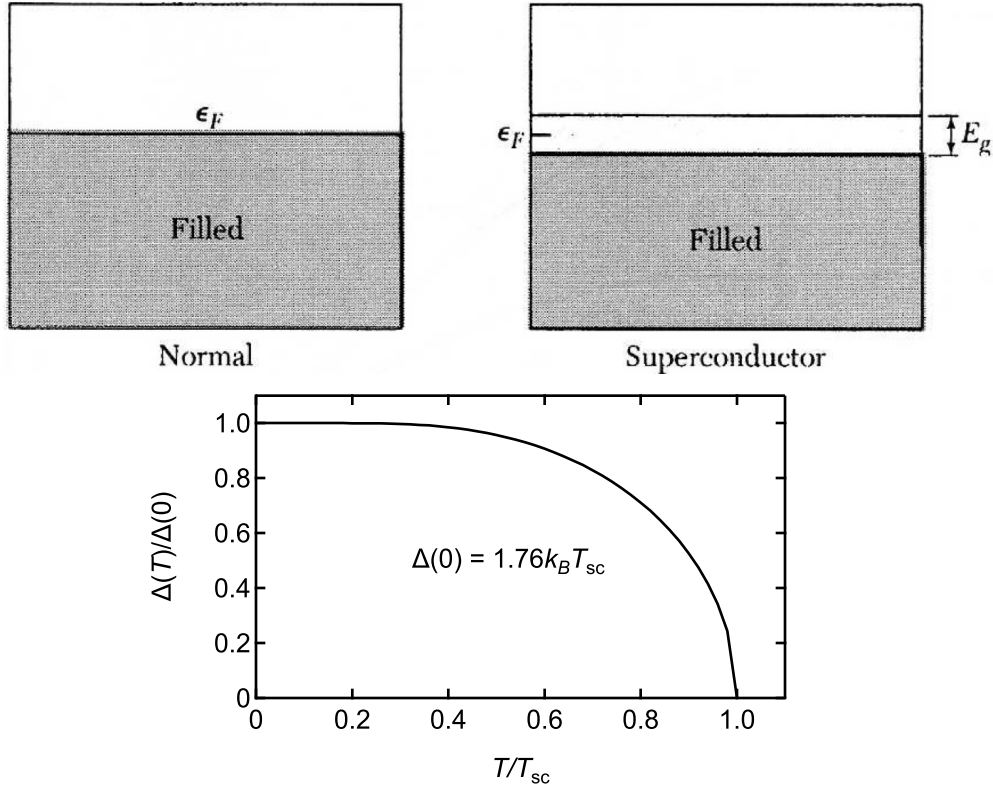
Figure 2.2: Top: Schematic of energy band fillings at absolute zero for the normal and the superconducting states. The conduction band in the normal state is completely full and no energy state above the Fermi level is occupied. In the superconducting state the energy gap, E_g, opens up at the Fermi level. Image was originally published in [6]. Bottom: Universal temperature dependence curve of the energy gap, $\Delta(T)$, for a conventional BCS superconductor. At absolute zero, all conventional superconductors will have a gap value of $\Delta(0) = 1.76 k_B T_{sc}$. Plot recreated with tabulated data from [9].

superconducting state and the resulting energy gap lower the system's thermodynamic free energy (F) an extension of BCS theory was that $F(T)$ should also develop the same for each superconductor. Importantly it also showed that the free energy difference from the energy gap at T_{sc}, $\Delta F = F_n - F_s$, should also be consistent and that the same goes for the heat capacity:

$$\Delta C = C_s - C_n = 1.76 * \gamma_n T_{sc} \tag{2.1}$$

7
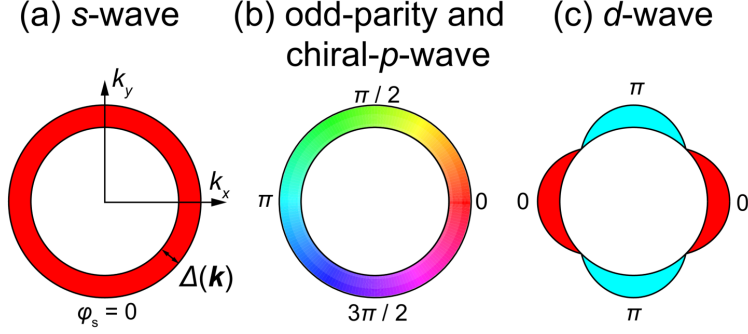
Figure 2.3: Basic schematics for (a) s-wave, (b) chiral p-wav, and (c) $d-$wave superconducting $\Delta(k)$ functions for a tetragonal lattice. Image was originally published in [10].

with γ_n as the Sommerfeld coefficient from normal state low-temperature heat capacity data. In the end measuring ΔC at T_{sc} and the shape $C(T)$ provides experimentalists a quick and easy way to determine whether a superconductor abides by conventional BCS theory.

Now we can start examining unconventional superconductivity. The easiest way to understand unconventional superconductivity is that it does not follow conventional BCS theory. As simple as that sounds, this can occur for many different reasons, such as the symmetry of Cooper pairing, the existence of nodes in the superconducting gap, and/or multiple energy gaps. See Fig. 2.3 for basic schematics of a few $\Delta(k)$ functions. Note the difference between the isotropic s-wave $\Delta(k)$ and the slightly more complicated $\Delta(k)$ functions of the unconventional chiral p-wave and d-wave. Regardless of how a material breaks BCS convention, what is common across these condensates is that they contain a superconducting state with less symmetry than the s-wave pairing. It is paramount to research unconventional superconductors because there is not yet a cohesive microscopic theory that connects all of the unique phenomena of unconventional superconductors, including predicting which symmetries are broken or preserved. Exhaustively examining the physical properties of unique unconventional superconductors combined with novel comprehensive models will continue to challenge our understanding of condensed matter systems.

8

There are several experimental probes (e.g. penetration depth, NMR, NQR, μSR) to determine whether and how a superconductor is unconventional. However, often this conclusion is most easily accomplished by examining the aforementioned heat capacity gap ΔC and the shape of the low-temperature heat capacity curve, $C(T)$, in the superconducting state. If a superconductor does not have the appropriate gap value $\Delta C/\gamma_n T_{\rm sc} = 1.76$ and/or does not follow the expected heat capacity curve, the material is clearly unconventional. From the low-temperature heat capacity data, it is possible to elucidate the existence of any nodal behavior in the superconducting gap $\Delta(k)$ [11] and/or multiple superconducting gaps [12, 13]. For example, the superconducting electronic heat capacity data for LaNiGa$_2$ is shown in Fig. 2.4 and Fig. 4.10(b). Fig. 2.4 shows the fittings for three possible single-gap nodal behavior: $C_e \propto T$ for a nodeless gap, $C_e \propto T^2$ for point nodes, and $C_e \propto T^3$ for line nodes [11]. Each of these fittings was modeled over the low-temperature ($T << T_{\rm sc}$) region and the experimental data quickly deviates from each fitting at the higher temperatures. Instead, in conjunction with London penetration depth and upper critical field fittings [14], Fig. 4.10(b) shows that a two-gap model more accurately matches the superconducting electronic heat capacity data.

Although examining heat capacity data is helpful to easily identify unconventional superconductors, it only provides a sliver of information about the full nature of the unconventional superconductivity. Therefore by performing an array of experimental techniques on a particular unconventional superconductor, we can begin to understand the full characteristics (e.g. Cooper pairing, shape of energy gap) of the superconducting state. By having a comprehensive picture of the unconventional superconductivity we can eventually begin to make the connections about what symmetries are preserved or broken to advance the microscopic models of unconventional superconductivity.
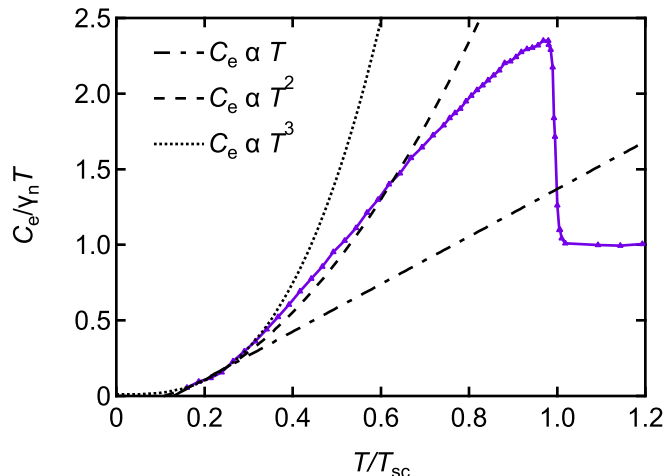
Figure 2.4: Superconducting electronic heat capacity data for LaNiGa$_2$. Overlaid are three possible fittings which show evidence for nodal features: $C_e \propto T$ for a nodeless gap, $C_e \propto T^2$ for point nodes, and $C_e \propto T^3$ for line nodes. Each fitting quickly deviates from the experimental data.

2.1.2 Symmetry and Unconventional Superconductivity

When researchers first used symmetry analysis to understand the properties of the ^{3}He superfluid state [15], theoreticians started exploring the role that symmetry plays on Cooper pairing and the energy gap in unconventional superconductors [11, 16–18]. More specifically, these researchers started applying Group Theory principles. Eventually, it was understood that a material's real-space crystal symmetry was a good predictor of possible Cooper pair order parameters in single-gap superconductors. Wherein a crystal's point group and the respective character table could be employed to decode all possible symmetries that are persevered or broken with each Cooper pairing iteration and the presence/type of nodal features within the superconducting gap.

As an example, Tables 2.1-2.4 show the character table, possible singlet superconducting states, possible triplet Cooper pairs with weak spin-orbit coupling (SOC), and possible triplet Cooper pairs with strong SOC for the D$_{2h}$ point group [18]. When zero-field muon spin

10

D_{2h} basis	Representation	E	C_2^z	C_2^y	C_2^x	i	iC_2^z	iC_2^y	iC_2^x
1	A_{1g}	1	1	1	1	1	1	1	1
XY	B_{1g}	1	1	-1	-1	1	1	-1	-1
ZX	B_{2g}	1	-1	1	-1	1	-1	1	-1
YZ	B_{3g}	1	-1	-1	1	1	-1	-1	1
XYZ	A_{1u}	1	1	1	1	-1	-1	-1	-1
Z	B_{1u}	1	1	-1	-1	-1	-1	1	1
Y	B_{2u}	1	-1	1	-1	-1	1	-1	1
Z	B_{3u}	1	-1	-1	1	-1	1	1	-1

Table 2.1: Group character table for the D_{2h} point group. Table recreated from [18]

resonance (ZF-μSR) revealed that LaNiGa$_2$ (original $Cmmm$ space group and D_{2h} point group) breaks time-reversal symmetry with a single energy gap, these tables were employed to deduce the possible Cooper pair order-parameters that would result in broken time-reversal symmetry [19]. Since LaNiGa$_2$ exhibited weak SOC behavior, these tables showed that the only possible Cooper pair order parameters that could break time-reversal symmetry were the nonunitary triplet states ($\uparrow\uparrow$) with weak SOC: $^3A_{1u}(b)$, $^3B_{1u}(b)$, $^3B_{2u}(b)$, or $^3B_{3u}(b)$. Consequently, this symmetry analysis also showed that each of these order parameters would contain superconducting gap nodes in the energy gap if the Fermi surface (FS) crossed the node location. Since LaNiGa$_2$ contains a total of 5 FSs and they collectively cross all three k-space axes (k_x, k_y, and k_z), it then follows that each of these order parameters would expect to exhibit nodal features for LaNiGa$_2$.

When experiments revealed that the low-temperature heat capacity and penetration depth measurements showed no evidence for superconducting gap nodes, it became clear that this point-group symmetry analysis was insufficient to completely predict the unconventional superconductivity in LaNiGa$_2$ [14]. This discrepancy is further enhanced when the heat capacity, penetration depth, and upper critical field data revealed multiband behavior. Therefore, despite the strength of the point group method, it is clear that LaNiGa$_2$ has a

State	g.s. order parameter	Residual group	Gap function $\Delta(k)$	Nodes: sphere	Nodes: cylinder	Name
A_{1g}	1	SO(3)$\times$D$_{2h}\times$T	1	—	—	s-wave
B_{1g}	1	SO(3)$\times$D$_2$(C$_2^z$)$\times$i$\times$T	XY	line	line	
B_{2g}	1	SO(3)$\times$D$_2$(C$_2^y$)$\times$i$\times$T	XZ	line	line	
B_{3g}	1	SO(3)$\times$D$_2$(C$_2^x$)$\times$i$\times$T	YZ	line	line	

Table 2.2: Singlet superconducting states for the D$_{2h}$ point group. The columns indicate the nomenclatures, the ground state (g.s.) order parameter, the residual symmetry group, an example gap function, the gap nodes occurring on a spherical or cylindrical FS, and the usual name. Table recreated from [18]

State	g.s. order parameter	Residual group	Gap function $\mathbf{d}(k)$	Nodes: sphere	Nodes: cylinder	Name
$^3A_{1u}(a)$	$(0,0,1)$	D$_\infty$(C$_\infty$)$\times$D$_2\times$i(E)$\times$T	$(0,0,1)XYZ$	line	line	
$^3A_{1u}(b)$	$(1,i,0)$	D$_\infty$(C$_\infty$)$\times$D$_2\times$i(E)	$(1,i,0)XYZ$	surface	surface	
$^3B_{1u}(a)$	$(0,0,1)$	D$_\infty$(C$_\infty$)$\times$D$_2$(C$_2^z$)$\times$i(E)$\times$T	$(0,0,1)Z$	line	line	
$^3B_{1u}(b)$	$(1,i,0)$	D$_\infty$(C$_\infty$)$\times$D$_2$(C$_2^z$)$\times$i(E)	$(1,i,0)Z$	surface	surface	
$^3B_{2u}(a)$	$(0,0,1)$	D$_\infty$(C$_\infty$)$\times$D$_2$(C$_2^y$)$\times$i(E)$\times$T	$(0,0,1)Y$	line	line	
$^3B_{2u}(b)$	$(1,i,0)$	D$_\infty$(C$_\infty$)$\times$D$_2$(C$_2^y$)$\times$i(E)	$(1,i,0)Y$	surface	surface	
$^3B_{3u}(a)$	$(0,0,1)$	D$_\infty$(C$_\infty$)$\times$D$_2$(C$_2^x$)$\times$i(E)$\times$T	$(0,0,1)X$	line	line	
$^3B_{3u}(b)$	$(1,i,0)$	D$_\infty$(C$_\infty$)$\times$D$_2$(C$_2^x$)$\times$i(E)	$(1,i,0)X$	surface	surface	

Table 2.3: Triplet superconducting states for the D$_{2h}$ point group, assuming weak SOC. Same notation as table 2.2. Table recreated from [18]

more complicated unconventional superconducting state than initially thought.

Before moving on, it is worth highlighting that this type of point group analysis only applies to symmorphic space groups. Space groups are direct products of the point group operations and the translation symmetries [20]. Symmorphic space groups only contain trivial Bravais lattice translations (no screw rotations or glide planes) and therefore these space groups have identical symmetry operations to their respective point group. This then makes the point-group analysis a good predictive model for single-gap symmorphic superconductors. Nonsymmorphic space groups, on the other hand, contain at least one screw axis or glide plane. These symmetry operations contain translation symmetries and make

State	Order parameter	Residual group	Gap function $\mathbf{d}(k)$	Nodes: sphere	Nodes: cylinder	Name
A_{1u}	1	$D_2 \times i(E) \times T$	(AX, BY, CZ)	—	—	BW
B_{1u}	1	$D_2(C_2^z) \times i(E) \times T$	$(AY, BX, CXYZ)$	point	—	
B_{2u}	1	$D_2(C_2^y) \times i(E) \times T$	$(AZ, BXYZ, CX)$	point	point	
B_{3u}	1	$D_2(C_2^x) \times i(E) \times T$	$(AXYZ, BZ, CY)$	point	point	

Table 2.4: Triplet superconducting states for the D_{2h} point group, assuming strong SOC. Same notation as table 2.2. Table recreated from [18]

the space group symmetry different from the point group symmetry. Consequently, the complete space group symmetries need to be used to predict all possible superconducting order parameters for nonsymmorphic superconductors. Theoreticians have recently started exploring how these nonsymmorphic symmetries operations impact the resulting unconventional superconducting gap structures at various parts within the Brillouin Zone (BZ) [21–33].

This work, both with point and space groups, shows the vital connection underlying unit cell symmetries and the superconducting state. With continued work on nonsymmorphic space groups, we can get to a point where it is possible to use a material's unit cell as a predictive model for individual superconducting states.

2.1.3 Topological Superconductivity

Initially a niche branch of mathematics to classify shapes, topology has become a pivotal concept within condensed matter systems. At first, theoreticians applied topology to predict a new state of quantum matter: two-dimensional topological insulators [34]. Experimental realizations of this state displayed the quantum spin Hall effect [35], wherein the bulk material exhibits an insulating gap but the surface states contain gapless Dirac band crossings [36–38]. Shortly thereafter, topological classifications were applied towards other quantum states with energy band gaps like superconductors [39, 40]. It is now understood that experimen-

tal realizations of topological superconductivity could provide a promising pathway towards discovering Majorana fermions (quasiparticles that are their own antiparticles) [41–43]. Discovering and harnessing these quasiparticles could profoundly impact engineering reliable fault-tolerant quantum computing devices [44, 45]. There are several articles on the theoretical aspects of topological superconductivity [46, 47]. Here I will briefly discuss the materials that exhibit topological superconductivity and the experimental signatures of this state.

Thus far, there are several routes towards topological superconductivity such as artificial heterostructures [41, 42, 47–49], unconventional superconductivity overlapping or in the proximity of a magnetic ordering [50–55], inducing superconductivity within Dirac materials [46, 56–65], and discovering topological features amongst unconventional superconductors [66–73]. One of the most promising methods is through single-material unconventional superconductors (topological crystalline superconductors) because these materials do not require special heterostructure engineering, the lack of magnetism makes studying the electronic behavior more accessible, and inducing superconductivity in known Dirac materials is difficult to predict. The promise of single-material topological superconductors (TSCs) is especially true when put in the context that many theoreticians are starting to explore the symmetry connections between a material's space group and the resulting topological features (Dirac crossings) [32, 33, 52, 74–80]. This association could then provide an easy avenue to predict topological behavior just from a unit cell and the resulting electronic structure [81–83].

Several key identifying features develop from topological superconductivity. Possibly the simplest way to identify a single material TSC is that the material contains Dirac band crossings (in bulk or surface states) while also exhibiting unconventional superconductivity. These Dirac crossings can take on various forms (nodal points/lines, surfaces), occur across

14

a range of energy levels, be entirely accidental or symmetry-protected, and exist anywhere throughout the BZ. Therefore, locating and verifying these features through DFT band calculations and scanning tunneling microscopy or angle-resolved photoemission spectroscopy (ARPES) measurements is critical to understanding the topological nature of unconventional superconductors.

One possible consequence of topological superconductivity is that the superconducting order parameter could induce Cooper pairs that break time-reversal symmetry [4, 47]. Materials with this exceedingly rare superconducting property (~ 25 known systems) provide a space for theoreticians and experimentalists to better understand the interplay between topology, unconventional superconductivity, and crystal structure. In that context, our work on $LaNiGa_2$ provides a clear example of how a crystal structure can connect the underlying topological features and the resulting time-reversal symmetry breaking superconductivity.

2.2 Concepts related to $CeIn_3$

2.2.1 Magnetic Ordering

Since magnetism is so relevant to modern-day technology, much condensed matter research has focused on the underlying physics behind magnetism over the past century. Why magnetism exists within certain compounds? What is the structure of a magnetic ordering within a material? What happens when magnetism is suppressed to lower temperatures? Answering these fundamental questions and constructing models to accurately predict these interactions can ultimately help us better understand the world around us and construct better technology for the future. Since magnetism is such a significant topic with hundreds of books focused on this topic, I will have a brief overview of the types of magnetic orderings

and then talk about the Ruderman-Kittel-Kasuya-Yoshida (RKKY) interaction which can influence the magnetic ordering of $4f$ ions. Since my magnetism work almost exclusively focused on antiferromagnetic (AFM) systems, I will focus on these concepts. In section 3.3.2 I will discuss and show experimental signatures of paramagnetism and antiferromagnetism. This overview will provide a bases for the physics relevant to CeIn$_3$ and what happens as magnetic orderings are suppressed. More details about magnetism and the microscopic origins can be read up in several sources [6, 84].

Types of Magnetic Orderings

There are several types of magnetic orderings (e.g. ferrimagnetism and helical ordering); however, I will first focus on the two most common types of magnetic ordering: ferromagnetic (FM) and AFM. In the simplest case, FM materials have a spontaneous magnetization with all magnetic moments aligned along a single direction. Whereas an AFM system has its localized magnetic moments orientate so that they are antiparallel to their neighbors. First, we will examine what happens to the magnetic material before entering the ordered state.

Above the transitions temperatures for the two magnetic orderings, T_C for FM and T_N for AFM, typically a magnetic system is in a magnetically disordered state called paramagnetism. There are several models of paramagnetism, but the most typical model for $4f$ systems is the Cure-Weiss behavior. The localized magnetic moments are randomly orientated throughout the material but can interact with an external magnetic field and internally amongst other moments. The internal magnetic moments will begin to align when exposed to increasing external magnetic fields. Nevertheless, the state remains disordered because of thermal fluctuations. Then as the system cools down and the thermal vibrations of the moments reduce, the moments increasingly align with the external magnetic field. Thus

increasing the magnetic response. This paramagnetic behavior is well described by the following Curie-Weiss law:

$$\chi(T) = \frac{C}{T - \Theta_{CW}} \qquad (2.2)$$

where χ is the magnetic susceptibility (M/H), C is the Curie constant, and Θ_{CW} is the Curie temperature in Kelvin [6, 84]. With decreasing temperature, the disordered magnetic moments will align more and the susceptibility will rise. Paramagnetic systems will follow the Curie-Weiss law until a magnetic ordering occurs. In section 3.3.2 I will discuss experimental signatures of Curie-Weiss paramagnetic behavior and what information can be extracted from this state.

Simply put, in FM systems the magnetic moments all align in a particular direction. The magnitude and specific direction of the ordering varies between materials and depends on the unit cell and the magnetic atom(s). When a paramagnetic system becomes FM, the susceptibility response should sharply increase because all the moments align along the same direction.

AFM materials are a bit more complicated than FM ones. The basic description for an AFM structure is that the magnetic moments within a system are aligned antiparallel to its nearest neighbor. Since magnetic moments occur within 3D space, several different possible AFM configurations could satisfy that basic definition (Fig. 2.5). To make matters more complicated, within the more simplistic AFM orderings in Fig. 2.5 it is possible that moments can align in any particular direction. Just so long as a neighboring moment aligns antiparallel. Therefore studying AFM materials and understanding the magnetic structure of these materials is considerably more complicated and than their FM counterparts.

In section 3.3.2 I will go over the experimental signatures of AFM materials in magnetic susceptibility, but for now let us discuss how AFM structures can be determined. Deter-

17
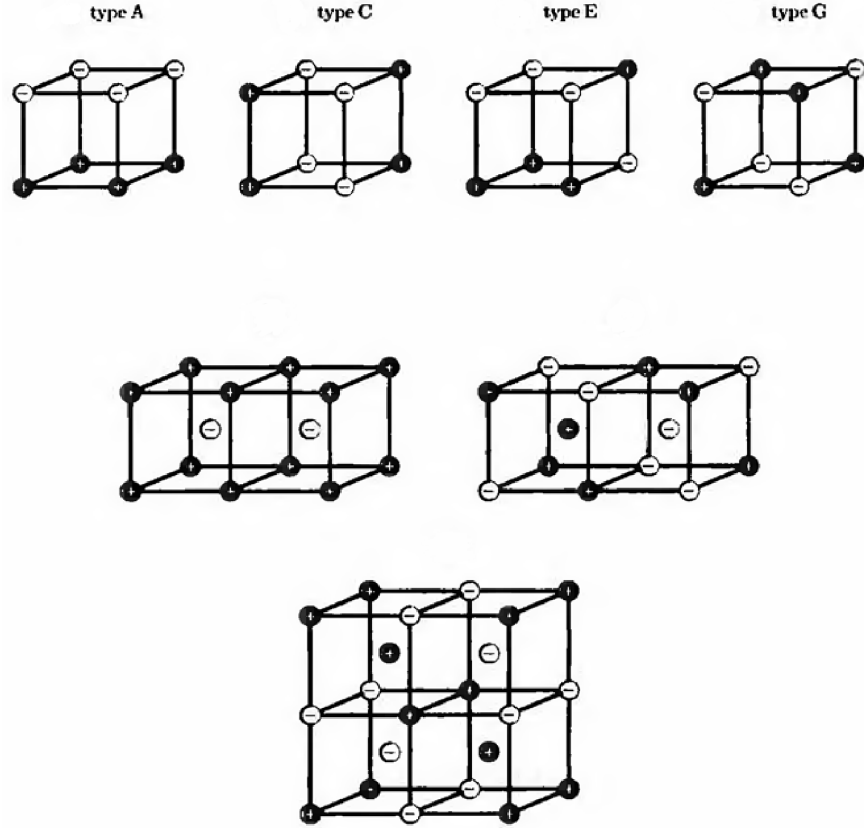
Figure 2.5: Possible AFM structures that can exist within a simple cubic (top four) and a body-centered cubic (bottom three) lattice. The possible spin states are marked as + or −. Image was originally published in [84]

mining an AFM ordering is more akin to solving a crystal structure. Therefore, just like one would use diffraction to determine the unit cell, diffraction can be employed to elucidate the AFM order. In unit cell determination, the most common diffraction source are X-rays because they interact directly with the electron cloud of an atom and are readily available. Despite an atom's magnetic moment originating from the valence electrons, photons contain no magnetic moment and therefore will not interact with the magnetic moment. So to 'observe' the magnetic spins, the diffraction source needs a net magnetic moment, such as neutrons. Hence neutron diffraction is the most common and powerful technique to elucidate

18
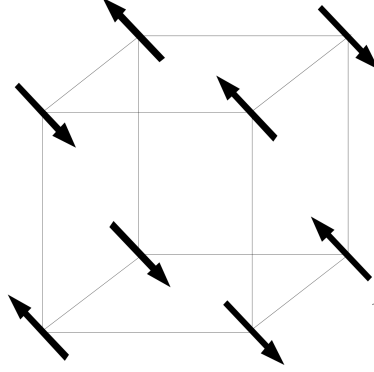
Figure 2.6: The AFM ordering of CeIn$_3$ determined to have a **Q**= $(1/2, 1/2, 1/2)$ from neutron diffraction experiments [86, 88]. Image was originally published in [89]

AFM magnetic structures [6, 85].

Generally, AFM structures can be placed into one of two categories: commensurate or incommensurate modulation. AFM structures as a whole have a repeating 'wave' of magnetic oscillations throughout the crystal [85]. As a result, the periodic function of the AFM ordering can be defined by a propagation vector called the **Q**-vector. Where the wavelength of the periodic modulation is equal to $2\pi/\mathbf{Q}$. If the **Q**-vector contains rational numbers then the AFM structure is defined as commensurate. In the case of CeIn$_3$, through neutron diffraction experiments, it was discovered that the AFM ordering has a propagation vector $\mathbf{Q} = (1/2, 1/2, 1/2)$ and can be visualized in the cubic unit cell in Fig. 2.6 [86, 87]. Most often, like CeIn$_3$, the AFM ordering and the associated propagation vector extends beyond a single crystal unit cell to produce a supercell.

In short, commensurate AFM structures have rational numbers within the **Q**-vector, while incommensurate have irrational numbers. Therefore a single periodic function can not relay the necessary information about the magnetic moments. Instead incommensurate AFM orderings need to have multiple or more complex functions to convey the periodicity [85]. Such an AFM ordering was discovered within the complicated magnetic phase diagram for

19

NdIn$_3$. In this material the first AFM transition coincides with the onset of an incommensurate ordering. As the system cools, two additional AFM structures are observed [90]. In the end, a commensurate AFM ordering with a $\mathbf{Q} = (1/2, 1/2, 0)$ in NdIn$_3$ stabilizes below 4.83 K.

RKKY Interaction

As discussed above, magnetic ordering results from magnetic moments interacting with other nearby moments. In highly localized $4f$ systems, this exchange interaction typically occurs through indirect means, where the $4f$ moment couples with the conduction electron. Subsequently, the conduction electron then interacts with a neighboring $4f$ moment [6, 84, 91–93]. This interaction produces a spatial 'ringing' effect in the magnetization with the following function:

$$F(x) = \frac{-x\cos x + \sin x}{x^4} \tag{2.3}$$

where x is proportional to the real space distance between magnetic moments. As a result, the RKKY interaction produces a distance-based oscillatory coupling between the $4f$ magnetic moments. Which in turn can dictate whether the resulting magnetic ordering of the entire system is FM or AFM. Overall, this interaction shows that the distance between $4f$ ions can have a huge impact on the type of magnetic ordering.

2.2.2 Kondo Physics

Here I will briefly discuss an overview of Kondo effects through the example of tetragonal CeMIn$_5$ (M = Co, Rh). This overview will help us better understand the underlying physics in cubic CeIn$_3$. There are two main types of Kondo effects: Kondo impurities and Kondo coherent lattices. Oftentimes, these effects are mistakenly and confusingly mixed up for one

another. To make matters worse, the same terminology is often erroneously used for both types of effects.

Kondo Impurity

Historically, the Kondo effect was first described as a way to rationalize a strange resistivity uptick observed within metallic systems at low temperatures [94]. This phenomenon would only occur in nonmagnetic metals alloyed with a very dilute concentration of magnetic ions. In these materials is was discovered that the magnetic moments from the impurity atoms would couple with the conduction electrons to form an opposite spin-polarization cloud. Although this behavior was first discovered in metals diluted with magnetic transition metals, Kondo physics is now most associated with heavy fermion materials (Ce, Yb, U) because the $4f$ electrons and resulting magnetic moments from these elements are localized and interact with conduction electrons.

As a result, this coupling has two main consequences. First, the overall magnetization decreases below the expected value from Curie's law. Second, the electron scattering and thus the resistivity $(\rho(T))$ increases proportional to $J_k ln(T)$ [84]. Where J_k is the exchange coupling (Kondo coupling constant) between the local moment and the conduction electrons and commonly $J_k < 0$. This $\rho(T)$ upturn is only observed when a material is cooled to a low enough temperature such that the phonon scattering behavior is no longer dominant.

From this model, the Kondo temperature, T_K, is defined as a theoretical temperature where $\rho(T)$ deviates from the $-ln(T)$ behavior [94]. At first, this temperature was thought to be too low to observe experimentally; however, $\rho(T)$ was eventually shown to deviate from the logarithmic behavior at very low temperatures (see Fig. 2.7). Furthermore, $\rho(T)$ was also shown to flatten completely at temperatures much lower then T_K. Initially, this

21
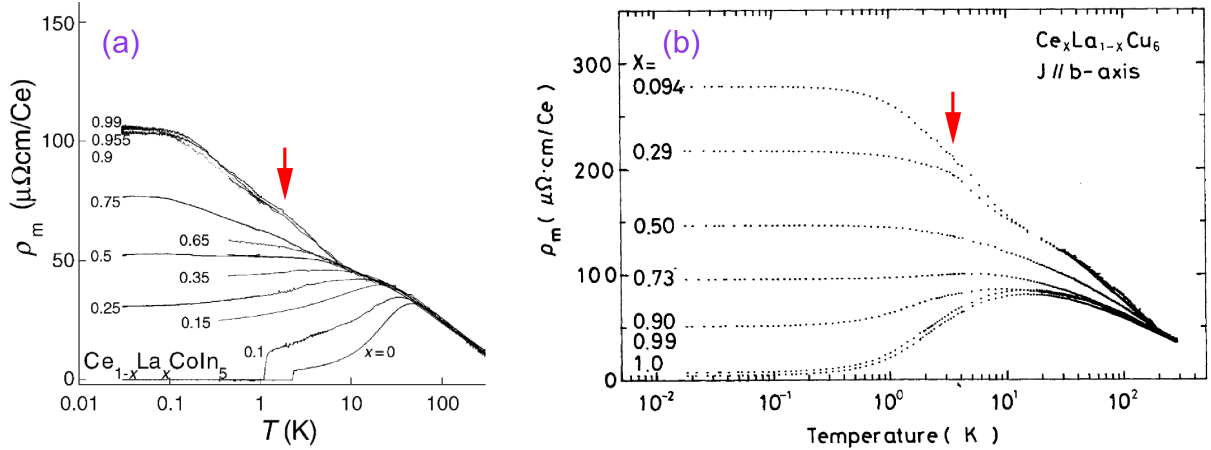
Figure 2.7: (a) In-plane ρ_{mag} per molar Ce for various x in $Ce_{1-x}La_xCoIn_5$. The red arrow is roughly where $T_K \approx 1.5\,K$ is located and where the $-ln(T)$ relationship slightly diverges for the Kondo dilute systems $x = 0.9, 0.944$, and 0.99. Plot was originally published in [95]. (b) Temperature dependence of ρ_{mag} per molar Ce in $Ce_xLa_{1-x}Cu_6$. The red arrow is roughly where $T_K \approx 3.5\,K$ [96] is located and where the $-ln(T)$ relationship slightly diverges for the Kondo dilute systems $x = 0.094$ and 0.29. ©(1986) The Physical Society of Japan. Plot was originally published in [97]. In both plots ρ_{mag} is labeled as ρ_m.

flattening was an issue with the original model but was then rationalized by the onset of a Kondo singlet ground state between the local $4f$ magnetic moments and the conduction electrons [98, 99]. From theoretical calculations, T_K occurs before $\rho(T)$ flattens and is shown to be proportional to:

$$T_K \propto De^{\frac{-1}{J_k n(E_F)}} \tag{2.4}$$

where D is the band-width of the conduction band and $n(E_F)$ is the density of states at the Fermi level [100, 101]. From a theoretical perspective, T_K also coincides with the crossover from perturbative to non-perturbative Kondo coupling [101]. Experimentally, T_K can be observed in Kondo impurity systems where magnetic resistivity $(\rho_{mag}(T))$ deviates from $\rho_{mag}(T) \propto -ln(T)$. Examples of this behavior can be observed in Fig. 2.7 where La-substituted $CeCoIn_5$ [95] and $CeCu_6$ [97] both show slight divergences from low-temperature

22

$-ln(T)$ behavior near their respective T_K values.

The defined T_K and the ground singlet behavior can be seen in the Fig. 2.8(a,c). Using the labels from [101], the notation in Fig. 2.8 is defined as:

T_K^{onset} = onset of incoherent spin-flip scattering $- ln(T)$ resistivity

T_K' = resistivity minimum crossover from phonon-scattering to $- ln(T)$ resistivity

T_K^h = effective Kondo temperature including the full sixfold degeneracy of the

$J = 5/2$ f-states

T_K = Kondo temperature for groundstate f-level

theory crossover

T_K^{gs} = onset of fully-screened Kondo singlet ground state

In the high-temperature region of the dilute system $(T > 30\,K)$ there is another region for heavy fermion materials that follows the $-ln(T)$ behavior. In this regime the higher-energy crystal electric field (CEF) levels are populated and incoherent Kondo scattering occurs because the higher degeneracy (N=6) increases T_K. This feature is well described by Cornut and Coqblin [102] and more will be discussed about these features separately in section 2.2.3. Nonetheless, it is important to highlight that even in diluted Ce systems this $-ln(T)$ behavior is observed at much higher temperatures than the traditional Kondo impurity temperature regime [95].

Kondo Coherent Lattices

Aside from the low-temperature dilute phenomena, Kondo interactions can also be observed in high-temperature regions of heavy fermion materials. In these systems the defining char-
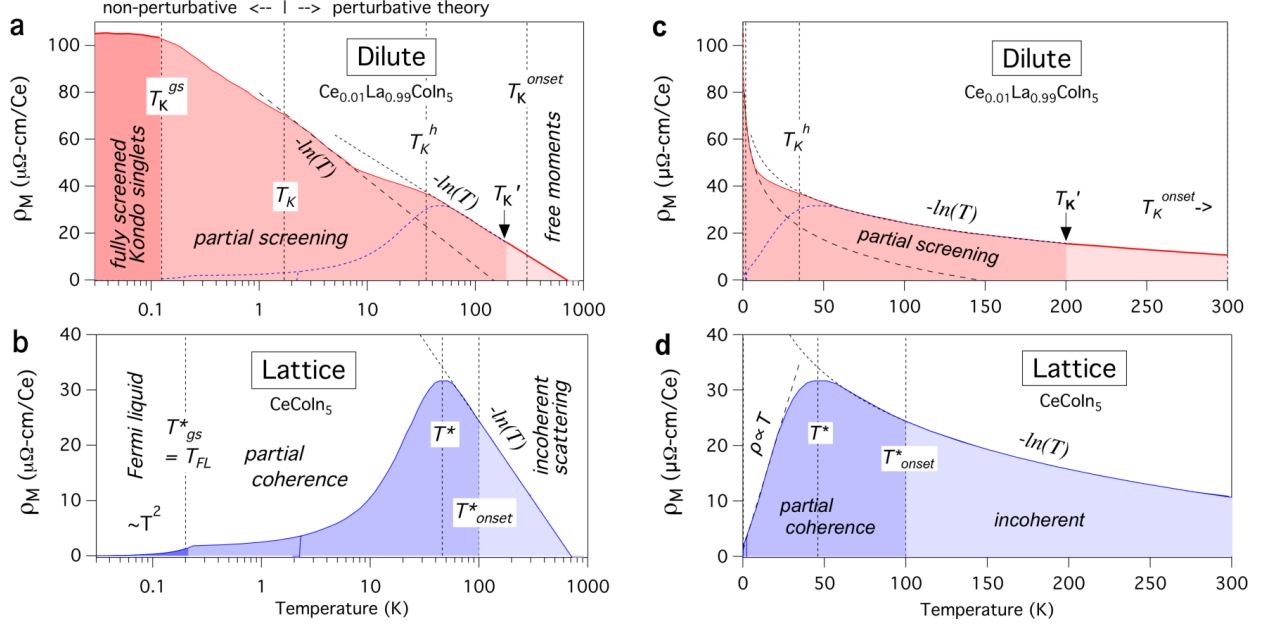
Figure 2.8: (a,b) Schematic magnetic resistivity profiles for (a) a dilute impurity and (b) a Kondo lattice system. (c,d) Linear temperature scales of plots (a) and (b), respectively. All of the T values are defined in the main text. Figure was originally published in [101].

acteristic is a broad maximum (denoted by T^*) in $\rho_{mag}(T)$ (See Fig. 2.8(b,d)). As the temperature lowers from room temperature, there is an initial scattering increase because of the Kondo coupling between the f-bands and the conduction electrons. This increase in $\rho_{mag}(T)$ also follows the $-ln(T)$ relationship until the broad crossover into a 'coherent' system. At which point the resistivity begins to drop because the heavy fermion f bands hybridize with the conduction bands. Hence the 'Kondo coherence' label for the resistivity maximum at T^*. Again using the notation from [101], the notation used in Fig. 2.8 is defined as:

$$T^*_{onset} = \text{onset of lattice coherence}$$

$$T^* = \text{magnetic resistivity maximum, onset of the resistivity downturn}$$

$$T^*_{gs} = T_{FL} = \text{onset of ground state Fermi liquid } T^2 \text{ resistivity behavior}$$

It should be noted that this feature does not have a microscopically defined origin but instead is strictly determined by the observed features in resistivity, magnetic susceptibility, and heat capacity data. Another essential piece of information to highlight is that this only occurs in a lattice with a dense periodic array of magnetic elements (Ce, Yb, or U). That is because in materials with these elements, the f-level bands from these atoms are energetically close to the Fermi level and can interact with the conduction electrons.

The proximity of these $4f$ bands to the Fermi level can also cause CEF interactions [102]. Therefore to comprehensively understand the consequences of each interaction it is essential to first isolate the Kondo lattice coherence from the CEF phenomena. This can be achieved by driving the energy scale of the Kondo lattice coherence lower with chemical substitution [95, 103–105]. However, sometimes it can be difficult to make broad conclusions because chemical substitution can also change the CEF parameters and/or Kondo coupling [106–108]. Alternatively, the system could not contain a Kondo coherent lattice at all [109]. In the end, this difficulty can often lead to the wrong conclusions about the underlying physics of a material.

2.2.3 Crystal Electric Field

The CEF interactions impacts on a condensed matter system are best understood at the molecular level with a general chemistry principle — Crystal Field Theory (CFT). This model helps explain the orbital splitting observed from local symmetry and the resulting physical characteristics observed for a single molecule. Here it is assumed that there are no intermolecular interactions and, therefore, no periodic lattice effects.

CFT is best understood from a simple molecule with an octahedral geometry and a $3d$ metal center (Fig. 2.9). Before the formation of the molecule, all five $3d$ orbitals are energetically degenerate. If one were to assume that the ligands form a uniform negative electrical charge around the metal center, the energy level of all $3d$ orbitals would collectively rise. The orbital degeneracy is only ruined when the ligand negative charges coalesce into point charges to form an octahedron. Once in this geometry, the $3d$ orbitals with the most direct interactions with the ligand point charges, $d_{x^2-y^2}$ and d_{z^2}, will increase. Whereas the $3d$ orbitals with lobes off-axis from the ligands; d_{xy}, d_{xz}, and d_{yz}; will slightly lower their energy. The molecule's resulting physical properties (e.g. magnetism and optical) will then be determined by how the valence electrons from the metal center fill these orbital energy levels. Overall this is a simple and straightforward example that shows that the local geometry around an atomic center can have a significant impact on the energy levels and resulting physical properties of a molecule.

When scaling the CFT interaction to a periodic crystalline solid, the picture is not quite as simple. First off, the discrete energy levels of a single molecule smear together to form bands. The energy of these bands are still associated with the discrete energy levels from the individual molecules/atoms, so they are still impacted by the central element and the local geometry. Second, for materials with heavy elements with localized f electrons, the strong
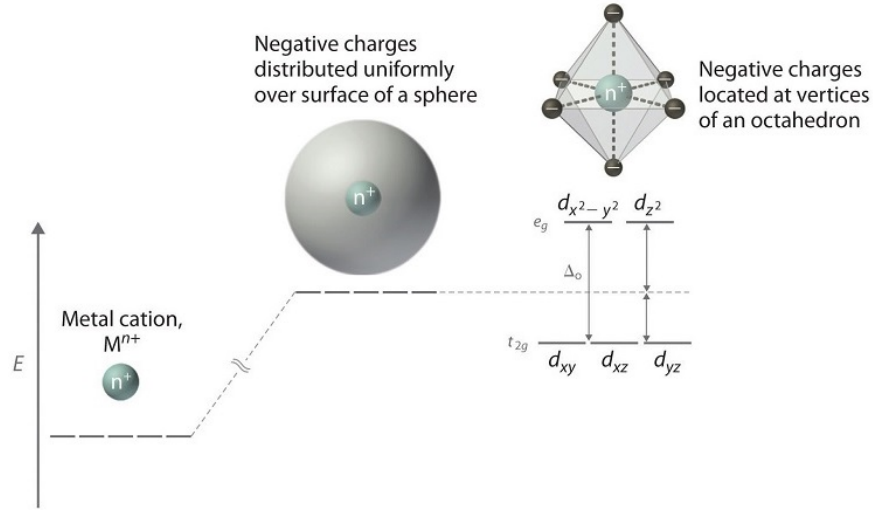
Figure 2.9: Schematic of CFT splitting as a result of an octahedral molecule. Image was originally published in [110].

SOC (coupling between electron and orbital spin) and the number of f electrons will split energy levels before accounting for environmental splitting. For these elements/materials, the total angular momentum quantum number, J, can describe the ground-state of energy levels before accounting for CEF interactions. In the case of $4f$ heavy fermion ions with one unpaired electron ($4f^1$ for Ce^{3+} and $4f^{13}$ for Yb^{3+}) we can determine the J value by following Hund's rules:

$$L = 3$$

$$S = 1/2$$

$$J = L \pm S = 7/2 \text{ and } 5/2$$

where L represents the orbital angular momentum quantum number and S is the electron spin quantum number. For systems with an f-shell that is less than half full, the primary multiplet is $J = |L - S|$. While for systems with an f-shell that is more than half-filled the

27

ground multiplet is $J = L + S$. Therefore, materials with Ce^{3+} ions have a ground state of $J = 5/2$, and Yb^{3+} has a $J = 7/2$. With the appropriate J value determined, the actual number of energy levels are determined by:

$$m_j = -J, -J+1, -J+2, ...J-1, J \tag{2.5}$$

Which gives discrete m_j values for Ce^{3+} as $\pm 5/2$, $\pm 3/2$, and $\pm 1/2$ and a sextet ground state. While for materials containing Yb^{3+} have $m_j = \pm 7/2$, $\pm 5/2$, $\pm 3/2$, and $\pm 1/2$ and an octet ground state. Meaning that despite Ce and Yb ions only having one unpaired $4f$ electron, the two elements have to be treated separately in regards to their SOC and CEF interactions.

With the appropriate ground state determined, the CEF and local geometry around the heavy fermion atom can be fully accounted. In cubic Ce systems, the $J = 5/2$ ground state is split into a doublet and a quartet [102]. The energy level schematic within a cubic system is then dependent upon the number of point charges and the geometry of these point charges immediately around the Ce atom [111]. In the case of cubic $CeIn_3$ the sextet splits into a ground state doublet (Γ_7) and a higher energy quartet (Γ_8) [112]. While cubic CeAg, CeMg, and CeZn (all CsCl structure type) each have a low lying Γ_8 and a higher energy Γ_7 [113]. For Ce systems with lower symmetry, tetragonal or hexagonal, the cubic quartet Γ_8 is split into two doublets to form three distinct doublets [84, 102, 114]. In these systems, the order of the doublets can vary between different tetragonal/hexagonal structures and can even vary between materials with the same structure [114].

To summarize the SOC and CEF energy level splitting in a tetragonal system, the schematic is shown in Fig. 2.10. As it can be seen, the $J = 7/2$ energy level exists for a Ce^{3+} system. However the energy difference between the $J = 5/2$ and $J = 7/2$ levels

28

is estimated to be $0.3\,\text{eV}$. Which roughly equates to about $3000\,\text{K}$. So this higher energy branch is effectively empty because it is never appreciably thermally excited. Whereas the CEF splitting, in this example, between the ground state doublet to the second doublet is $\sim 5\,\text{meV}$ ($\sim 50\,\text{K}$). Therefore, in this tetragonal Ce^{3+} system the thermal transitions of electrons (excitation or depopulation) can play a critical role in the observed electronic, magnetic, and thermodynamic properties. This is especially true for any heavy fermion material where the rare-earth bands are close to the Fermi level, as discussed in section 2.2.2. For other $4f$ systems without bands near the Fermi level, these energy levels/gaps will not impact the observed properties because they will either always be occupied or are so high in energy that they are practically empty across all temperatures.

2.2.4   Combined Kondo and CEF interactions

This brings us back to the Kondo effect and the impact of CEF splitting on these heavy fermion systems. In order to best understand how CEF interacts with the Kondo physics discussed above, we will examine the impacts of CEF splitting and depopulation on resistivity experiments. As first described by Cornut and Coqblin [102], the authors wanted to understand the influence of CEF splitting on the Kondo effect in alloys and compounds with Ce or Yb impurities. The calculations from this model are lengthy but well described. They have been reproduced on several systems to understand how the CEF and Kondo interactions develop with the evolution of pressure [109, 115, 116]. Although these systems ($CeAl_2$, $CeAl_3$, and $CeZn_{11}$) are not true Ce-dilute alloys, this model has successfully explained the influence of CEF on the Kondo effect in these heavy fermion materials and countless others.

To summarize the calculations, it was found that several parameters impact the CEF interactions and, ultimately, the resistivity curves. Overall this model showed that at suf-
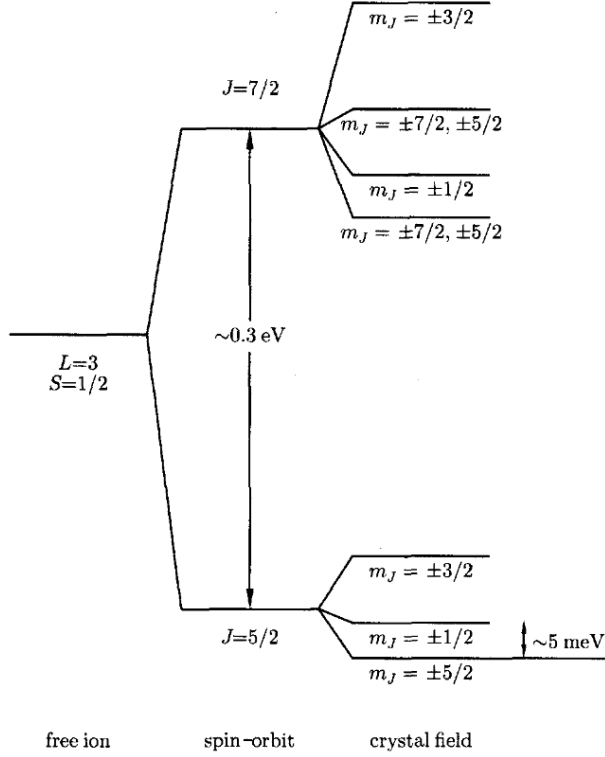
Figure 2.10: Schematic of energy level splitting for a Ce^{3+} ion in a tetragonal structure. The splittings are exaggerated to easily observe each energy level. Image was originally published in [84].

ficiently higher temperatures than the CEF splitting ($T > k_B \Delta_{\text{CEF}}$), all CEF states are thermally populated and incoherent Kondo scattering increases $\rho_{mag}(T) \propto -ln(T)$. As the temperature decreases, the excited CEF states begin to depopulate down to the lower energy excited state and/or ground state. Thereby reducing the degeneracy of the occupied energy levels. Following the depopulation of the CEF energy levels, $\rho_{mag}(T)$ is expected to drop. Thereby forming a broad maximum in $\rho_{mag}(T)$ with $T_{Max} \sim \Delta_{\text{CEF}}$ (in Fig. 2.8(b,d) this feature is labeled as T^*).

This CEF depopulation effect should occur for every well-separated Δ_{ij} within a system. So within a cubic system with one energy gap, Δ_{12}, it is expected that one region with

30
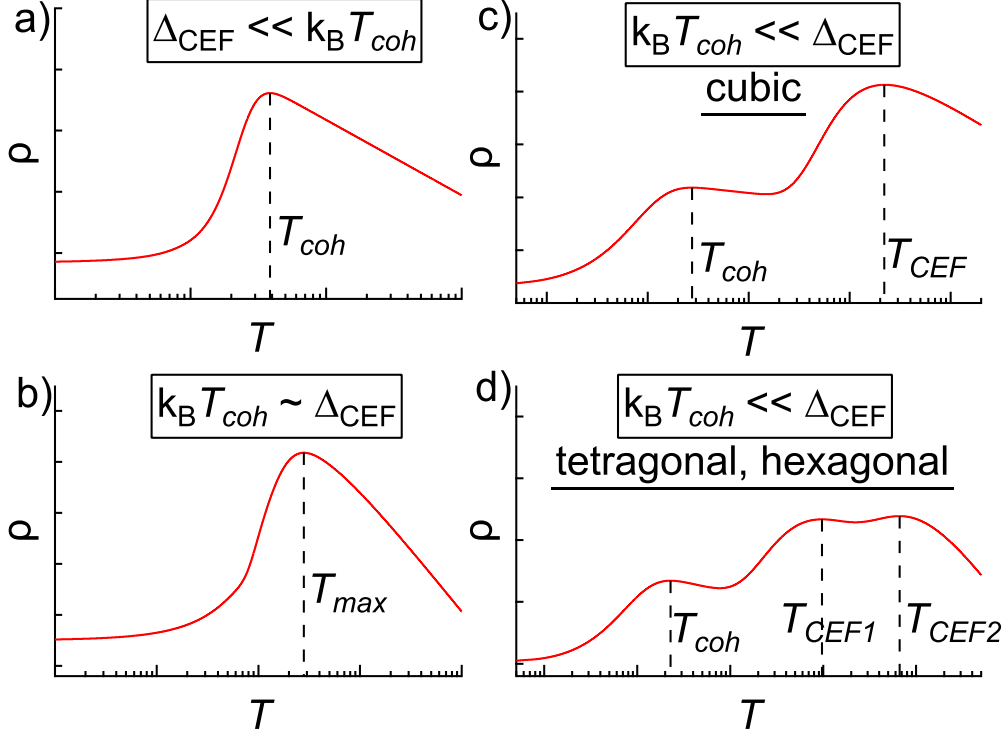
Figure 2.11: Schematics of the temperature dependence of the electrical resistivity for a Kondo lattice (ignoring phonon contributions). a) the CEF splitting energy Δ_{CEF} is smaller than the Kondo coherence energy scale T_{coh}. b) Δ_{CEF} and k_BT_{coh} are of similar magnitude. c) and d) k_BT_{coh} is smaller than Δ_{CEF}. In cubic symmetry c), there are two resistivity maxima associated with the coherence and CEF effects. In hexagonal or tetragonal symmetries d), there can be a third maxima associated with the additional CEF energy splitting.

$\rho_{mag}(T) \propto -ln(T)$ and broad maximum will occur with $T_{Max} \sim \Delta_{12}$ [102, 115]. While for tetragonal or hexagonal materials, two energy gaps, Δ_{12} and Δ_{13}, exist and therefore, two regions with $\rho_{mag}(T) \propto -ln(T)$ and broad maxima are expected [117–119].

However, in many systems the number of broad maxima in $\rho_{mag}(T)$ differs from the expected number of depopulation features. This difference can be directly attributed to the Kondo lattice coherence or because of similar energy scales between different Δ_{ij} gaps. The difference between the expected and experimental maxima depends on the Kondo lattice coherence energy scale (k_BT_{coh}) relative to Δ_{CEF}. For example, in cubic CeMg$_3$ two broad

31

maxima, each with a region $\rho_{mag}(T) \propto -ln(T)$, are observed even though there is only one CEF splitting [120]. In such a system $k_B T_{coh} << \Delta_{CEF}$ so the high-temperature maximum is associated with the CEF depopulation effect, and the low-temperature maximum is correlated with the Kondo lattice coherence (schematically shown in Fig. 2.11(c)).

Whereas the opposite, fewer maxima than expected, can also exist. Each of CeMIn$_5$ (M = Co, Rh, Ir) have two well-separated CEF splittings (Δ_{CEF}^{High} and Δ_{CEF}^{Low}) [114]. Hence one would expect two regions with $\rho_{mag}(T) \propto -ln(T)$ and maxima associated with the two CEF splittings. Plus, one more maximum from the Kondo lattice coherence if $k_B T_{coh} << \Delta_{CEF}^{Low}$ (schematically shown in Fig. 2.11(d)). However, the resistivity curve from each compound clearly shows only one maximum [121–123]. Revealing that that either $k_B T_{coh} \sim \Delta_{CEF}^{High}$ or $k_B T_{coh} >> \Delta_{CEF}^{High}$ for each of CeMIn$_5$. As shown in Fig. 2.11(a,b) both scenarios would result in a single maximum for any unit cell.

Ultimately this summary shows that it is inherently difficult to truly isolate the impacts of Kondo and CEF interactions on any particular heavy fermion system. This is especially true when $k_B T_{coh} \sim \Delta_{CEF}$. Although through the evolution of hydrostatic pressure or chemical substitution it is possible to alter $k_B T_{coh}$ to either separate or conjoin the feature with the CEF depopulation feature [95, 103, 117–119, 124–131].

2.2.5 Quantum Criticality

Over the past several decades studying quantum criticality in heavy fermion materials has been incredibly important to the progress of the condensed matter community. To begin to understand 'quantum criticality' it is best to first examine the two underlying aspects within the name. The first is 'quantum.' Although quantum is used everywhere these days, the specific usage, in this case, comes from 'quantum phase transition.' Typically a

phase transition occurs when a particular phase is destroyed or condensed by increasing or decreasing thermal fluctuations, respectively. A quantum phase transition, however, occurs when a phase transition is controlled by another nonthermal variable (such as pressure, external magnetic field, or chemical substitution/doping) such that at some critical value the phase transition is driven to occur at absolute zero [84, 132]. At a quantum phase transition the phase change is no longer driven by thermal fluctuations but instead quantum fluctuations.

The second part of this term, 'criticality,' which comes from 'critical point.' A critical point is a unique point on a phase diagram where phase transition models (e.g. mean free theory) break down. As an example, let us examine the most commonly known critical point in the $p - T$ phase diagram of water. The phase transition is well described as a first-order transition along the boiling line (A-E in Fig. 2.12). At the critical point (point E in Fig. 2.12), the liquid-gas transition shifts to a second-order phase transition and classical phase transition models break down. Above the p and T values of the critical point the liquid and gas phases cannot be distinguished. As the system approaches the critical point, the fluid's heat capacity and compressibility curves both diverge from their expected shapes in the form of a power law.

So a 'quantum critical point' is a particular point on a phase diagram where a critical point occurs at absolute zero. Systems with quantum critical points are expected to display unusual phenomenon around the quantum critical point. This region is the zone of quantum criticality, where phases are controlled by quantum fluctuations (Fig. 2.13). Even systems without a true quantum critical point often reveal novel phenomena when ordered systems are pushed towards a quantum phase transition. The research born out of the search for quantum critical points has resulted in many exotic low-temperature phases
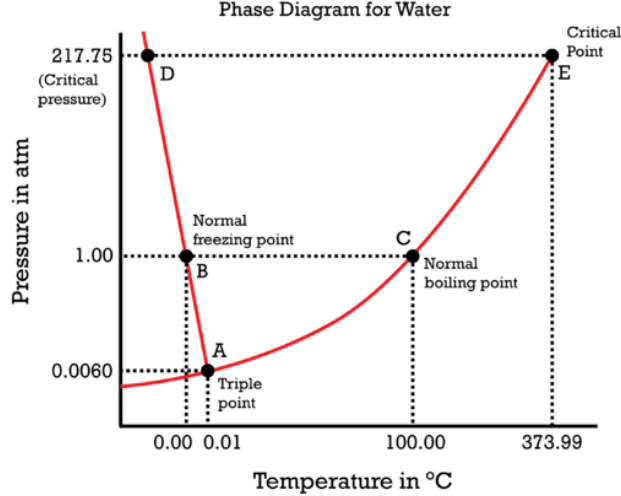
Figure 2.12: $P - T$ phase diagram of water. The critical point shows where the liquid-gas transition shifts from being first-order (along red line) to a second-order transition at the critical point. Above this pressure and temperature, both the liquid and gas phases exist simultaneously. Image was originally published in [133].

such as heavy fermion superconductivity [134–136], coexisting magnetism and superconductivity [55, 137–139], reentrant superconductivity [140–143], winged ferromagnetic phase diagrams [132, 144–148], and non-Fermi liquid behavior [149–152]. Overall, studying these low-temperature phase diagrams by tuning pressure, magnetic fields, and/or chemical substitution has revealed novel low energy states which have immensely progressed the condensed matter physics community.

Heavy fermion metals have been the focus in many studies searching for quantum critical points [154]. Specifically, Ce-based fermion systems have been extensively studied in search of quantum criticality. One such system is $CeIn_3$. Where countless studies have examined the phase diagrams of $CeIn_3$ when tuning with pressure [88, 89, 155–160], magnetic fields [161–164], and chemical substitution [104, 165–171]. Overall it appears that $CeIn_3$ does not exhibit a quantum critical point as the AFM phase is suppressed with magnetic fields, chemical substitution, or pressure (Fig. 2.14). $CeIn_3$, however, does show a small superconducting
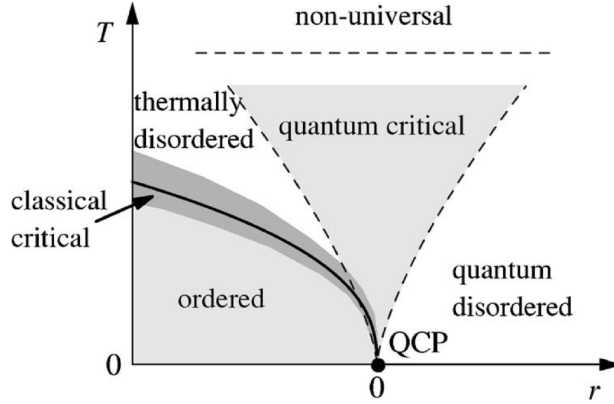
Figure 2.13: A generic phase diagram of an ordered state as the nonthermal parameter r is used to tun the system towards a quantum critical point. The solid line marks the temperature boundary between order and disordered phases. The dashed lines indicate the boundaries of the quantum critical region. Figure was originally published in [153].

dome near the quantum phase transition as the AFM ordering is tuned with pressure [89, 156–158].

2.2.6 Percolation Limit

Percolation theory is a mathematical and statistical model that describes the behavior of networks. Much of this work focuses on the connectivity of networks as the individual components making up the network are gradually removed or replaced. Within this theory are percolation limits (or thresholds) which are mathematically defined values or concentrations that destroy a network's long-range connectivity [172]. This concept has be applied to various topics such as wildfire propagation and magnetic ordering in crystalline systems. In the latter, magnetic atoms are systematically replaced from the magnetically ordered network to understand the forces that drive the phase transition towards absolute zero. The particular concentration where phase transition becomes a quantum phase transition is called the critical concentration, x_c, (percolation limit). To better understand this concept we can examine
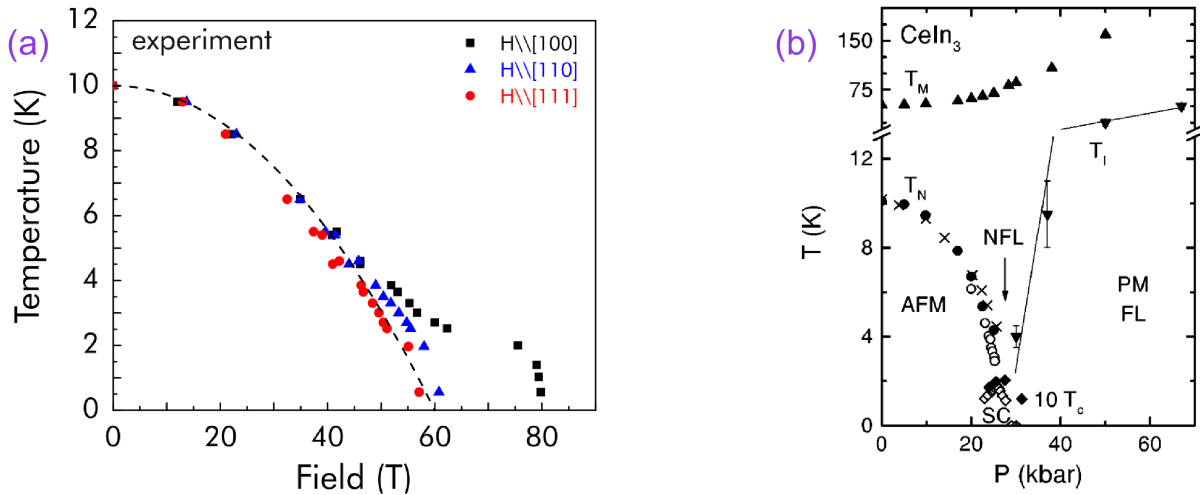
Figure 2.14: (a) Magnetic field phase diagram of CeIn$_3$ when the external magnetic field is aligned along various directions of the CeIn$_3$ crystal. At high fields, $\mu_0 H \approx 40$ T, the phase diagram when $\mu_0 H \parallel$ [100] separates from the other directions. Plot was originally published in [163]. (b) Pressure phase diagram of CeIn$_3$. T_M indicates the resistivity maximum, T_N the Néel temperature, and T_1 the crossover temperature to the Fermi-liquid regime. The superconducting transition T_c is scaled by a factor of 10. Plot was originally published in [158].

an example of La substituted into the Ce$_m$Rh$_n$In$_{3m+2n}$ ($m = 1, 2; n = 0, 1$) family [104].

Each of the three structurally related compounds, CeIn$_3$, CeRhIn$_5$, and Ce$_3$RhIn$_5$, contain an AFM ordering at low temperatures. By systematically substituting Ce with a non-magnetic ion, La, we can understand the driving forces that suppress the AFM order by comparing the experimental La x_c with the theoretical percolation limit. For the tetragonal systems, CeRhIn$_5$ and Ce$_3$RhIn$_5$, x_c of La extrapolated to $x = 0.41(5)$ and for the cubic unit cell, CeIn$_3$, x_c extrapolated to $x = 0.63(5)$ [104]. At first glance, this difference might seem odd because the theoretical percolation limit for a simple 3D cubic system $x_c \sim 0.7$, which was in reasonable agreement with CeIn$_3$ [172]. This discrepancy was ultimately rationalized by the structural differences between the tetragonal and cubic unit cells. The

36
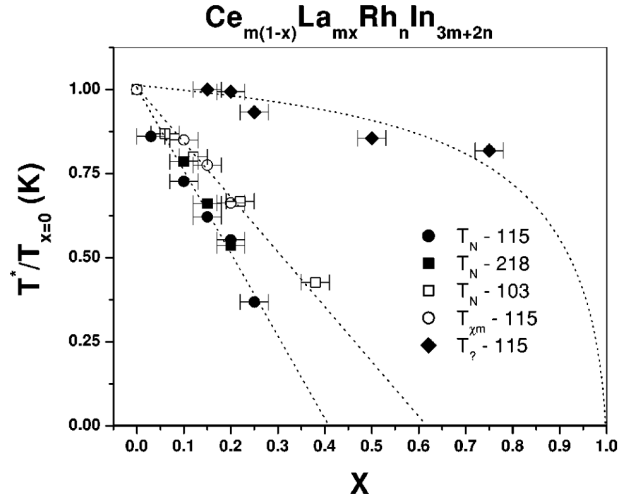
Figure 2.15: Normalized T_N values to show the dependence in the $(Ce_{1-x}La_x)_m Rh_n In_{3m+2}$ $(m = 1, 2; n = 0, 1)$ compounds. Figure was originally published in [104]

two tetragonal systems contain planes of Ce atoms and therefore are more akin to a 2D system. The x_c values for these two systems are now in good agreement with the percolation limit for a 2D $x_c \sim 40\%$ [173]. Since all of the materials agree with their respective percolation limits, it was concluded that no additional mechanisms were suppressing the AFM ordering beyond percolation interactions. However, in Nd substituted $CeRhIn_5$ the critical concentration extrapolates to $x = 0.2$ [105]. The difference between La and Nd critical concentrations in substituted $CeRhIn_5$ indicates that the Nd substitutions have an additional mechanism suppressing the AFM ordering of $CeRhIn_5$. The authors of this work suggest the additional mechanism to be crystal-field induced magnetic frustrations stemming from the AFM ordering difference between $CeRhIn_5$ and $NdRhIn_5$ [105]. Performing these substitution studies provides insights into the mechanisms that suppress an ordered state and allows us to determine the existence of a quantum critical point and/or novel condensed matter states.

Chapter 3

Overview of Experimental Techniques

Copyright permission has been obtained and granted to use Figures 3.1, 3.6, 3.8, 3.9, 3.20(a), 3.22, and 3.23. Figure 3.16 was obtained from an open access source. Figure 3.15 was published within [174] and figures 3.18 and 3.19 were published within [175]. For both articles I was a participating author.

3.1 Sample Synthesis

3.1.1 Flux Growth

Within the condensed matter physics and solid state chemistry communities there are a variety of methods to grow materials in various morphologies. For the purposes of this research, the samples are best studied when grown as high-quality single crystals. As the case before, there are several general methods towards growing single crystals. The most widely applicable method to grow single crystals is through the flux technique. The general mechanisms behind this technique have been well studied and established [176–181]; with

countless examples of materials grown through this method. Here I will describe a brief overview of the mechanisms behind flux growth, how to determine whether a material can be grown via the flux technique, how to go about performing a flux growth, and some precautions to note during the preparation and growth periods. Then I will provide examples of how I performed flux growth syntheses to grow $CeIn_3$ and $LaNiGa_2$. Since the flux technique can grow a wide variety of materials, I will focus on how this technique can be used to grow intermetallic compounds specific to our research in the Taufour group. More details of this technique can be found in a variety of resources [176–181]. Additionally, more information about phase diagrams can be found directly in the ASM handbook [182].

Mechanisms of Flux Growth

Before talking about how a flux technique is performed, let us first focus on how the crystals are grown. One of the most important driving forces for crystals to grow with this technique is supersaturation [181]. At a particular temperature when any solution is formed there is a thermodynamically-stable maximum concentration of a particular solute that can be achieved. Once the solution reaches this concentration it is said to be saturated. For most solutions when the temperature increases, the saturation concentration also increases. When the temperature is lowered for a saturated solution the solute does not immediately drop out to lower the concentration. Instead the solution enters a metastable state called supersaturation. Where the supersaturation can be quantified as: $\sigma = (C_0 - C)/C$ with C_0 being the saturation concentration at a particular temperature and C the current concentration of the solution.

Even within a supersaturated state the crystals will not immediately form. It is not until a particular threshold of σ will crystals begin to nucleate to drive σ down and form a

thermodynamically stable solution. Therefore, to maintain the driving force behind crystal nucleation and/or growth, the solution must remain in a supersaturated state.

When σ reaches a particular threshold and enough atoms randomly cluster together at a critical size, the compound will start to nucleate. Theoretically, nucleation occurs randomly throughout the solution. However, in real syntheses, with crucibles and impurities, the nucleation energy barrier is lowered by the heterogeneous growth medium; leading to clusters nucleating on the imperfections. It should be noted that in general nucleation requires a higher supersaturation state than attaching additional atoms to a nucleated crystal. Therefore to reduce the number of nucleation sites and grow larger crystals the supersaturation state must be slowly changed. A slow supersaturation change can be achieved by slowly cooling the reaction temperature. Additionally, slow cooling can have the additional benefit of reducing disorder and imperfections within a crystal.

It should be noted that supersaturation concentrations, rates of nucleation, and rates of crystal growth are extremely difficult to experimentally determine for any given system. Therefore, these concepts are good to qualitatively understand as a guide to performing flux growth.

How to Determine if a Material can be Grown via Flux Growth

There are two main types of flux growths that can be performed: a self-flux and an external flux. The self-flux technique uses a specific atomic percentage of elements from the desired compound (e.g. using 97% In and 3% Ce to grow $CeIn_3$ as will be discussed later). While an external flux growth uses another element to dissolve the starting reactants of the desired phase. Regardless of the which flux method is used the basic premise of the technique remains the same: force the elements into the liquid phase to create a solution, lower the

temperature to create a supersaturated solution, and continue slowly cooling down to allow crystals to nucleate and grow.

Starting with the self-flux technique, I will use a case study with $CeIn_3$ to show all the necessary steps. To avoid blindly attempting to grow the material it is best to first look up the phase diagram between the elements within the desired material [182]. The general technique can also be used on ternary and quarternary materials. Although there are much fewer of these phase diagrams, making the self-flux growth of these materials much more challenging.

The Ce-In phase diagram acquired from [182] is shown in Fig 3.1. This phase diagram shows all of the known binary compounds as the atomic percentages shifts from 0% In (100% Ce) to 100% In (0% Ce). The vertical lines (solidus lines) represent all of the materials between Ce and In. As can be seen, some vertical lines show a width (e.g. (Ce) ht1, and Ce_3In) which represents a solid solution where the specific material has range of possible atomic compositions. The shaded blue region at the top of the figure shows where the elemental mixture forms a liquid and the line at the edge represents the liquidus line where a solid starts to nucleate. In the case of $CeIn_3$, this material has a exact composition of 25% Ce and 75% In. Between solidus lines (e.g. $CeIn_2$ and $CeIn_3$ and below $1120\,^{\circ}C$) both phases would exist concurrently and there would be a mixture of the two phases. A mixture of phases also occurs in regions between solidus and liquidus lines. For example, the white region to the right of $CeIn_3$, excess In region, where a wide range of atomic percentages will result in mixture of $CeIn_3$ and a liquid ($T = 157 - 1180\,^{\circ}C$).

As can also be seen, pure $CeIn_3$ congruently melts straight into a liquid. Thus $CeIn_3$ could be grown by mixing exact atomic percentages of Ce and In and heating above the melting point, $1180\,^{\circ}C$, and allowing the system to cool down. However, in this scenario

upon dropping below the melting point there will be a rapid transition from liquid to solid and result in a polycrystalline sample of CeIn$_3$. Therefore, to grow high-quality single crystals it is imperative to form a supersaturated solution and then slowly cool down the reaction. For the self-flux growth technique this is done by going off stoichiometry of the desired phase and heating above the liquidus line. The liquid is then cooled down below the liquidus line to induce nucleation of the desired phase. Once nucleation starts, the reaction then contains a mixture of the desired phase and the supersaturated solution.

Going off stoichiometry of CeIn$_3$ there are two possibilities: excess Ce or excess In. Given the small temperature window ($T = 1120 - 1180\,^\circ\mathrm{C}$) where a mixture of CeIn$_3$ and a liquid exists, it is difficult to grow large single crystals in this region. Whereas, when the system has excess In, there is a large temperature window where the mixture exists which provides a large region to grow single crystals. Therefore, to grow single crystals of CeIn$_3$ via the self-flux technique one would set up a reaction with excess In ($75\% - 100\%\,\mathrm{In}$), heat the system above the liquidus line, and then slowly cool down as the system drops below the liquidus line to form single crystals (see below for exact temperature profile to grow CeIn$_3$).

Once the single crystals have been formed, it is important to isolate them to more easily access the samples and subsequently measure their properties. If one were to continue cooling down the reaction to room temperature, the crystals would continue to grow until the freezing point of the flux is reached. This would encase the samples and make them very difficult to extract. So to avoid this disaster, a porous barrier can be added to the reaction vessel and with the help of a centrifuge the molten flux can be forced through the barrier to separate the desired single crystals and the liquid. More will be discussed in the section 3.1.1 on the setup to achieve this.

Since experimentalists are not perfect (although some may disagree) and in-situ centrifug-
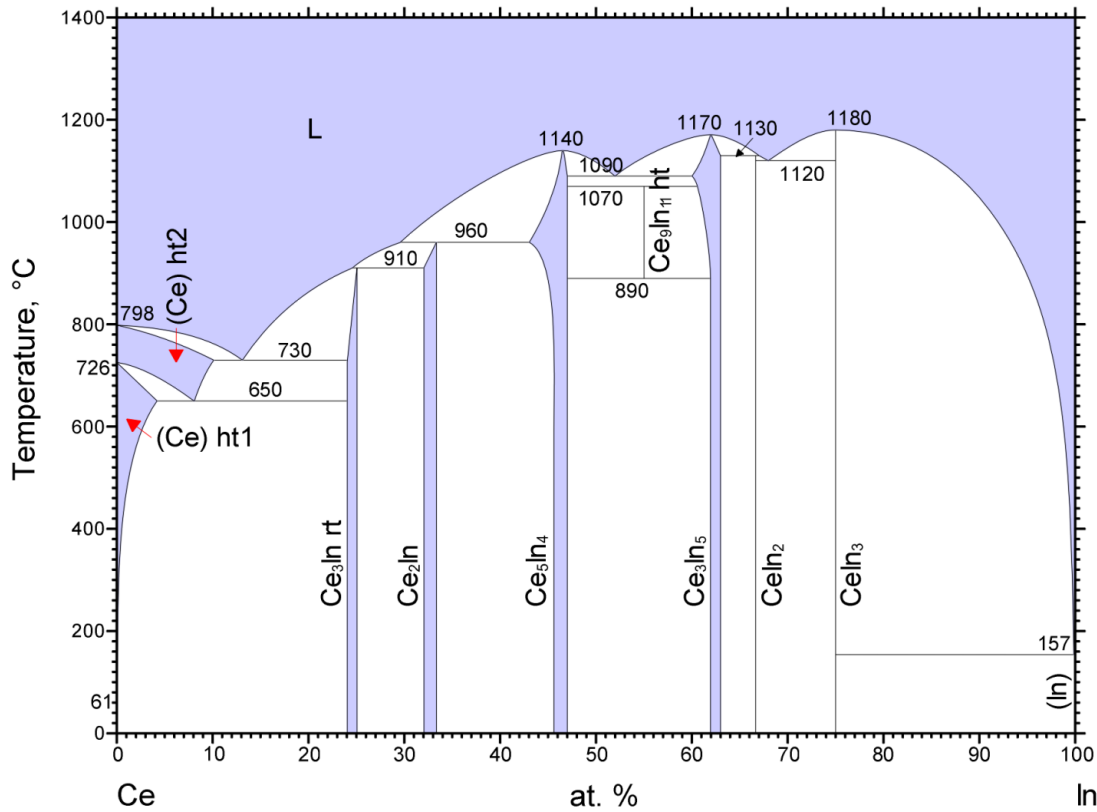
Figure 3.1: Ce-In phase diagram that ranges from an atomic percentage of 0% In (100% Ce) to 100% In (0% Ce). The vertical lines represent the known binary compounds between Ce and In. Figure was originally published in [182].

ing is extremely difficult, we can not centrifuge the sample directly at the freezing point of the flux ($157\,^{\circ}$C for the $CeIn_3$ growth). Therefore, a temperature buffer must be built into the reaction temperature profile. This allows for the reaction vessel to be removed from the furnace and immediately placed into a centrifuge. Typically this buffer is about $\sim 50\,^{\circ}$C. This temperature buffer again verifies that the Ce excess route to grow $CeIn_3$ is prohibitively difficult and not the preferred method to grow the desired phase.

If a self-flux growth proves futile, then an external flux growth could be attempted. In these scenarios the external flux is an element or compound that is not part of the desired phase. For these reactions the external flux is used to dissolve the reactants. Forming a solution with the reactants enables them to interact in the liquid phase and form a super-saturated solution.

For successful growths, the external flux must exhibit three key properties. One, the chosen flux must have a low melting point and a high boiling point to maximize the temperature range where the flux is a liquid. This large temperature range thus provides a large growth window for the desired phase. Two, the external flux must be able to dissolve the reactants of the desired phase. Three, the external flux must not produce any undesirable side-reactions with any elements of the desired phase. In general it is also desirable to use external fluxes that are cheap and nontoxic.

It is possible to use a compound or eutectic mixture for external flux growths (e.g. single crystal FeSe flux growth [183–185]), however I will focus on elemental fluxes to grow intermetallic compounds. The first desired property really limits the number of possible elements down to five main 'usual suspects': Ga, In, Sn, Pb, and Bi. Each of these elements have relatively low melting points ($< 350\,^{\circ}\text{C}$) and boiling points above the temperature limit for quartz ampoules ($> 1200\,^{\circ}\text{C}$). See Table 3.1 for melting and boiling points of the 'usual suspect' fluxes. These large temperature differences between the melting and boiling points provide a large growing window for the desired phase. Other elements can be used as possible fluxes, however these have much narrower temperature windows where they are a liquid or have other potential problems (e.g. Al attacking quartz) [176, 178, 181].

It is usually difficult to predict exactly which flux will produce the best results but the options can be further limited by checking the binary phase diagrams between the flux and

44

Flux	T_{melt} (°C)	T_{boil} (°C)
Ga	30	2400
In	157	2072
Sn	232	2602
Pb	327	1749
Bi	272	1564

Table 3.1: Melting and boiling temperatures of the 'usual suspect' metallic fluxes. Table adapted from [181]

the reactants. These binary phase diagrams will indicate whether the metallic flux is miscible with the solute or if there are any possible side reactions to form an undesirable phase. Along these lines it should be noted that these growths are typically prepared with heavily excess amounts of solvent ($> 90\%$ metallic flux) to minimize the possibility of side reactions. After examining the phase diagrams and it appears that multiple metallic fluxes could be options, it can sometimes be beneficial to try several different growths to best determine which is optimal for the desired phase.

Setting up the growth

To create a uniform growing environment, the elements are placed in an alumina Canfield crucible set (see Fig. 3.2(a)) [186]. This setup has been specifically designed and optimized for flux growths. The bottom crucible acts as the 'synthesis crucible' where the single crystals are grown, the middle frit acts as the porous barrier that allows for the molten flux to be removed during centrifuge, and the 'catch crucible' is where the liquid is pushed into during centrifuging. Therefore, prior to centrifuging the ampoule must be inverted in order for the flux to be separated from the single crystals.

Once the elements have been weighed and placed in the synthesis crucible, the setup must then be placed within a vessel to contain the crucible set. Additionally, since many of
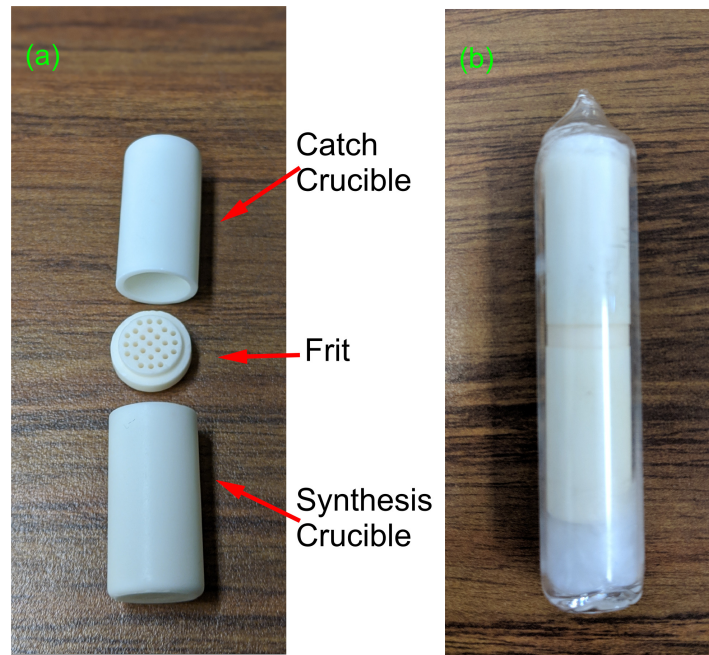
Figure 3.2: (a) Alumina Canfield crucible set which contains the synthesis crucible (bottom) where the elemental mixture is placed, the frit, and the catch crucible [186]. (b) The crucible set sealed within an evacuated quartz ampoule.

the elements and compounds oxidize at high temperatures, the most important aspect when performing an intermetallic flux growth is to ensure that the environment is oxygen free. Both of these necessities can be achieved by sealing the reaction within an evacuated sealed quartz ampoule as shown in Fig. 3.2(b). This can be accomplished by using a torch (using either natural gas or hydrogen as the fuel) to carefully create and seal the quartz ampoule.

Once the ampoule has been sealed, it is placed within a larger crucible to hold the reaction vertical. Subsequently it is placed within a furnace which has been pre-programmed with the previously planned reaction profile (see below for examples). Once the furnace has completed the reaction cycle the ampoule must be centrifuged. While wearing the proper PPE, you can quickly and carefully remove the larger crucible, containing the ampoule, from the furnace

with tongs. Then in a swift motion the larger crucible is inverted to slide the ampoule into the centrifuge. Once the ampoule is in place the centrifuge is turned on and the molten flux is separated from the crystals. In the end, the ampoule can be broken open to reveal crystals in the synthesis crucible.

Precautions

There are a variety of precautions that need to be taken into account when performing a flux growth. Some are small tricks that can ultimately improve the single crystal quality. While others are more dire and if not properly accounted for can result in catastrophic failure and potential injury.

Starting from the beginning, some elements are inherently more hazardous due to innate health properties (e.g. arsenic, cadmium, beryllium). So if these elements are used within growths, additional precaution must be taken throughout the entire synthesis. Such safety measures include weighing the reactants in a glovebox and using a furnace within a fumehood.

Others elements are dangerous because of their melting and boiling points. Since these reactions are performed within a closed environment and the elements are ultimately melted, under certain circumstances vapour pressures can cause the ampoule to explode. This could lead to the vapours escaping into the room and potentially causing severe health issues while also damaging the furnace. To avoid this situation, the vapour or gaseous pressures from elements with low boiling points (e.g. phosphourous, sulfur, selenium) or that sublimate (e.g. arsenic, iodine) should be calculated at the highest temperature. Although the quartz ampoule can withstand a small amount of positive pressure, it is best practice to use atmospheric pressure as the maximum pressure. With the maximum temperature and pressure the amount of starting material from these elements can be calculated for these reactions.

Additionally, if there is ever a possibility of an explosion the reaction should be placed within a furnace in a fume hood or have a setup that allows for the vapours to quickly be evacuated from the room.

On the other end of the temperature spectrum, are elements which do not melt under the temperature limits of the quartz ampoule. Quartz does not have well defined melting point, but rather begins to soften around 1250 °C. Therefore, the upper limit that the quartz ampoule can be taken is 1200 °C. Which means that several elements will not form a liquid at this temperature and subsequently would be omitted from flux growth reactions.

There are a couple methods to get around this dilemma. One is to arc-melt some or all of the elements to form a eutectic mixture with a lower melting point (a necessary step to synthesize single crystals of LaNiGa$_2$, see below for more details). Another method is to use a powder of the high-melting point element. Using a powder increases the surface area interactions between the high-melting point and the liquid flux. So during the synthesis set up, this powder is dispersed throughout the synthesis crucible and encased by the lower melting flux. With enough time at the maximum temperature and having correctly chosen a flux, the powder will eventually dissolve entirely into the molten flux. Ultimately forming a solution and allowing for the desired phase to precipitate out.

For certain reactions, the alumina crucible and/or quartz ampoule can prohibitively cause undesired side reactions. Some elements (e.g. yttrium) can react with the alumina crucible (Al$_2$O$_3$) to induce the highly exothermic thermite reaction:

$$M + Al_2O_3 \longrightarrow M_xO_y + Al \tag{3.1}$$

This reaction only takes place with elements with really high oxidation-potentials where the alumina crucible oxidizes the element and in the process releases an extreme amount of heat.

48

To combat this, the alumina crucible can be replaced with a highly stable metal like tantalum or platinum. In a similar regard, the silica quartz ampoule can react with certain elements that are highly reactive and also have high-oxidation potentials (e.g. Al, alkali metals). In these scenarios the reaction would deteriorate the structural integrity of the quartz ampoule. Although this can generally be avoided by using a synthesis crucible as a barrier between the reaction and the quartz. For growing both $CeIn_3$ and $LaNiGa_2$, it was discovered that an alumina crucible works perfectly well and neither of the syntheses react with the alumina.

Lastly, once the flux growth is underway the temperature gradient within the furnace itself can have a dramatic impact on the growth of the crystals. Although the temperature control system may state that entire volume of a furnace is at a uniform temperature, convection currents and temperature gradients will always occur and vary between furnaces. These factors do not really play an impactful role on the safety of a growth but they can greatly influence how the crystals grow and the properties of said crystals. More will be discussed later on the specific synthesis of $LaNiGa_2$ single crystals but it was discovered that the furnace gradient greatly impacts how the single crystals grow. Fig. 3.3 shows the growth difference between batches grown at the same time, within the same furnace, and with the same starting atomic percentages. The high-quality crystals in Fig. 3.3(a) (batch JB386) come from an ampoule that was positioned in the center of the furnace and these crystals exhibited properties that comport with the best crystals. Whereas the terraced and stacked crystals in Fig. 3.3(b) (batch JB389) were grown near the furnace door in the front and shown to exhibit worse physical properties (lower RRR and T_{sc} values).
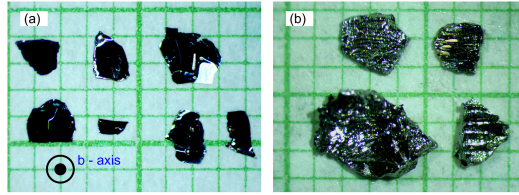
Figure 3.3: (a) High quality crystals of LaNiGa$_2$ grown from an ampoule that was positioned in the middle of the furnace. (b) Terraced and stacked LaNiGa$_2$ crystals grown from an ampoule that was positioned near the front door of the furnace. Both ampoules were set up and ran together at the same time and in the same furnace.

Self-Flux Growth for CeIn$_3$

All self-flux growths for CeIn$_3$ were performed with 97% In (99.99%) and 3% Ce chunks (99.996%). This atomic percentage was selected because it lowered the melting point of the mixture such that sample did not need to be heated up to 1200 °C while providing a large temperature growing temperature, reduced the amount and cost of Ce needed, and increase the size of the crystals by reducing the amount of nucleation. After weighing the appropriate atomic percentage, the metals were placed together in the bottom crucible of a Canfield crucible set [186]. For each synthesis, the alumina crucible set was sealed in an evacuated quartz ampoule and then heated up to and held at 1050 °C for 5 hours. After which the reaction was slowly cooled down to 300 °C over a period of $80 - 100$ hours to allow for adequate growth of large single crystals. Once at 300 °C the ampoule was then quickly centrifuged to remove the excess In-flux. After breaking open the ampoule and shiny, silver, block-like single crystals ranging from $1 - 3$ mm were grown in the bottom crucible (Fig. 3.4).

50

Figure 3.4: Single crystals of CeIn$_3$ on millimeter paper.

3.1.2 Arc-Melting

As mentioned in section 3.1.1, the primary goal of this research centers around growing single crystals. Although arc-melting is a standard method to grow polycrystalline samples, it nonetheless is a a crucial technique that can ultimately lead to growing single crystal samples.

Typically arc-melting is performed by taking stoichiometric amounts of elements for the desired phase and placing them on a water-cooled copper hearth in a vacuum-tight chamber. The chamber is then purged and vented with argon gas several times to knock off adsorbed gas molecules and remove all of the oxygen within the system. Once purged of the oxygen the chamber is backfilled with argon gas to create an oxygen-free environment for an arc to form. Employing a welding power supply an arc is first struck with the water-cooled tungsten tip on a zirconium button. When molten, the zirconium acts as an oxygen-getter and further removes any residual oxygen from the environment. After completely removing all oxygen, an arc is then struck over the reaction to melt the elements of the desired reaction. Since there is no way to control the cooling of the reaction, a polycrystalline boule will form. Once cooled, the boule should be flipped and melted again. This flipping ensures the elements are

51

evenly dispersed to form a homogeneous mass.

For synthesizing single crystals, the arc-melting technique can be employed to form a eutectic mixture with really high-melting point elements. As discussed earlier, dispersing powders of the high-melting point elements throughout the flux material could coax the high-melting point element to dissolve into the liquid phase. However, this method is not full-proof. Arc-melting the reactants together, if the elements are miscible, will almost always cause the elements to mix and react. Since there is a hard temperature limit to the quartz ampoules, arc-melting a precursor boule with the high-melting point element can be a beneficial step for single crystal synthesis. This can cause the high-melting point element to mix with the other element(s) to form a eutectic mixture with a melting point below the $1200\,^{\circ}$C limit. In the end, this lower melting point eutectic mixture can allow for a subsequent flux growth to occur.

As mentioned earlier, this was done for the single crystal synthesis of $LaNiGa_2$. Since nickel has very high melting point ($2913\,^{\circ}$C) it was arc-melted to form a precursor boule with lanthanum and gallium. After some tests it was determined that the melting point of the eutectic mixture is below $1150\,^{\circ}$C. Allowing for the self-flux technique to be used to grow single crystals of $LaNiGa_2$. More will be discussed on the exact stochiometry and reaction profile of this synthesis later.

A couple notes to that should be taken into account when performing an arc-melting growth. Since a high-voltage arc is used to melt the starting elements, the reactants must be able to conduct electricity. In some cases innate semiconductors (e.g. silicon, germanium) may be included in the arc-melted mass. Although precaution must be taken and a well thought out plan must be followed, otherwise the semiconducting material might cause small 'explosions' like popcorn on a stovetop. This would contaminate the arc-melting chamber

and ruin the stoichiometry of the reaction. One method to alleviate this issue is to use powder starting materials and press a pellet containing both the metallic and semiconducting elements. This ensures that there is a conductive path for the current to follow while also heating up the semiconducting reactants. Once the semiconductor mixes with the metallic elements, typically there is no further issue re-arc-melting the boule because an electrically conductive intermetallic phase(s) is/are formed.

Another area of concern are when using elements with 'low' boiling points. Given the nature of this technique, it is difficult to get a precise maximum temperature that be achieved. Since the arc-melting technique is able to melt almost every single element, the samples are exposed to extreme temperatures. So when using elements with relatively 'low' boiling points ($< 2000\,°C$ e.g. Zn, Cd, alkali metals) the arc should be used long enough for the elements to mix. Otherwise you run the risk of boiling off the element and forming a thin layer of said element throughout the chamber when it condenses.

Lastly, since hot metals (at least when they are not glowing) look no different than cold metals it is often difficult to know the exact temperature of the boule after arc-melting. Therefore, to avoid any cross-contamination with the tungsten electrode it is extremely important to allow both the boule and the tip to completely cool down (minimum 5 minutes) prior to flipping it. This minimizes the possibility of any side products from forming in the boule. This is also true before removing the sample from the chamber entirely. If the vacuum chamber opened preemptively then you run the risk of oxidizing the sample and ruining your work.

53

Arc-melting and Flux Growth for LaNiGa$_2$

Single-crystalline samples of LaNiGa$_2$ were grown with a Ga deficient self-flux technique. Ga (99.99999 %) atomic composition ranged from $32-36\%$ Ga and the remaining percentage was equally split between La (99.996 %) and Ni (99.999%). Precursor ingots were first synthesized by arc melting all the elements in an argon environment. The ingots were subsequently loaded into an alumina Canfield crucible set [186] and sealed in an evacuated quartz ampule. The material was heated up to 1150°C and held at temperature for several hours. The reaction was then slowly cooled down to 800°C over 100 hours and then quickly centrifuged. In the end high-quality single crystals were synthesized and characterized (see Figs. 3.3,3.5).

It was noted that different starting Ga percentages did not produce a noticeable difference in crystal quality, as evaluated by the residual resistivity ratio (RRR). However, larger single crystals (up to 7 mm) were obtained in the more Ga deficient syntheses. It was also discovered that the superconducting properties were highly sensitive to oxidation throughout the reaction. Additionally, as discussed above, growths were extremely susceptible to small changes of the thermal gradient within a furnace. For the most successful growths of LaNiGa$_2$, the reactions were performed in the furnace 'Haddock' and the ampoule was placed precisely in the middle of the furnace. If the ampoule was place centimeters (roughly 5 cm) closer to the door, then the crystals would come out terraced, as discussed above. Lastly, in more Ga deficient growths, below 32 %, no crystals were obtained when the reactions were centrifuged at 800 °C

3.1.3 Vapor Transport

Oftentimes when a flux growth proves to be futile, alternative synthesis routes can provide a pathway towards growing the desired material. The vapor transport method can be one
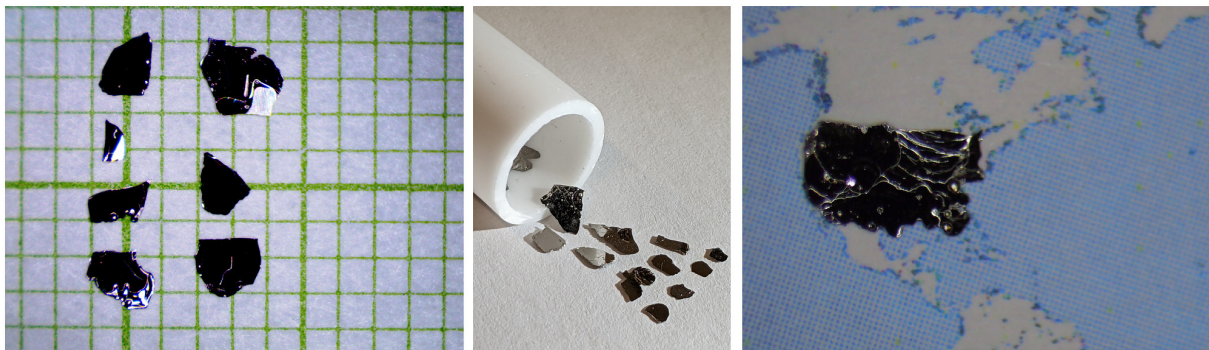
Figure 3.5: Single crystals of LaNiGa$_2$, including one that looks like the shape of the United States of America.

fruitful method to grow materials which have difficult flux approaches as a result of a complex phase diagram, like β-FeSe (See Fig. 3.6) [187–191]. Or when the flux method produces single crystals with poor quality samples, in the case of UTe$_2$ [53, 55, 192]. This method is also quite common to grow materials which contain nonmetals, such as chalcogenides and pnictides, where low boiling points or sublimation can be prohibitive barriers for flux growth.

The optimized synthesis described by Böhmer et al. [191] was replicated here at UC Davis and ultimately provided the samples for collaborative work with Nick Curro [193]. Below will be a brief overview of the vapor transport method. More details about this method can read up in the following sources [194–197].

There are several necessary components to a vapor transport growth: a solid source, vapor transport agent, chemical reaction, deposition site (sink), and most importantly a thermal gradient. These reactions take place within a closed system, making a sealed quartz ampoule of sufficient length a perfect vessel to contain the reaction (see Fig. 3.7(a)). The basic premise is that during the reaction, the source side, containing stoichiometric amounts of elements for the desired phased, is heated up such that a chemical reaction occurs between the transport agent, typically a halide or halogen, and the source materials. This chemical
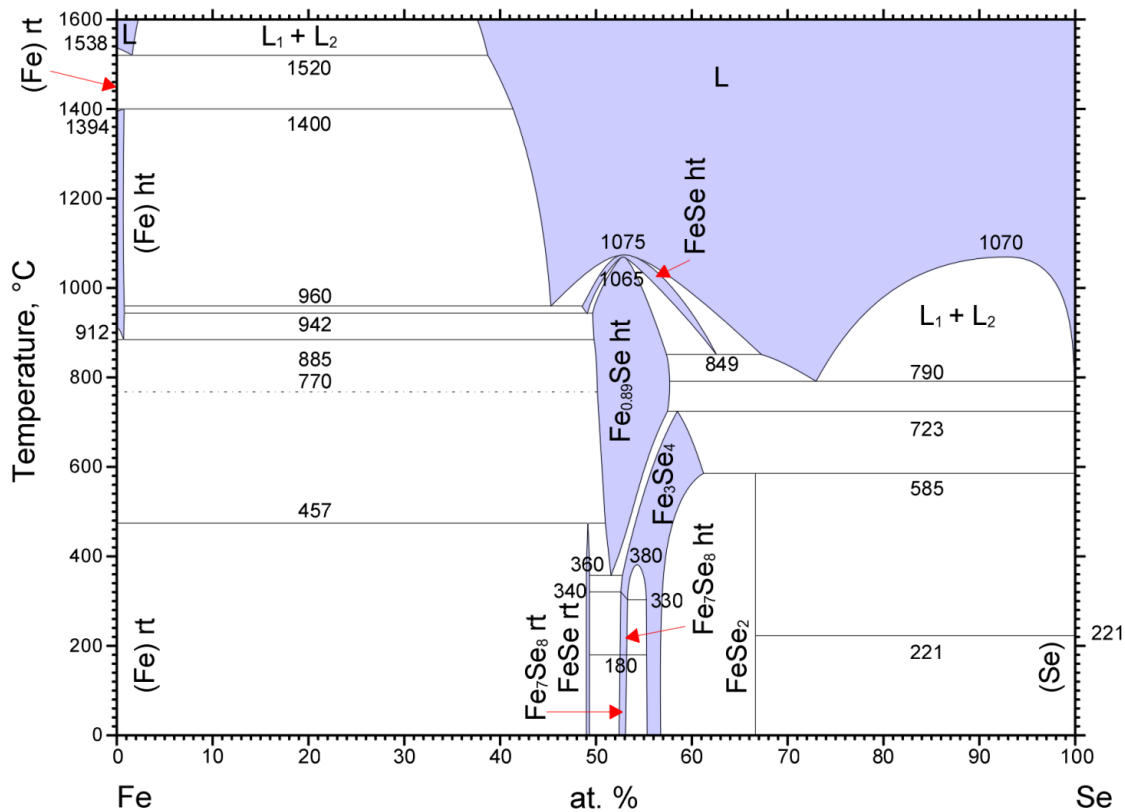
Figure 3.6: Fe-Se phase diagram that ranges from an atomic percentage of 0% Se (100% Fe) to 100% Se (0% Fe). This phase diagram shows that it is not possible to use the self-flux technique to grow β-FeSe (FeSe rt). Figure was originally published in [182].

reaction produces the gaseous transport effective species. The thermal gradient of the reaction then causes the transport effective species to travel to other end of the quartz ampoule and another chemical reaction occurs. This reaction deposits the desired material onto the surface of the quartz and the vapor transport agent cycles back to source side, perpetuating the reaction cycle. With sufficient time, single crystals can start to protrude from the quartz wall (Fig. 3.7(b)).
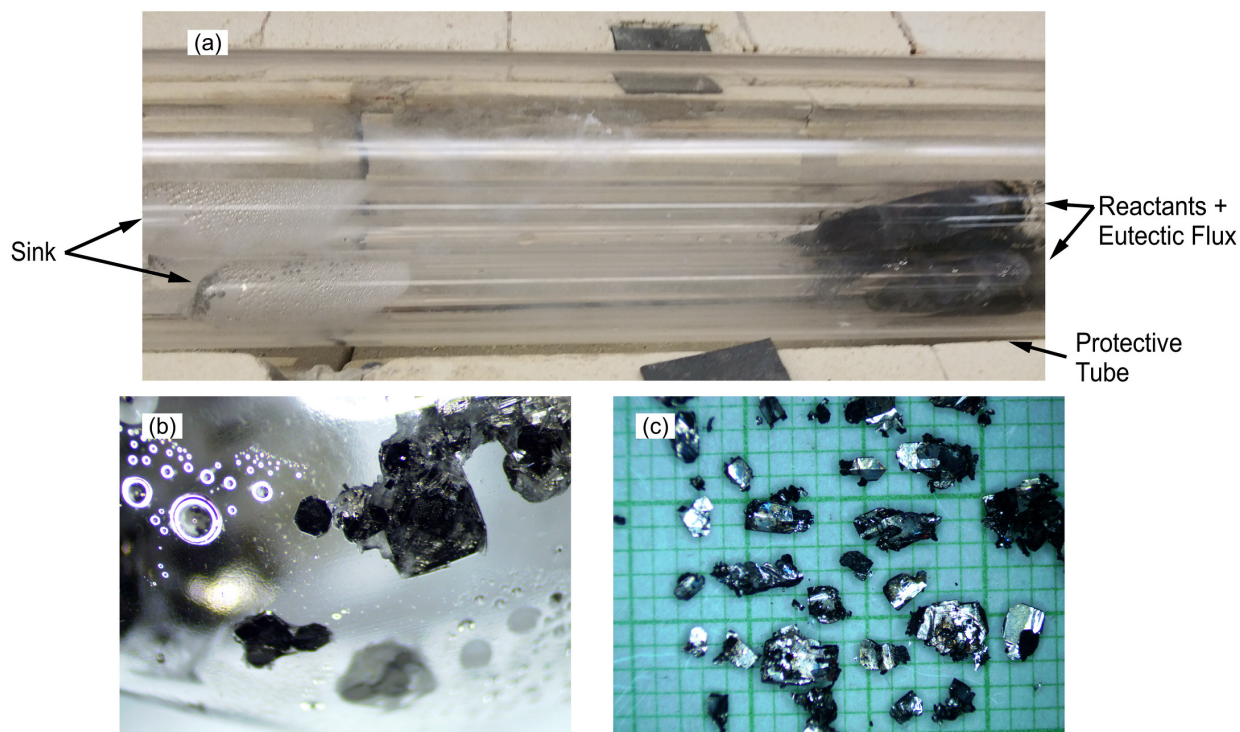
Figure 3.7: (a) Several ampoules set up for β-FeSe vapor transport growth. The reactants and eutectic flux are placed on the right side of the ampoule at the hot end $(390\,°\text{C})$. The transport effective species travels to the cold end $(350\,°\text{C})$ to deposit the β-FeSe single crystals at the sink. (b) Close up view of the crystals within the ampoule after the growth. (c) Extracted single crystals of β-FeSe on millemeter paper.

Given the inherent nature of this synthesis method and the number of controllable parameters, it is often extremely difficult to know the exact details about the chemical reactions. Consequently making this method a bit more challenging to plan and prepare relative to the flux growth. This is especially true when determining the proper transport agent and the exact thermal gradient. Despite these hurdles, there are countless examples of successful vapor transport growths.

For the synthesis of β-FeSe the exact reaction differs slightly from the prototypical va-

por transport growth. The first reported method to grow single crystals of β-FeSe was through an external flux growth using an eutectic mixture of NaCl and KCl as the flux [183]. Although this method was successful, the synthesis additionally produced the undesirable hexagonal phase and the resulting tetragonal phase crystals showed lowered superconducting and physical property values. After it was discovered that β-FeSe can be grown via a vapor self-transport method [187], Böhmer et al had the insight to combine the two methods by using a eutectic halide mixture, KCl and AlCl$_3$, as the vapor transport agent. [189]. Typically halogens (Cl$_2$, Br$_2$, and I$_2$) or halide compounds make great vapor transport agents, however eutectic mixtures have mostly been used for horizontal liquid transport growths [198–202].

What differentiates this growth from other vapor transport methods is the eutectic mixture. Traditionally, the transport agent and effective species remain entirely in the gas phase when heated up to the reaction temperatures. However, in this case the eutectic mixture melts to form a liquid and dissolves the elemental reactants. Which then evaporates to produce the transport effective species. This intermediate species then condenses at the sink and slowly deposits the desired phase. Since the transport agent condenses back to the liquid phase, the furnace and quartz ampoule must be performed at an angle during the reaction. Additionally, the reaction is extremely sensitive to the thermal gradient because the transport agent condenses into a liquid [191].

3.2 Structural Characterization

After a successful growth and single crystals are obtained, the first step is to confirm the phase of the material. Phase identification can be achieved through several different methods, but I will focus on the three main techniques done in the Taufour group: powder X-ray diffraction (PXRD), single-crystal X-ray diffraction (SCXRD), and energy dispersive spec-

troscopy (EDS). For each of these techniques, I will cover what information can be gained from the experiments, how to perform the measurements, and a summary of what analyses can be performed from the data. Both PXRD and SCXRD are very detailed techniques with a lot of nuances, where an entire Ph.D.'s worth of research can be focused just on perfecting one or both of these methods. Therefore it is best to read up on each technique before to performing an analysis [85, 203–207].

3.2.1   Powder X-ray Diffraction

What information can be gained?

For intermetallic materials that we grow in the Taufour group, the first and best technique for structural characterization on these materials is PXRD. Using this technique, one can confirm every phase produced in a growth, including the desired phase and any possible undesirable side products. This information can ultimately provide vital insights on any possible changes that need to be made about a particular growth, like starting atomic percentages or altering the growth medium.

Once it has been confirmed that the desired phase has been grown, either amongst several phases or isolated, further details can be obtained about the material's structure from X-ray diffraction as a whole. At the core of X-ray diffraction is Bragg's law (Fig. 3.8). Wherein X-rays are diffracted off of repeating layers of atoms. The exact angle (θ) of the diffraction is then based on the distance between the layers. This fundamental principle can inform experimentalists about the exact location of atoms and symmetry within a unit cell. Moreover, since the X-rays interact with an atom's electron cloud, it is also possible to discern the elements of the diffracted atoms.

These fundamental principles make X-ray diffraction an extremely powerful tool for de-
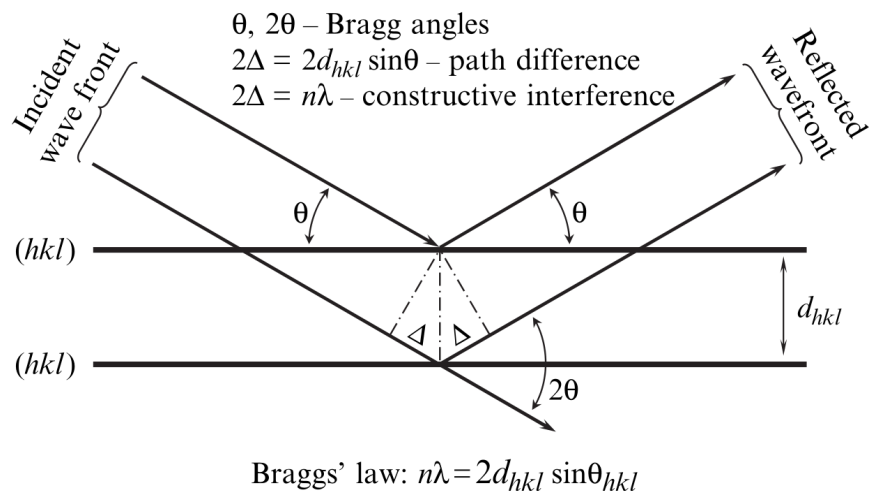
Figure 3.8: Geometrical illustration of Bragg's law. Image was originally published in [85].

termining the studied materials' atomic location and composition. Both PXRD and SCXRD are critical techniques to determine the structural properties of materials. Nevertheless, each method has its niche about what information can be obtained, how fast that data can be acquired, and then how fast can the analysis be performed. PXRD specializes in quickly confirming structures of known materials and can provide insight on bulk structural properties from large amounts of material. The barrier to perform higher-level PXRD analysis is lower than that of SCXRD. However, these analyses still require in-depth knowledge about the technique. Although PXRD is best used to confirm known materials and give some atomic information, it can be used to elucidate structures of unknown materials. However, this does require deep expertise and understanding of the technique as a whole.

The essence of PXRD is in the name. That X-ray diffraction occurs on polycrystalline (powder) samples. When X-rays are exposed to a nearly infinite number of randomly orientated polycrystalline unit cells, the incident light diffracts off of parallel planes of atoms within each unit cell. The angle (2θ) of the diffracted light is then determined by the distance between these planes (d-spacing) — Bragg's law. In PXRD, the diffracted photons
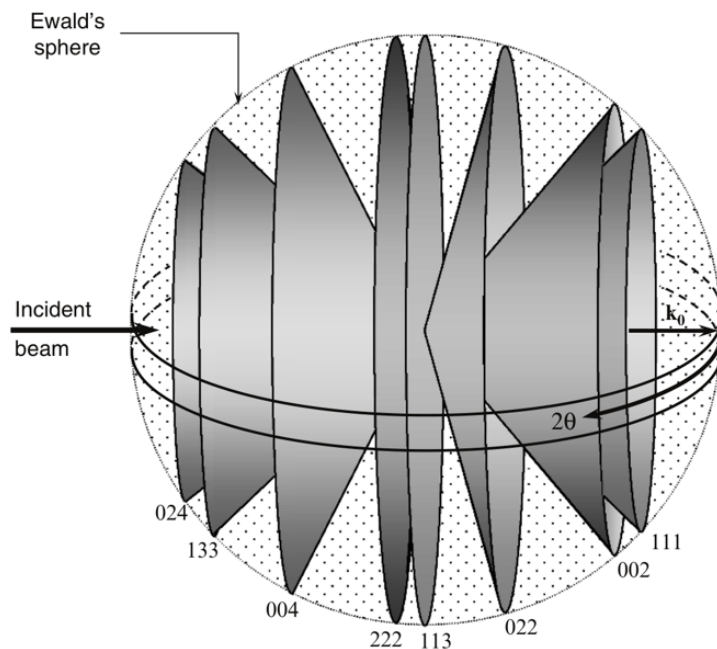
Figure 3.9: Schematic of powder diffraction cones produced in PXRD. The location (2θ) of the cone is dependent upon Bragg's law and the d-spacing of the atomic layers. Image was originally published in [85].

form concentric cones (Fig. 3.9).

The d-spacing of atomic planes within each crystalline sample is determined by the material's space group and unit cell parameters. The intensity of each diffraction then contains information about the atomic positions within the unit cell and the elemental composition of the atoms. By cutting through the cones and scanning 2θ these cones are turned into peaks with a particular peak shape (see Fig. 3.10(a) for a PXRD pattern of CeIn$_3$), providing information about crystallinity, disorder, and defects within the powder. For example, nanoparticle samples tend to have broad peak shapes because there are few repeating atomic planes within the particles.

Since this technique is highly sensitive to atomic positions and elemental compositions, PXRD is perfect for substitution studies. As previously mentioned, chemical substitution can
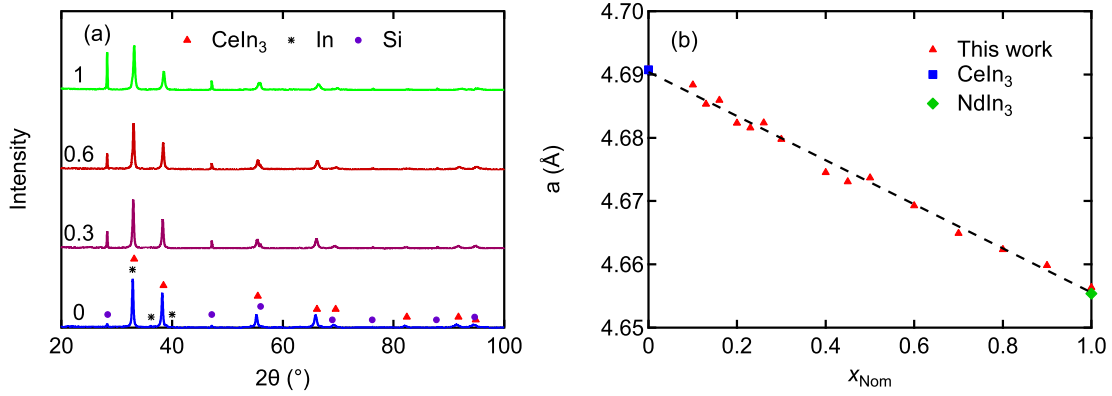
Figure 3.10: (a) PXRD patterns of $Ce_{1-x}Nd_xIn_3$ syntheses confirming the presence of $Ce_{1-x}Nd_xIn_3$ single crystals and In flux. Si powder was added to act as an internal standard. (b) Vegard's law applied towards $Ce_{1-x}Nd_xIn_3$ alloys. This shows that the unit cell parameter a shifts linearly as Nd incorporates into $CeIn_3$.

be a fantastic way to understand low-temperature phenomena near quantum critical points or quantum phase transitions. PXRD is a technique that can be employed to determine whether the substituted atom incorporates into the parent structure and the substitution concentration. If the PXRD pattern does not reveal a new phase and the unit cell parameters shift slightly, it can be confirmed that the external atoms are successfully incorporating into the parent structure. Vegard's law states that as the compounds are increasingly alloyed from one parent structure to the other, the unit cell parameters should be linearly dependent on the substitution concentration [208]. This principle can be used to experimentally and directly determine the concentration of the substituting atom. This was accomplished in $Ce_{1-x}Nd_xIn_3$ alloys (Fig. 3.10(b)).

How to perform the measurements?

To quickly gain the information listed above on freshly grown single crystals, the first step to performing a PXRD measurement is to convert a batch of single crystals into a powder. This
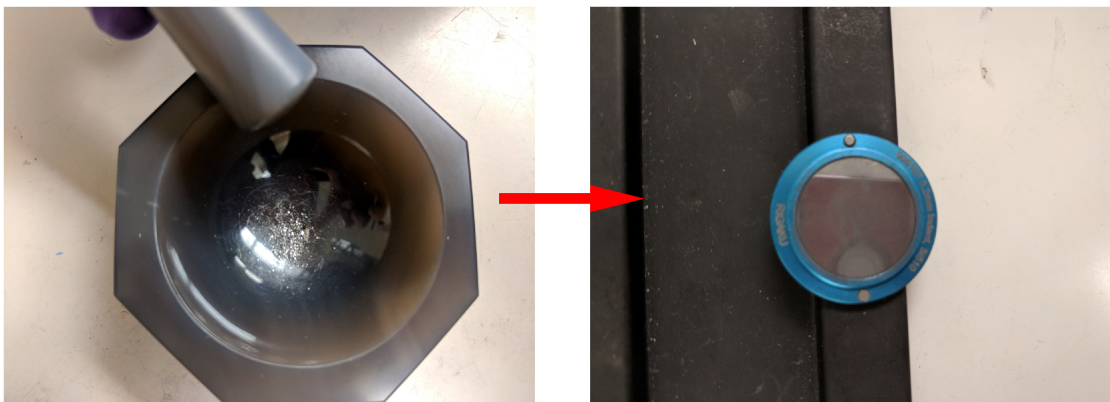
Figure 3.11: Preparing single crystals for PXRD by first grinding them in a mortar and pestle. Once ground to a sufficient powder, a small layer of Vaseline is applied to the puck and subsequently the powder is sprinkled onto puck.

process can easily be accomplished by grinding the crystals in a mortar and pestle until they become a fine powder. Because this increases the surface area of the material, sometimes this action needs to be performed in an inert environment to limit oxidation. If studying a sample from a polycrystalline growth it is still best practice to grind the starting material to ensure uniform particle size and shape.

After grinding the crystals into a powder, the powdered sample can be transferred to a sample puck. Since the sample puck spins during the measurement — this increases intensity statistics — an adhesive is needed to bind the powder to the puck. This can be achieved by applying a thin layer of Vaseline to the sample puck (Fig. 3.11). Once the powder and puck are prepared, the measurement is then ready to be performed.

In order to run a PXRD measurement, a constant wavelength X-ray source is needed. Nowadays, in benchtop PXRD instruments, this is achieved by using a Cu source where the Kβ emission is filtered out to give a high-intensity Kα_1 emission X-ray with a $\lambda = 1.54$Å. In a Bragg-Brentano configuration (most common benchtop configuration), both the Cu

source and the detector collectively travel in the same arc at the same rate. It is good practice to perform the measurements over a wide range ($2\theta = 5 - 100°$) to ensure that as many diffraction peaks are observed. Along these lines and depending upon the sample quality, it is generally good to run slower measurements ($\sim 3\,\text{hours}$) to observe the best possible intensity statistics. However, quick measurements ($\sim 15\,\text{minutes}$) may be run if only performing phase identification.

What analysis can be done?

As mentioned above, PXRD can be used as the primary tool for phase identification. For these simple analyses using software (PDXL by Rigaku) that can compare predicted PXRD patterns from known phases and the experimental data is all that is needed. If the predicted pattern matches that of the data, then it can be confirmed that that phase is present. As shown in Fig. 3.10(a), this was accomplished to ensure that the resulting single crystal alloys of $Ce_{1-x}Nd_xIn_3$ matched the expected pattern for the Cu_3Au structure type. However, if there are multiple phases and/or some of the phases have overlapping peaks, this can make the analysis much more difficult to confirm all phases confidently.

To acquire more potent structural information about the material, it is possible to computationally create a structural model and compare it to the PXRD data (Rietveld refinement). This method is quite challenging and does require expertise to ensure the analysis is performed correctly [85]. Rietveld refinement is accomplished by comprehensively modeling every aspect of the PXRD measurement. Such parameters include but are not limited to wavelength of the X-ray source, Gaussian and Lorentzian peak shapes originating from the instrument, atomic positions, unit cell parameters, strain within the crystallites, and sample displacement. Understanding how each parameter affects the resulting data is imperative

to perform a successful Rietveld refinement. Although this refinement is challenging, this method can provide beneficial structural information about the sample.

If only unit cell parameters are needed —in the case of determining substitution concentration— then performing a simpler whole-pattern Pawley or LeBail fitting is all that is needed. Since the peak locations contain all of information about unit cell parameters these are the only features that are modeled. Therefore the peak intensities are treated as free parameters and contain no actual information about the atomic parameters. This shortcut then simplifies the analysis. For these types of refinements, often, it can be helpful to include one or multiple peak shape parameters to better fit the modeled data to the PXRD data. As an example, whole-pattern refinement was performed on the PXRD patterns of the $Ce_{1-x}Nd_xIn_3$ alloys to produce the plot in Fig. 3.10(b).

3.2.2 Single Crystal X-ray Diffraction

What information can be gained?

As mentioned, information gained from PXRD can also be acquired from SCXRD experiments because both PXRD and SCXRD employ the same diffraction principles. The main difference between the two techniques, aside from sample type, comes down to the ultimate goal of doing a structural experiment and ease of analysis. If the goal is to confirm the structural data of a known system, then PXRD is quick and the analysis is much easier. It does not make much sense to perform this type of analysis using SCXRD because of how much longer these experiments and subsequent analysis require. However, if the structural data of a material is unknown, it can be much easier to determine all the nuances of the unit cell from the SCXRD experiments. Even though SCXRD analysis typically requires more time and expertise to perform successfully.

This conclusion is directly tied to the dimensionality of the resulting diffraction data. As previously highlighted, the diffracted light in PXRD experiments takes the shape of concentric cones. Thus, by scanning across 2θ the resulting peaks merely indicate the d-spacing of repeating planes, making the data one-dimensional, in a sense. However, in SCXRD, the resulting data is three-dimensional. This difference is because diffraction in SCXRD experiments occurs on a collection of unit cells that are all cohesively connected and aligned in the same direction. The diffracted light off of a single crystal produces a single spot for each Miller plane rather than cones (Fig. 3.12). Rotating the sample across 3 angles (ϕ, χ, and 2θ), makes it possible to map three-dimensional diffraction space. In the end, these extra dimensions contain more information that allows us to determine small structural nuances that are not possible with PXRD data.

For example, prior to our work on $LaNiGa_2$ all previous structural experiments were completed on polycrystalline samples [14, 19, 209, 210]. The results from the original Rietveld refinement produced a unit cell with a $Cmmm$ (#65) space group [209]. All subsequent experiments on polycrystalline $LaNiGa_2$ used PXRD experiments and the original structure to confirm that $LaNiGa_2$ was successfully grown. When we pioneered the single crystal growth method for $LaNiGa_2$ we performed SCXRD measurements on a small single crystal to confirm the original structural work. As it turns out, the resulting diffraction data pointed towards a $Cmcm$ (#63) space group. The slight symmetry difference between the two unit cells is almost indistinguishable in PXRD, as evidence by the successful whole-pattern LeBail fittings using both the $Cmmm$ and $Cmcm$ space groups (Fig. 4.6). This example shows the power of SCXRD work and how it can discern small structural details that can be overlooked in PXRD experiments.
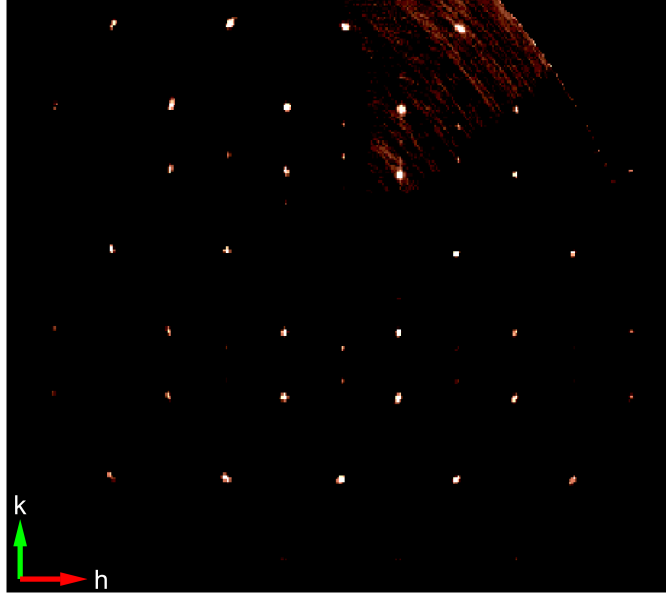
Figure 3.12: SCXRD data showing the diffraction spots. This is a compiled precession image of the $hk0$ plane from a SCXRD experiment on $LaNiGa_2$. Each diffraction spot originates from a particular Miller plane in the $LaNiGa_2$ unit cell.

How to perform the measurements?

The key to performing a SCXRD measurement is growing a single crystal. After successfully growing single crystals, the first step to performing a SCXRD experiment is to find a crystal with the appropriate size. Since we typically grow compounds containing heavier elements and our crystals often 'large' ($\sim 1\,mm \times 1\,mm$) we most often need to break a small piece off from the original crystal. This size restriction is because heavier elements (i.e. elements with more electrons) absorb X-rays at a much higher percentage than lighter elements, which is ultimately why lead blankets are used as shields during medical X-ray scans. Therefore to avoid significant absorption issues, it is best to use the smallest crystal that gives sufficient diffraction intensity. Nevertheless, the size needed for sufficient intensity varies between systems.

Once a sample has been selected, it must first be aligned in the X-ray beam. A proper

67

alignment can be determined by capturing a couple of quick diffraction images. These frames can also be used to determine whether the sample provides sufficient intensity to run a whole experiment and whether it is single crystalline. Once the sample has been aligned and deemed sufficient, a couple of fast sweeps (~ 15 minute) can be collected. These diffraction frames can then be used to calculate a preliminary unit cell. At which point the built-in software (APEX3) can calculate a complete sequence that is needed to collect a sufficient diffraction dataset to resolve the structure conclusively.

What analysis can be done?

After collecting a complete dataset, all of the single crystal's unit cell details can be determined by creating a model that matches the observed data. This is first achieved by scanning through all of the collected frames to harvest all of the spots. Through this harvesting process the software (APEX-3) will collect the intensity and location of each spot. A recreation of the crystal's three-dimensional diffraction space can then created from the library of diffraction spots (Fig. 3.13). At which point the Bravais lattice and lattice parameters of the unit cell can then be determined.

With an initial guess for the unit cell, the spot intensity from the frames needs to be collected into a set of integrated and scaled intensities. After which the intensities need to be scaled to account for the crystal's X-ray absorption. With absorption corrections, the space group can then be determined and ultimately refined to find the atomic coordinates and elemental composition.

The process described above is a very short summary of overall analysis and like Reitveld refinement, this procedure takes an advanced knowledge of the technique and controllable parameters to perform a successful refinement. But once this mastery has been achieved
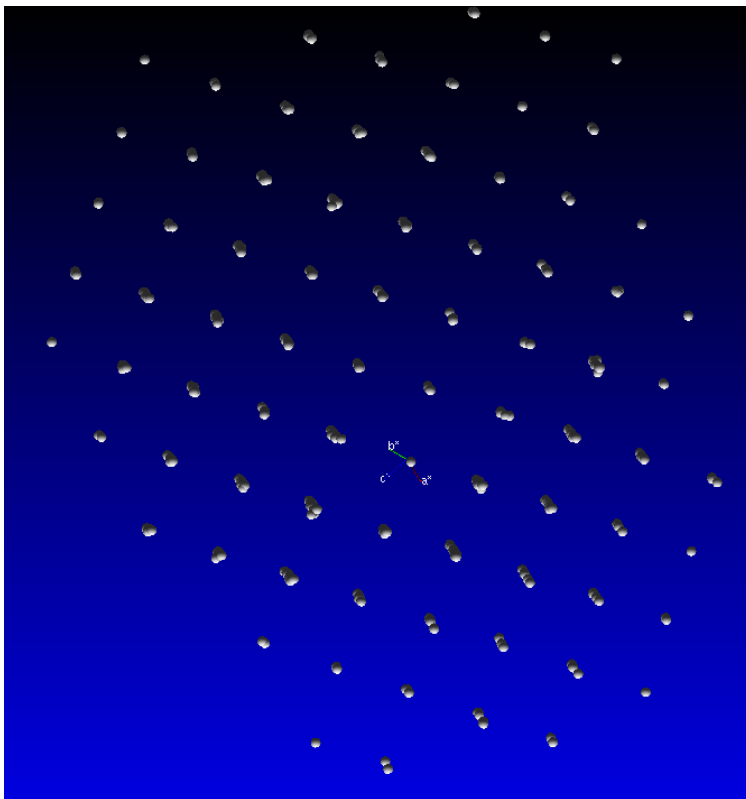
Figure 3.13: Screenshot of the diffraction space of LaNiGa$_2$ from a SCXRD experiment. The software APEX-3 was used to harvest and record the location of each spot. The coordinates of each diffraction spot represents a specific Miller index originating from a set of real world crystal lattice planes.

this method is an extremely powerful tool to comprehensively elucidate most details about a single crystal's unit cell. More can be learned about SCXRD refinement techniques in the following books [204–207].

3.2.3   Energy Dispersive Spectroscopy

What information can be gained?

What differentiates EDS from the X-ray diffraction techniques is that EDS can not help determine any details about symmetry or atom positions. Instead, EDS is a powerful tool

to help determine the elemental composition of a material. Elemental composition can be determined by bombarding the material with a high-energy beam and ejecting inner-shell electrons. Then as an electron from a higher-energy level relaxes into the vacancy, a photon is emitted (typically an X-ray). By counting photons across various energies, it is possible to build an emission spectrum, which could then be used to identify each element within the sample. Typically the high-energy beam is made up of X-rays, but in the instrument at UC Davis, the EDS is attached to a scanning electron microscope (SEM). So the high-energy beam is an electron beam. If the incident electrons have a large enough energy, they can act identically and eject inner-shell electrons from the bombarded atoms.

Not only can this technique be used to qualitatively determine the elements within the material, but it is also possible to quantitatively determine the composition of all the elements. Quantitative analysis can be accomplished by comparing the ratios of peaks within the resulting spectrum. Typical spectra for $CeIn_3$ and $Ce_{0.7}Nd_{0.3}In_3$ are shown in Fig. 3.14. Since Ce and Nd are very close to one another on the periodic table, their respective emission spectra are very similar. Nonetheless, in Fig. 3.14(b) the ratio between the Ce and Nd peaks produced a substitution concentration of $x_{EDS} = 0.342$, which is in good agreement with the nominal value $x_{Nom} = 0.3$.

Since the EDS at UC Davis is attached to an SEM, it is possible to take zoomed-in images of a material's surface and produce elemental maps. Elemental maps were used to show an uniform Ti substitution and O doping across the $CeGe_3$ parent structure in $(Ce_{0.85}Ti_{0.15})Ge_3O_{0.5}$ (Fig. 3.15) [174]. It should be noted that this measurement technique struggles to quantitatively determine the atomic percentage of lighter elements like O. Therefore, after normalization, the average formula unit across all the EDS spectra is calculated to be $(Ce_{0.89}Ti_{0.11})Ge_3O_x$. Overall the EDS work was vital to show that the only way to
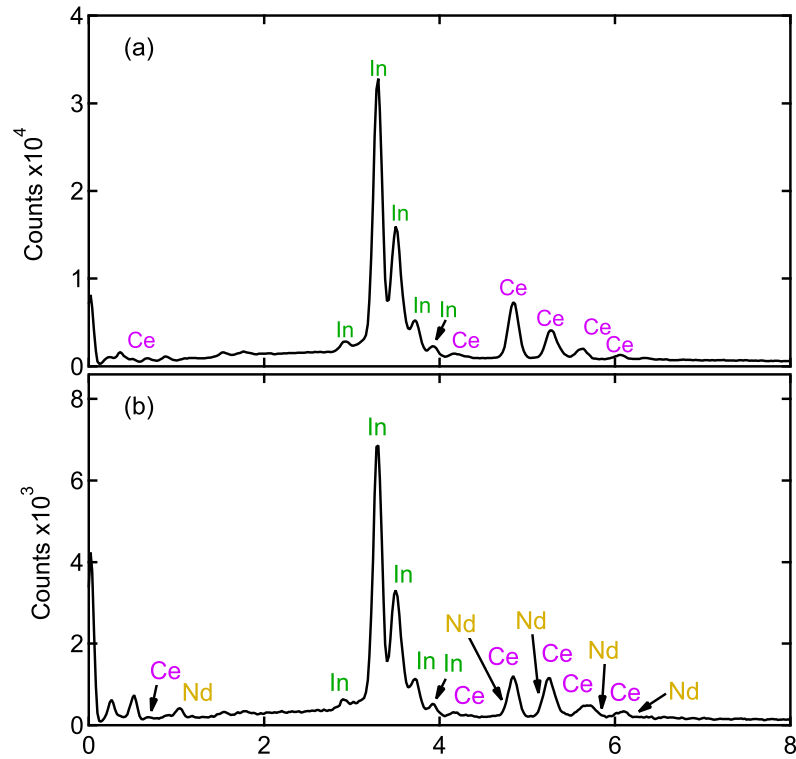
Figure 3.14: EDS spectra for (a) $CeIn_3$ and (b) $Ce_{0.7}Nd_{0.3}In_3$. By comparing the ratio of the Ce and Nd peaks, the measured value of $x_{EDS} = 0.342$ which is very close to the nominal value of $x_{Nom} = 0.3$.

stabilize $CeGe_3$ at ambient pressure was through Ti substitution and O additions.

How to perform the measurements?

To perform these measurements, you simply need to attach the samples onto pieces of carbon tape which are taped on a mountable metal puck. Before running the measurements, you must first know the material's ability to conduct electricity at room temperature. Since the sample is bombarded with a beam of electrons, an electrical charge will build up if the material cannot efficiently conduct electricity (semiconductors or insulators). To avoid
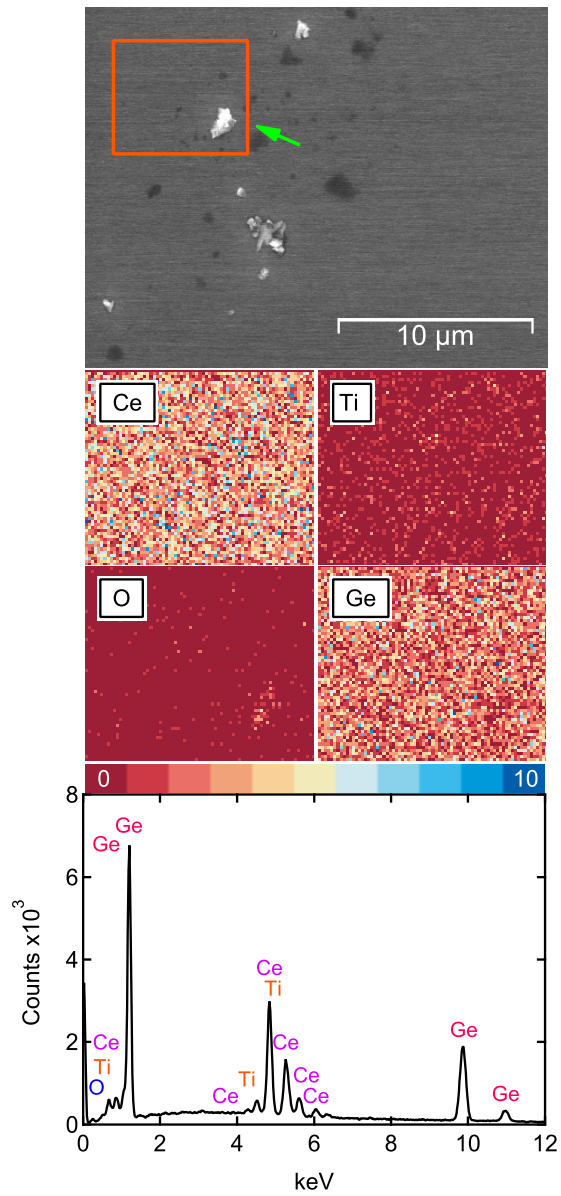
Figure 3.15: SEM image of a bulk crystal with an elemental mapping performed over a selected area, orange rectangle, to determine the uniformity of Ce, Ti, O, and Ge. The arrow shows the pebble (white spot) on the surface of the crystal with a slight excess of O. From the selected area, an EDS spectrum shows the successful identification of each element. Figure was included in the following article [174].

damaging semiconducting or insulating samples, one could build in time breaks to allow the electron build-up to disperse to the surroundings. This issue does not apply to metallic samples as these materials can easily move electrons to quickly dissipate any charge build-up.

What analysis can be done?

As seen in Fig. 3.14 the software produces spectra that can be used to identify the elements within the samples. Additionally, the software also produces quantitative atomic percentages for each element based on the intensity of each element's spectrum. To obtain a formula unit, to determine substitution percentages in $Ce_{1-x}Nd_xIn_3$, you need to normalize the atomic percentages. In $Ce_{1-x}Nd_xIn_3$ this was accomplished by normalizing the atomic percentages to the sum of the Ce and Nd amounts.

3.3 Physical Property Characterization

Throughout the previous chapter, there were scattered references to a variety of physical property characterization techniques. In the Taufour group, besides the structural techniques just presented, we specialize in three main methods: electrical resistivity, magnetic susceptibility, and heat capacity. In this section, I will discuss fundamental concepts about each technique, how to set up a measurement, and some basic analyses that can be performed. Obviously, there are a variety of small details contained in the data for each system. Still, by understanding the basics, you can better understand why specific systems deserve to be studied for their uniqueness.

3.3.1   Electrical Resitivity

Basic Concepts

The basic premise for electrical resistivity (ρ) measurements is that they provide insight into a material's electrical conductivity, where the electrical conductivity and resistivity are inversely proportional. In the most basic sense, electrical resistivity is directly related to the scattering of electrons as they move through the sample. However, the scattering rate (τ^{-1}) within a sample is affected by several different factors such as lattice vibrations, magnetic ordering, band structures, and impurities. Therefore to understand the temperature dependence of electrical resistivity ($\rho(T)$) at the atomic level, it is vital to connect it back to the sources of electron scattering.

One of the key characteristics of a metal is that it can conduct electricity well (low resistance). This low resistance occurs because metals have free electrons ('sea of electrons') that can easily travel throughout the material. From band theory, this low resistance is due to the overlapping of the valence and conduction bands at the Fermi level (Fig. 3.16). Since metals have no energy gap between the occupied (valence) and unoccupied (conduction) bands, it requires very little energy to excite electrons within the conduction band. Meaning that thermal fluctuations can easily excite electrons into the higher energy states, and current can flow through the sample with little resistance. Thereby making the conduction electrons act more like free particles in the solid. This simplified view of band structures can also help predict thermal behavior. As temperature decreases and thermal fluctuations slow down, semiconductors and insulators (materials with an energy gap between valence and conduction bands) are expected to show increased resistivity values because fewer electrons have enough energy to overcome the energy gap. In contrast, metals do not have a band gap, so resistivity is expected to drop as the temperature lowers because electron scattering

74
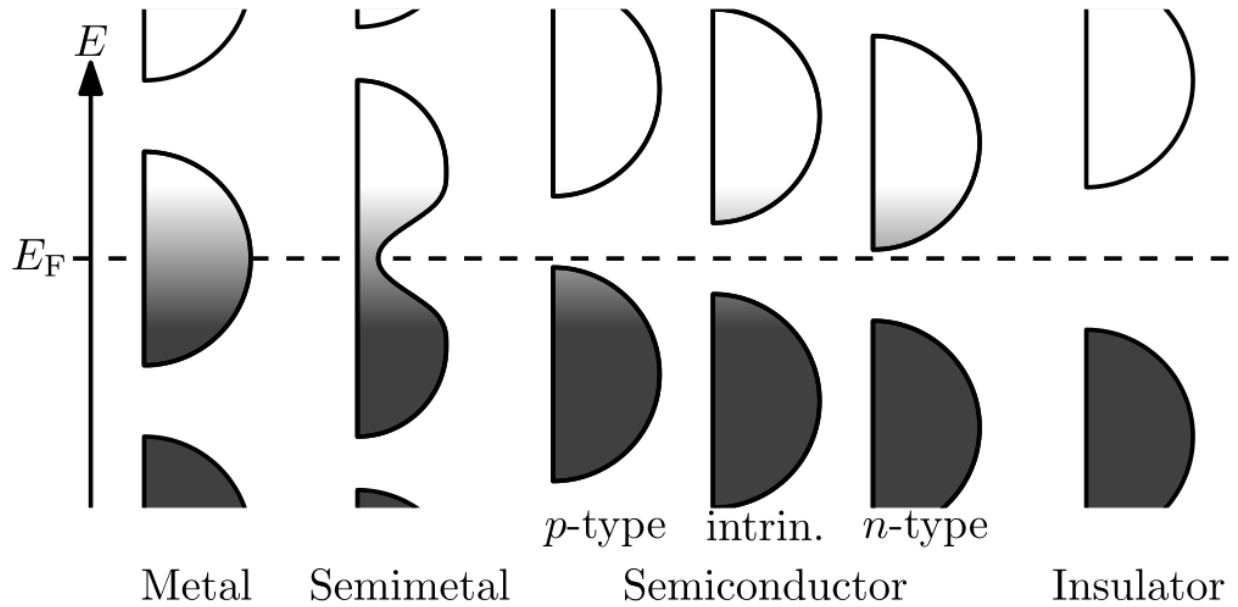
Figure 3.16: Simplified schematics of band structures for metals, semimetals, various semi-conductors and insulators. Image was originally published in [211].

across the variety of sources will reduce (more on this in a bit).

The Drude model builds on this free electron concept to explain the transport properties of electrons in metals. By applying a voltage to a system, the electrons are attracted to the positive end of the electric field. As an electron travels through the sea of electrons, it will undergo collisions with phonons from the lattice, other electrons, and defects within the lattice. The scattering rate of an electron will then define the electrical resistivity by:

$$\rho = \frac{m}{ne^2}\tau^{-1} \tag{3.2}$$

where m is the effective mass of the conduction electrons, n is the density of conduction electrons, $-e$ is the electronic charge, and τ^{-1} is the average scattering rate of electron collisions [5].

According to Matthiessen's rule, τ^{-1} can be thought of as the sum of all scatting processes:

$$\tau^{-1} = \tau_{def}^{-1} + \tau_{e^- - e^-}^{-1} + \tau_{e^- - ph}^{-1} \tag{3.3}$$

where τ_{def}^{-1} is the defect scattering rate, $\tau_{e^- - e^-}^{-1}$ is the electron-electron scattering rate, and $\tau_{e^- - ph}^{-1}$ is the electron-phonon scattering rate. Combining 3.2 and 3.3 gives the total resistivity from these three scattering sources:

$$\rho = \frac{m}{ne^2}(\tau_{def}^{-1} + \tau_{e^- - e^-}^{-1} + \tau_{e^- - ph}^{-1}) = \rho_{def} + \rho_{e^- - e^-} + \rho_{e^- - ph} \tag{3.4}$$

Understanding how each resistivity source can develop as a function of temperature will then determine the thermal dependence of resistivity $\rho(T)$. Defect resistivity, ρ_{def}, is practically temperature independent and simply a function of a sample's innate defects. This aspect is ultimately why the residual resistivity ratio (RRR=$\rho(300\,\text{K})/\rho(0\,\text{K})$) is a great indicator of sample quality. High-quality samples will have few defects, and therefore, ρ_{def} will be small. Thus making RRR values high. On the other hand, $\rho_{e^- - e^-}$ and $\rho_{e^- - ph}$ are proportional to T^2 and T^5, respectively. The Bloch-Grüneisen model can accurately model both effects with the following equation:

$$\rho(T) = A(\frac{T}{\Theta_D})^n \int_0^{\Theta_D/T} \frac{t^n}{(e^t - 1)(1 - e^{-t})} dt \tag{3.5}$$

where A is a material-dependent constant and Θ_D is the Debye temperature [212, 213]. The value n is an integer that is dependent upon the dominant scattering mechanism with $n = 2$ for electron-electron collisions and $n = 5$ for electron-phonon collisions. Overall, these models reveal that the defect and electron-electron scattering only really impact a material's

resistivity at low temperatures (generally $T < 10\,\text{K}$). Above this temperature threshold, the resistivity is dominated by the electron-phonon scatting term. These simple resistivity models for $\rho(T)$ have been shown to accurately predict temperature-dependent resistivity curves for countless nonmagnetic metals [212].

It is worth noting that some transition metals have interband $s-d$ electron-electron scattering that deviates from the T^2 relationship. For these systems, the electron-electron resistivity $(\rho_{s-d}(T))$ term is better modeled by an integer of $n = 3$ for the similar Bloch-Wilson equation:

$$\rho_{s-d}(T) = A(\frac{T}{\Theta_D})^3 \int_{T_E/T}^{\Theta_D/T} \frac{t^3}{(e^t - 1)(1 - e^{-t})} dt \tag{3.6}$$

where T_E is the Einstein temperature [214]. Fig. 3.17 shows the combination of the $s-d$ electron-electron scattering from the Bloch-Wilson equation and the electron-phonon scattering of the Bloch-Grüneisen model to fit the normal state resistivity data for LaNiGa$_2$. The fitting parameters of $\Theta_D = 271\,\text{K}$ and $T_E = 380\,\text{K}$ are within reasonable agreement with the values obtained from the high-temperature heat capacity fittings in Fig. 3.24(b).

Modeling the low-temperature normal state behavior can also provide vital insights about non-Fermi liquid behavior near a quantum critical point [151, 215]. For example, Fermi liquid behavior predicts that low-temperature resistivity curve can be simplified to:

$$\rho(T) = \rho_0 + AT^2 \tag{3.7}$$

Materials that develop non-Fermi liquid behavior have a different power-law relationship than T^2. This fitting was done in Fig. 4.8(c) on LaNiGa$_2$ to show that the low-temperature resistivity data follows Fermi liquid behavior. Therefore tracking the power-law relationship T^n across a non-thermal parameter phase diagram can provide critical insights as a system
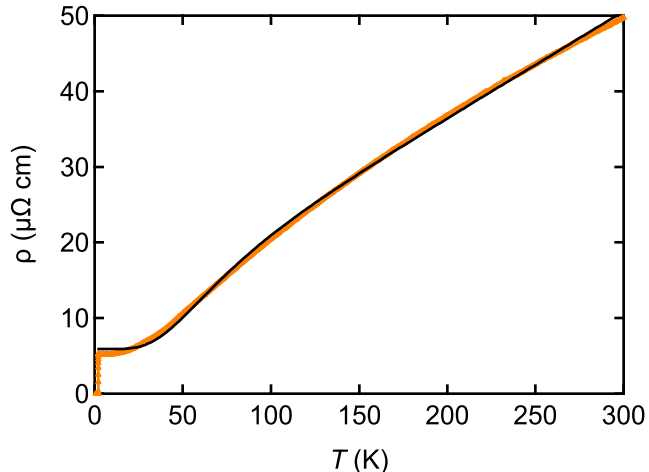
Figure 3.17: Normal state resistivity data of LaNiGa$_2$ which was fit to the $s-d$ electron-electron scattering from the Bloch-Wilson equation and the electron-phonon scattering of the Bloch-Grüneisen model. From the fitting $\Theta_D = 271$ K and $T_E = 380$ K were obtained.

approaches quantum-critical phenomena [151].

The behavior described above is for metals in the normal state without any magnetic ordering. Oftentimes magnetic orderings or magnetic interactions can also impact electron scattering. Such as the Kondo interactions described in section 2.2.2. To isolate $\rho_{mag}(T)$ for any material, the electron-lattice and electron-electron scattering need to be removed from $\rho(T)$. This separation can be achieved by subtracting out $\rho(T)$ from a non-magnetic counterpart with an identical structure. The key assumption is that the non-magnetic analogue has the same electron-lattice and electron-electron scattering as the studied material. For example, the $\rho(T)$ curves from LaIn$_3$ and La$_{0.55}$Nd$_{0.45}$In$_3$ were subtracted out from CeIn$_3$ and Ce$_{0.55}$Nd$_{0.45}$In$_3$ to show the regions where $\rho_{mag}(T) \propto -ln(T)$ (Fig. 5.4(b)).

Electrical resistivity measurements are also a great tool to easily identify transitions. Such experiments were used to identify both the ambient pressure and high-pressure structural transition of β-FeSe [183, 184, 216–218], superconducting transitions in β-FeSe (Fig. 2.1(a)) and LaNiGa2 (Fig. 4.9), AFM ordering transitions in Ce$_{1-x}$Nd$_x$In$_3$ (Fig. 5.4(a)), and FM

78
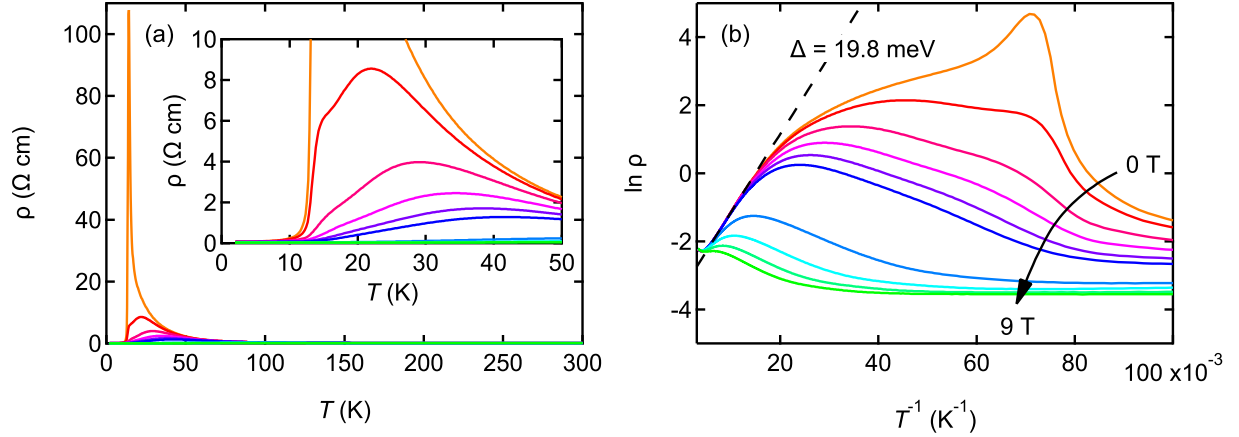
Figure 3.18: (a) Temperature-dependent $\rho(T)$ measurements of $Eu_{11}Zn_4Sn_2As_{12}$ at applied fields of $\mu_0 H = 0$ (orange), $0.2, 0.4, 0.6, 0.8, 1, 3, 5, 7, 9$ T (green). The inset shows the zoomed in data from $2 - 50$ K at different applied magnetic fields. (b) $\ln(\rho)$ vs T^{-1} for the same fields showing the fit to determine the activation energy. Figure was included in the following article [175].

ordering in $Eu_{11}Zn_4Sn_2As_{12}$ (Fig. 3.18). These measurements also provide vital insights on how these transitions can develop with increasing applied magnetic fields. By carefully aligning a $LaNiGa_2$ sample I was able to construct the anisotropic H_{c2} phase diagrams when the applied magnetic field was aligned along the a, b, and c-axes (Fig. 4.11 and Fig. 4.8(b) for the setup). Applying magnetic fields to $Eu_{11}Zn_4Sn_2As_{12}$ allowed us to estimate the FM activation energy and observe colossal magnetoresistance.

From $70 - 170$ K $Eu_{11}Zn_4Sn_2As_{12}$ shows a linear dependence at 0 T in $\ln(\rho)$ vs. T^{-1} (Fig. 3.18(b)). This linear behavior indicates that the resistivity can be can be described by a simple activation energy relation $\rho \propto e^{\Delta/k_B T}$. From the linear region the fitting gives a $\Delta = 19.8$ meV, leading to an estimated band gap of 0.04 eV which was in reasonable agreement with the band calculations [175]. Colossal magnetoresistance, $\frac{|\rho(\mu_0 H) - \rho(0)|}{\rho(\mu_0 H)}$, was observed at $\mu_0 H = 9$ T where a 2690-fold decrease was observed at $T_C = 14$ K (Fig. 3.19(a)).

79
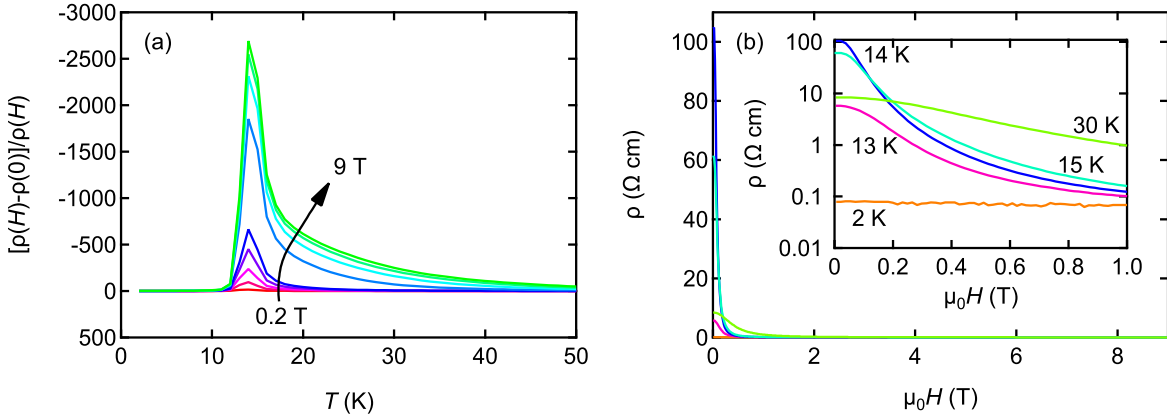
Figure 3.19: (a) Magnetoresistance of $Eu_{11}Zn_4Sn_2As_{12}$ at applied fields of $\mu_0H = 0$ (orange), $0.2, 0.4, 0.6, 0.8, 1, 3, 5, 7, 9\,T$ (green). (b) $\rho(\mu_0H)$ at various temperatures above and below T_C. The inset shows low-field region. Figure was included in the following article [175].

It is also clear that even applying small magnetic fields to $Eu_{11}Zn_4Sn_2As_{12}$ quickly suppresses electrical resistivity. Where ρ decreases by nearly 4 orders of magnitude at 14,K with the application of a $\mu_0H = 1\,T$ field (Fig. 3.19(b)).

Setting Up the Measurement

To perform an electrical resistivity measurement, a current needs to flow through the sample and then the voltage needs to be measured. Then by Ohm's law ($V = IR$) the resistance values from the measurement can be calculated. An electrical resistivity measurement can be accomplished in various ways; but the most straightforward technique is the four-point probe method. For this method, two wires connect the sample to a power source that can supply a current and two voltage wires are attached to the sample inside of the current wires. Examples of the four-point probe technique are shown on single crystals of $LaNiGa_2$ in Fig. 4.8(a) and Fig. 3.20(b) and $Ce_{0.55}Nd_{0.45}In_3$ in Fig. 3.20(c).

Attaching the wires to the samples is a different story. Theoretically, just pressing the

wires onto the surface of the sample should work to perform the measurements. However, practically, this does not work because the wires will move during the measurement and thus break the electrical pathway. Like the overall measurement, there are several different methods to attach the four wires to a sample. Such strategies include indium pressed contacts, wire-bonding, or spot-welding. The most reliable and widely applicable technique is to use silver epoxy to adhere platinum wires to a crystal's surface. Unfortunately, the platinum wires need to be laid by hand, but with practice samples as small at $0.5\,\text{mm}$ wide can be measured using this technique.

The first step to laying contacts with silver epoxy is to practice 'mise en place.' To prepare for laying contacts by hand, the two-part silver epoxy (EPO-TEK H20E) needs to mixed with equal parts by weight, the platinum wires ($\varnothing\,25\,\mu\text{m}$) need to be annealed and cut, and the sample needs to have a clean surface where the wires will be placed. Before placing the wires, the crystal should be placed onto a microscope slide to avoid altering the contacts when it is transferred into an oven to cure the epoxy. Next, with the crystal and everything in place, the wires are dipped into the silver epoxy and then the wire and epoxy are carefully placed onto the crystal's surface. The sample can then be placed into an oven after placing all four wires. Ideally, the curing process should be completed in an oxygen-free environment to prevent any possible sample oxidation. So the sample should be placed in a vacuum oven and heated up to $120\,^{\circ}\text{C}$ for $30\,\text{minutes}$.

Once the epoxy is cured, the crystal then needs to be attached onto a measurement puck. A DC resistivity puck should be used if the sample is expected to have semiconductor or insulating behavior. But if the sample is expected to be metallic, then an AC transport puck (which uses an AC current supply) is better suited to handle the low resistance values. With the puck in hand, the wires should then be soldered onto their respective pads (voltage and

81

current) on the puck. After the wires have been soldered onto the puck, a small amount of DC current ($\sim 1 - 10\,\mathrm{mA}$) should be run through each contact to anneal away any defects from the epoxy or the soldered joints. If you intend to perform low-temperature measurements (down to $0.35\,\mathrm{K}$) with the $^3\mathrm{He}$ probe, then the sample needs to be in good thermal contact with the puck. Thermal contact can be achieved by applying a small amount of Apiezon N grease on the puck's surface and then carefully pressing the crystal into the grease.

Analyzing the Data

Once a sequence has been completed and the entire dataset collected, we can analyze the data. The most important thing to note about the outputted data is that it only reports the resistance values of each measurement. So calculating resistivity values can be achieved with the following equation:

$$\rho = \frac{RA}{L} \tag{3.8}$$

where R is the resistance value, A is the cross sectional area of the sample, and L is the distance between the two voltage wires (Fig. 3.20). Therefore, performing these calculations requires that the A and L values be measured for each sample and measurement. Measuring these values can be achieved by taking pictures of the cross-sectional area of the sample before laying contacts and the voltage lead distance after curing the epoxy. By having millimeter paper in both pictures then both geometric values can easily be measured with software.

Since both A and L are required to obtain resistivity values, this influences which samples should be selected to run these measurements. The ideal sample shape is a rectangular prism because this shape minimizes any errors associated with the measured A and L values, thereby reducing the error of the calculated ρ values.
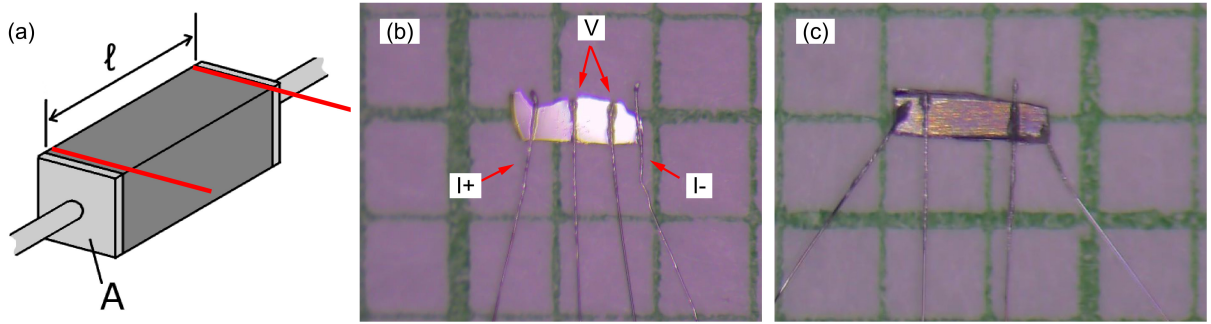
Figure 3.20: (a) Ideal sample shape for an electrical resistivity measurement. A and L are shown in this figure and these values constant throughout the rectangle prism. Image was originally published in [219]. Contacts laid and annealed on single crystals of (b) LaNiGa$_2$ and (c) acid-etched Ce$_{0.55}$Nd$_{0.45}$In$_3$. Both crystals are on millimeter paper so the resistivity geometry of the measurement can be measured.

3.3.2 Magnetic Susceptibility

How the Measurement Works and Setting up the Measurement

To understand a material's magnetic behavior at a particular state, it is best to first understand what we are trying to measure and then some basic mechanisms behind the measurement. Understanding basic concepts will then inform how to set up a magnetic susceptibility measurement to make conclusions about material's magnetic behavior and ordering. Since magnetism units are quite confusing, I will use SI units unless specified.

A magnetic material is first defined as a solid consisting of many individual magnetic moments. Understanding the macroscopic magnetic behavior of the material can then inform us about how these magnetic moments microscopically interact with one another, if at all. A material's magnetization, M, is defined as the magnetic moment per unit volume (J T^{-1} m^{-3}). The net magnetic flux density, B, of a system is related to a material's magnetization by:

$$B = \mu_0(H + M) \tag{3.9}$$

where H is the applied external magnetic field. H is the field applied by the superconducting magnet from the Magnetic Property Measurement System (MPMS) in real magnetic measurements. Setting H to a particular value and measuring B with the superconducting detection coil can isolate M at a particular applied field and temperature. Measuring B is achieved by moving the material through the sample space to induce a current in the detection coils. By measuring the amount of induced current, we can then relate this directly to B of the measurement and, ultimately, the magnetic moment of the sample.

Understanding how the MPMS measures magnetic moments can inform us how to set up a magnetic susceptibility measurement. Since the MPMS moves the sample through the detection coils, any difference in magnetic flux over the scanning range (typically 6 cm) will induce a current in the detection coils. Therefore the sample holder must have a uniform magnetic moment throughout the scanning range. This necessity is most easily achieved by using simple plastic straws (see Fig. 3.21(a)). These naturally have a small magnetic moment, can easily be manipulated to hold a small crystal, and provide a long scanning range. For the setup, it is essential to ensure that the 6 cm scanning range around the single crystal is free of any other material with a magnetic moment, intended or unintended.

When performing a measurement, the MPMS reports values of the magnetic moment (m) in CGS units - electromagnetic units (e.m.u)$= 10^{-3} \, \text{J} \, \text{T}^{-3}$ - after each scan. Across different systems we may use m to report a material's magnetism in a variety of other CGS units such as magnetization per volume (e.m.u./cm^3), magnetization per mass (e.m.u./g), or magnetization per mol (e.m.u./mol). The unit chosen is dependent upon the quality of the measured sample and the accuracy of volume. In certain circumstances, it could be beneficial to report the magnetism per a formula unit (μ_B/f.u.) or a particular atom (μ_B/Ce atom) to better compare to other materials. It is also widespread to display the magnetism

as magnetic susceptibility $\chi = M/H$. Since M and H contain the same units, χ is actually unitless. Confusingly, e.m.u. is actually used to display χ per volume (e.m.u./cm^3), per mass (e.m.u./g), or per mol (e.m.u./mol). Especially for superconductors, it is beneficially to display the magnetic susceptibility in SI units. This can be achieved by multiplying the CGS magnetic susceptibility (volumetric) by 4π to produce SI magnetic susceptibility. Using χ, in either CGS or SI units, allows us to easily compare the magnetic behavior to theoretical models such as Curie-Weiss Paramagnetism.

Paramagnetism

As mentioned in section 2.2.1, before entering a magnetically ordered state, most $4f$ systems are in the magnetically disordered paramagnetic state. There are several origins of paramagnetism (e.g. Pauli and Van Vleck), but the most common model for $4f$ systems is the Curie-Weiss paramagnetism. In this paramagnetic state, the magnetic moments are randomly oriented by thermal fluctuations and interact internally. 2.2 shows the equation that defines the magnetic susceptibility temperature dependence for a Curie-Weiss paramagnet. Taking χ^{-1} and fitting it to the Curie-Weiss susceptibility $1/\chi(T) = (T - \Theta_{CW})/C$ allows us to compare the experimental data to this model more easily (see Fig. 3.21).

From fitting χ^{-1} two values can be extracted: the effective moment μ_{eff} of the paramagnet and Θ_{CW} which gives the type of interactions between the moments. The slope for molar χ^{-1} in CGS units is equal to $1/C$ and C can be used to calculate the effective moment:

$$\mu_{eff} = \sqrt{\frac{30 k_B C}{\mu_B^2 N_A}} \tag{3.10}$$

where k_B is Boltzmann's constant, μ_B is Bohr N_A is Avogadro's number. Typically μ_{eff} is reported in units of Bohr magnetons (μ_B). By determining the experimental effective
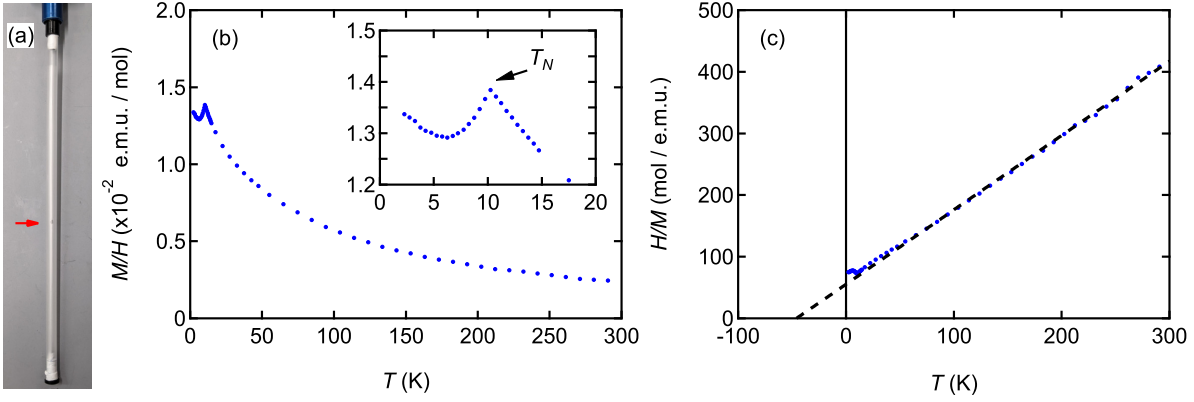
Figure 3.21: (a) Straw setup for a magnetic susceptibility measurement. The red arrow shows the sample. (b) Shows the χ paramagnetic curve of CeIn$_3$ until the onset of the AFM state. The inset better shows the sharp downturn associated with the AFM ordering. The temperature at the peak is T_N. (c) χ^{-1} data for CeIn$_3$ from (b). The dotted black line shows the Curie-Weiss χ^{-1} fitting of the paramagnetic region. Values of $\mu_{eff} = 2.58\mu_B$ and $\Theta_{CW} = -45.9$ K were obtained from the fitting.

moment from the χ^{-1} fitting, it is then possible to compare this value to the calculated effective moments. For CeIn$_3$, this calculation resulted in a value of $\mu_{eff} = 2.57\mu_B$. This experimental value matches well with that of the calculated value, $\mu_{eff} = 2.6\mu_B$, for a Ce^{3+} free-ion [84].

The other insight that can be obtained from plotting $\chi(T)^{-1}$ are the types of interactions between the magnetic moments. If $\Theta_{CW} > 0$ then there are net FM interactions. On the flip side, if $\Theta_{CW} < 0$, then there are net AFM interactions. If Θ_{CW} happens to equal zero, then there are no dominant interactions between the magnetic moments, and the material is said to be a Curie paramagnet. Plotting $\chi(T)^{-1}$ and examining the sign of the x-axis intercept indicates the types of interactions: positive indicates FM and negative indicates AFM. It is important to distinguish these types of paramagnetic interactions from a magnetically ordered state.

Antiferromagnetism

When a system enters, the AFM ordered state the magnetic moments align in the opposite direction to their neighbors. As discussed in section 2.2.1 this magnetically ordered state can take on many different iterations. Regardless of how the magnetic moments align in any particular system, the experimental signatures of the AFM state should be similar. Wherein the paramagnetic curve shows a sharp drop at T_N with the onset of the AFM state. This behavior can best be seen in the inset of Fig. 3.21(b) for $CeIn_3$.

Frequently it is good to think about the AFM state as the combination of two antiparallel FM sublattices (M_+ and M_-). By thinking about an AFM material in such a manner, we can understand the consequences of anisotropic experiments. For example, if a small external magnetic field aligns parallel to one of the sublattices, M_+, it must therefore align antiparallel to the other sublattice, M_-. At which point, if we assume that the external magnetic field is too small to flip M_- to align parallel with H, when all thermal fluctuations are removed, the net magnetization of this AFM state should be zero: $\chi_\parallel = 0$. This result is because at $T = 0\,K$, both sublattices M_+ and M_- are fully and equally saturated. However, if H is aligned perpendicular to one or both sublattices, then the net magnetization should no longer equal zero: $\chi_\perp \neq 0$. This difference is because the external magnetic field will slightly tilt the magnetic moments within the sublattices towards the applied magnetic field. In both cases, the resulting $\chi(T)$ curves are shown in Fig. 3.22.

If we assume an AFM state to be completely antiparallel at $T = 0\,K$ such that the $M = 0$ with no applied field, let us understand what happens as a magnetic field is first applied and then increases. When the applied magnetic field is aligned with M_+ and small, the sublattices should remain antiparallel. Then, at a particular magnetic field strength, the M_- lattice should rapidly flip to start to align parallel with H. If the M_- moments
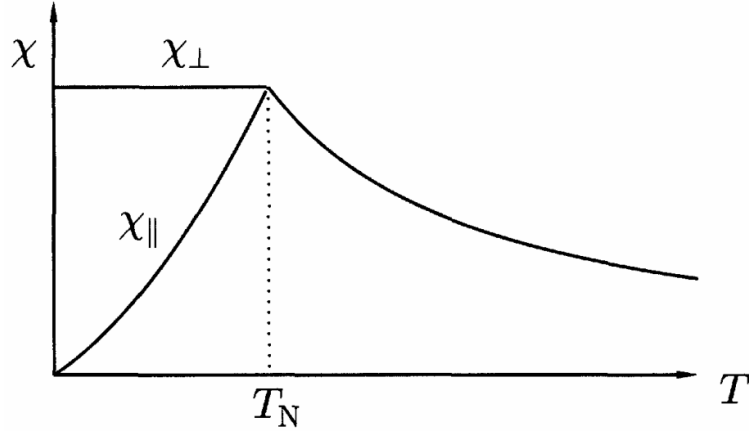
Figure 3.22: The $\chi(T)$ curves if the applied magnetic field is aligned along the same direction of the M_+, $\chi_\parallel$ or perpendicular to one of the sublattices, $\chi_\perp$. Figure was originally published in [84]

completely align with H then the AFM state undergoes a spin-flip, and the state transitions to a saturated FM state. If the M_- moments become canted and are not perfectly aligned with the applied magnetic, the AFM state has undergone a spin-flop. After a spin-flop, if the applied magnetic field continues to increase, the magnetization should also increase until the system becomes completely saturated with all the moments from both sublattices aligned. However, if the applied magnetic field is not perfectly aligned with either sublattice or perpendicular to either sublattice, then the magnetization should gradually increase as the applied magnetic field increases. That is until the moments are entirely aligned.

Superconductivity

Although not a magnetically ordered state, magnetic susceptibility is one of the critical tools for characterizing superconductors. As shown in Fig. 2.1(b) in section 2.1.1 a diamagnetic response is exhibited when a material enters the superconducting state. Since applied magnetic fields suppress superconductivity (see Fig. 4.11), it is imperative to perform magnetic

susceptibility measurements with the smallest possible field (typically $20\,\mathrm{Oe}$). This ensures the highest T_{sc}.

As can be seen in Fig. 2.1(b), there is a large difference in the magnitude of the diamagnetic response between zero-field cooled (ZFC) and field-cooled (FC). For an ideal and type-I superconductor, this should not be the case. But in a type-II superconductor, this difference is attributed to vortices. For ZFC measurements, cooled below T_{sc} without an applied magnetic field, when the magnetic field is turned on, the superconductor will shield the external magnetic field and produce a diamagnetic response. If same material is cooled below T_{sc} with a small magnetic field, FC, then below T_{sc} the superconductor will first enter the Abrikosov state (vortex state). Here some of the magnetic field will penetrate the superconductor through a vortex and produce a smaller diamagnetic response than the ZFC one. Even as the system continues to cool down into the Meissner regime (below the $H_{\mathrm{c1}}(T)$ curve), the penetrative magnetic field can remain trapped. Therefore the weakened diamagnetic response of the FC curve remains.

Another interesting aspect of performing magnetic susceptibility measurements on superconductors is that the magnitude of the diamagnetic response can provide insights into the sample quality. An ideal superconductor should exhibit perfect diamagnetism wherein the entire volume of the sample screens the magnetic field. It should then follow that the magnetic response should equal the strength of the magnetic field. By displaying volumetric susceptibility in SI units, we should see that $\chi_{SI} = -1$ for an ideal superconductor. Therefore plotting the volumetric magnetic susceptibility curves for a superconductor in SI units provides insights into how close a sample gets to perfect diamagnetism. As can be observed in Fig. 4.7 a near-perfect diamagnetic response is observed for this particular sample of LaNiGa$_2$. Although plotting the volumetric susceptibility in SI units is helpful

to understand the shielding fraction of a superconducting sample, keep in mind that this measurement only indicates what percentage of the surface is superconducting. Measuring the magnetic susceptibility of a superconductor does not provide insights into the bulk of the sample. Thus magnetic susceptibility needs to be coupled with electrical resistivity and heat capacity measurements to understand the superconducting state better. It should be noted that it is possible to get a diamagnetic response less than $\chi = -1$. This response results from demagnetization fields due to a sample's shape.

Running field-dependent magnetic susceptibility measurements can also be vital to understanding whether a superconductor is type-I or type-II. Type-I superconductors do not have a vortex state. So the magnetic response should have a -1 slope as H increases. That is until the critical field, H_c, at which point the superconducting state is destroyed, and the material enters the normal state. For a type-II superconductor, the magnetic response will also initially have a -1 slope. However, in a type-II superconductor, there are two critical fields: the lower critical field H_{c1} and the upper critical field H_{c2}. Once the applied magnetic field reaches H_{c1} then the superconductor will enter the vortex state. At which point, the magnetic response will no longer follow the -1 slope and start to increase back to zero. While in the vortex state, the superconductor will continue to have a diamagnetic response until H_{c2} is reached, and the superconducting state is destroyed. These magnetic responses for both types of superconductors can be observed in Fig. 3.23.

It should also be noted that while determining whether a superconductor is type-I or type-II is important, this determination does not indicate whether the superconductor is conventional or unconventional. While nearly all conventional superconductors are type-I, some type-II superconductors are well described by conventional theory like Nb, Nb-Ti, V_3Si, and MgB_2 (both V_3Si and MgB_2 show multiband behavior, but both have conven-
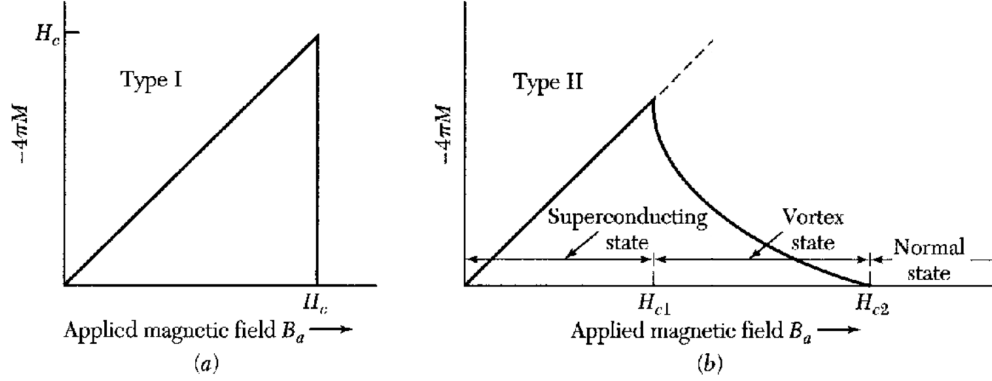
Figure 3.23: Magnetization versus applied magnetic field for a (a) type-I and a (b) type-II superconductor. Both superconductors display perfect diamagnetism with a slope of -1 until H_c is reached for a type-I or H_{c1} is reached for a type-II. At which point the superconducting state is destroyed for a type-I. While the type-II enters the vortex state. Not that minus $4\pi M$ is plotted as the vertical axis. Figure was originally published in [6]

tional phonon-mediated Cooper pairs). Conversely, most unconventional superconductors are type-II. Therefore, magnetic susceptibility measurements are best to identify whether the superconductor is type-I or type-II and not necessarily whether it abides by conventional BCS theory.

3.3.3 Heat Capacity

Mechanisms Behind the Measurement

Heat capacity measurements are a fantastic tool to obtain information on the lattice, electronic, and magnetic properties of a solid. Temperature-dependent heat capacity measurements on metals are well described by theory. Comparing the experimental data to these models is critical to a comprehensive understanding of a condensed matter system. Performing these thermodynamic measurements also provides insight into the bulk of the sample (e.g. order of a transition). The nature of heat capacity measurements is ultimately due to how these experiments are performed.

91

There are several different measurements techniques, such as the classic coffee cup calorimeter used in general chemistry and physics labs. In the PPMS, the heat capacity option uses the relaxation technique. For this technique, the sample, grease, and the platform undergo a short burst of heat from small built-in heaters and then all materials are allowed to cool. The thermal relaxation of the system is then modeled, and a heat capacity value (amount of energy it takes to warm one degree: J/K) can be obtained. By previously measuring the heat capacity response for the sample holder and the grease (called an addenda), the background's response can be subtracted out to isolate the sample's heat capacity. This mechanism also indicates that the heat capacity of the entire sample on the platform will be measured. Knowing this and how long it takes to perform a complete heat capacity experiment, the measurement should be performed on a well-known and phase pure sample.

For successful measurements, there are several vital aspects. One of which is thermal isolation. Small metal wires are attached to the bottom of the platform. These wires then provide an electrical pathway between the heaters, platform thermometer, and sample puck. These wires, as intended, also act as thermal links to the surrounding bath. After a small burst of heating, the excess heat from the sample and platform dissipates through the wires during the thermal relaxation period. Therefore, to obtain the highest quality data, it is imperative to minimize the heat that is lost to the surrounding environment. Reducing heat loss can be obtained by performing the measurements in a high-vacuum state (10^{-5} Torr).

Another important aspect of heat capacity measurements is ensuring good thermal contact between the sample and the platform. If there is not a sufficient thermal pathway for the heat, the sample will not be thoroughly heated, and poor data will ensue. This dilemma can easily be averted by applying a thin layer of grease to the platform and carefully pressing the sample into the grease.

Setting up the Measurement

The first step to perform a successful heat capacity measurement is to run an addenda. This initial run collects the heat capacity data for the platform and the grease so that the data can be subtracted out from the final run with the sample. Before applying the grease it is crucial to know the temperature range of the final measurement because this will determine which grease to use. If performing a high-temperature scan ($T > 200\,\text{K}$) then it is recommended to use Apiezon H grease, and for a low-temperature measurement ($T < 220\,\text{K}$) then it is recommended to use Apiezon N grease. This recommendation is because below $200\,\text{K}$ H grease tends to spontaneously pop off, and above $220\,\text{K}$ N grease melts and heat capacity measurements in this temperature range are unreliable. After selecting the appropriate grease, it must then be applied to the sample platform. To collect the best data on your sample, it is essential to use just enough grease to ensure that the sample is in good thermal contact with the platform. If too much grease is applied, the addenda's heat capacity data could mask small changes in the sample's heat capacity data.

After completing the addenda then the sample must be carefully placed onto the platform. A special mounting contraption is required to load the sample onto the platform (and apply the grease). Since the four metal wires (see Fig. 3.24(a)) are very delicate, you can not simply place the sample onto the platform by hand. Instead, by mounting the heat capacity puck onto the mounting contraption, the platform can rest onto a flat mounting post that can provide support for placing the sample (and applying grease). This mounting contraption also has a small vacuum that ensures the platform sits completely flat on the mounting post. Once the sample has been thoroughly yet carefully pressed into the grease, the measurement is ready to run. The complete setup of the sample and grease can be seen in Fig. 3.24(a).
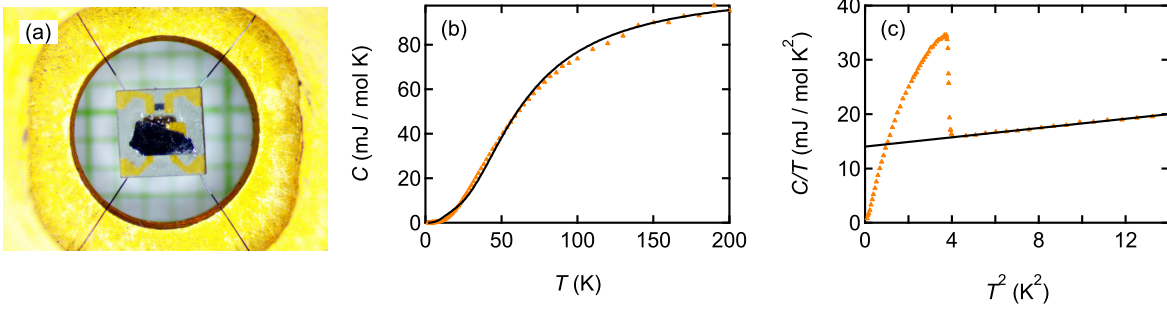
Figure 3.24: (a) Sample mounted onto the platform with a small amount of grease. The four metal wires send electricity to the platform heater and thermometer. These wires also provide a thermal pathway for the heat to dissipate into the thermal bath. (b) Zero-field high-temperature data of LaNiGa$_2$. The data fits well to the high-temperature weighted Einstein-Debye model (black line) defined by 3.11. (c) Zero-field low-temperature data of LaNiGa$_2$. In addition to the second-order superconducting transition (sharp jump) the normal-state data fits well to the low-temperature Debye model (black line) defined by 3.13.

High-Temperature Information

As just mentioned, temperature-dependent heat capacity measurements of metals are well defined by theoretical models. I will first discuss the high-temperature models, and then subsequently, I will talk about the low-temperature model. Previously highlighted was that heat capacity data can provide insights into a solid's lattice, magnetic, and electronic properties. In high temperatures, like in electrical resistivity, the heat capacity is dominated by phonons. In fact, at sufficiently high enough temperatures, the heat capacity is entirely dominated by phonons, and the Dulong-Petit value of $3nR$ (n is the number of atoms in a formula unit) is a good approximation for the heat capacity. As the sample is cooled down and phonon branches begin to depopulate, the heat-capacity data can be defined by the

94

weighted Einstein-Debye model [220]:

$$C(T) = \gamma_n T + nx C_{\text{Debye}}\left(\frac{T}{\Theta_D}\right) + n(1-x) C_{\text{Einstein}}\left(\frac{T}{T_E}\right) \tag{3.11a}$$

$$C_{\text{Debye}}\left(\frac{T}{\Theta_D}\right) = 9R\left(\frac{T}{\Theta_D}\right)^3 \int_0^{\frac{\Theta_D}{T}} \frac{x^4 e^x}{(e^x - 1)^2}dx \tag{3.11b}$$

$$C_{\text{Einstein}}\left(\frac{T}{T_E}\right) = 3R\frac{z^2 e^z}{(e^z - 1)^2}, z = \frac{T_E}{T} \tag{3.11c}$$

where n is the same as above, $R = N_A k_B$ is the gas constant, and x is the fractional contribution of the Debye model. At first, the Einstein model was a method for estimating the phonon contribution in a solid by assuming that the lattice vibrations were a collection of many non-interaction harmonic oscillators. Each of which was oscillating at the same frequency. While this first model was primarily successful in describing the shape of the heat capacity curve, it struggled to predict low-temperature behavior accurately. Debye improved upon this initial model by allowing the phonon frequency to vary. This model improved the low-temperature behavior (see next section) but can sometimes struggle to accurately define the intermediate temperature regions. Later it was discovered that a weighted sum of the two models more accurately predicts the heat capacity data over a wide temperature window. Within the weighted sum, the Einstein model approximates the optical phonons [6] and the Debye model approximates the acoustic phonons.

Therefore, to best model the heat capacity data over a wide temperature range, the first step is to calculate the number of optical branches. It then follows that the percentage of the acoustic phonons will be equal to x in 3.11. To calculate the number of each phonon branches, one must first determine the number of atoms, N_p, within the primitive unit cell. With N_p, there are $3N_p$ total phonon branches with 3 acoustic and $3N_p - 3$ optical branches.

For LaNiGa$_2$ this was achieved and plotted in Fig. 3.24(b). With 8 atoms in the primitive

cell, there are 24 phonon branches. The effective Debye model contribution should then be $x = 12.5\%$. The black line in Fig. 3.24(b) shows the fitting of the function, which gives a Debye temperature, $\Theta_D = 83\,\mathrm{K}$, and an Einstein temperature $T_E = 200\,\mathrm{K}$.

Low-Temperature Information

While a weighted sum of two models best defines the high-temperature heat capacity data, low-temperature heat capacity can be well described by just the Debye model because at these temperatures, only acoustic modes are thermally excited [6]. Therefore, at these temperatures the Debye model can be simplified to show that $C \propto T^3$:

$$C = \frac{12\pi^4}{5} N_A k_B \left(\frac{T}{\Theta_D}\right)^3 \tag{3.12}$$

In addition to acoustic phonons contributing to the heat capacity at low temperatures, electronic behavior can also influence the heat capacity. Thus, the combination of the Debye model simplification and the electronic heat capacity can be combined to show the experimental linear relationship between C/T and T^2:

$$\frac{C}{T} = \gamma_n + \beta\,T^2 \tag{3.13}$$

where γ_n is the Sommerfeld coefficient and $\gamma_n T$ corresponds to the electronic heat capacity. The parameter β then contains the Debye temperature:

$$\Theta_D = \sqrt[3]{\frac{12\pi^4 N_A k_B}{5\beta}} \tag{3.14}$$

Since only the acoustic phonons are thermally populated at these temperatures, the Debye

temperature from this experimental fit is often considered more accurate than the high-temperature fitting. As with the high-temperature region, the normal state low-temperature data for LaNiGa$_2$ was fit to 3.13 and shown in Fig. 3.24(c). Values of $\gamma_n = 14.1 \, \mathrm{mJ/mol \, K^2}$ and $\Theta_D = 166 \, \mathrm{K}$ were obtained from this fitting.

Since the Sommerfeld coefficient represents the residual electronic heat capacity, this can provide us a nice insight into the 'weight' of the conduction electrons. Where $\gamma_n \propto m$. Therefore low-temperature heat capacity measurements are a great way to determine whether a system qualifies as a heavy fermion material (i.e. materials with 'heavy' electrons). For heavy fermion materials, the Sommerfeld coefficients are typically two or three orders of magnitude larger than for usual metals. Examples of this are CeIn$_3$ and UTe$_2$ which have normal-state γ_n values of 130 and 110 $\mathrm{mJ/mol \, K^2}$, respectively [53, 112]. Therefore it is clear that LaNiGa$_2$ is not a heavy fermion material, which is expected for La-based materials with no $4f$ electrons.

Superconductivity

As mentioned a couple of times, heat capacity measurements are critical to identifying and understanding a superconducting state. Not only does the onset of the superconducting state coincide with a second-order phase transition (Fig. 3.24(c)), but heat capacity measurements can also indicate sample quality. Since the entire mass on the platform is measured, it is possible to observe impurities or if the sample does not exhibit bulk superconductivity. In such cases, the heat capacity of the superconducting state would not approach zero because the entirety of the sample is not superconducting. However, there are cases where the heat capacity of pure superconducting samples does not approach zero [53].

Heat capacity measurements are also beneficial for determining the nature of an uncon-
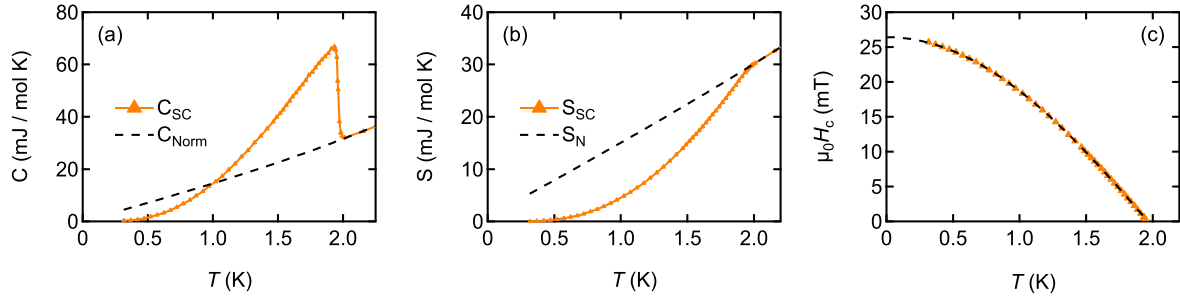
Figure 3.25: (a) Heat capacity data from the superconducting state of LaNiGa$_2$ and the extrapolated low-temperature Debye fitting representing the normal state heat capacity. (b) the entropy data calculated from the superconducting and normal states in (a). (c) The $H_c(T)$ curve calculated from 3.15 and the Taylor expansion fitting from 3.18. From the fitting $H_c(0) = 23$ mT was obtained.

ventional superconductor, as discussed in section 2.1.1. From heat capacity measurements, it is possible to deduce the presence of any superconducting gap nodes and the form of the gap nodes. It is also possible to elucidate how many energy gaps are present within the superconducting state [12, 13]. As can be seen for LaNiGa$_2$ Fig. 4.10(b), the superconducting heat capacity data reveal evidence for two superconducting energy gaps.

In addition to elucidating information about the unconventional nature of the superconducting state, it is also possible to understand the development of the thermodynamic critical field $H_c(T)$ [5, 221]. The following equations achieve this:

$$-\frac{1}{2}\mu_0 V_m H_c^2(T) = \Delta F(T) = \Delta U(T) - T\Delta(T) \tag{3.15}$$

where μ_0 is the permeability of free space and V_m is the molar volume. The difference in internal energy, $\Delta U(T)$, can be obtained by integrating the difference of the heat capacity

98

between the superconducting $C_s(T)$ and the normal state $C_n(T)$:

$$\Delta U(T) = \int_{T=0}^{T} [C_s(T') - C_n(T)]dT' \tag{3.16}$$

and the difference in entropy, $\Delta S(T)$, can be obtained by taking the difference of entropies between the superconducting and normal states. The entropy for each state can be obtained by integrating $C(T)/T$ for each state:

$$\Delta S(T) = \int_{T=0}^{T} \frac{C_s(T') - C_n(T)}{T'} dT' \tag{3.17}$$

When combined together $H_c(T)$ can be fit to a Taylor expansion to determine $H_c(0)$:

$$H_c(T) = H_c(0)[1 - b(T/T_{sc})^2 + (1 - b)(T/T_{sc})^4] \tag{3.18}$$

where b is a fitting parameter [222]. It should be noted that this critical field H_c is purely a thermodynamic value and different than either H_{c1} or H_{c2} for a type-II superconductor.

Chapter 4

Discovery of Dirac Lines and Loop in Time-Reversal Symmetry Breaking Superconductor LaNiGa$_2$

This work was performed in collaboration with Yundi Quan, Matthew Staab, Shuntaro Sumita, Antonio Rossi, Kasey Devlin, Kelly Neubauer, Daniel Shulman, James Fettinger, Peter Klavins, Susan Kauzlarich, Dai Aoki, Inna Vishik, Warren Pickett, and Valentin Taufour. The manuscript is currently under review for publication but has been posted on the pre-publishing database arXiv [223]. All band structure calculations were completed by Yundi Quan and Warren Pickett. The ARPES work was performed by Matthew Staab, Daniel Shulman, and Inna Vishik. Both band structure calculations and the ARPES work are included in this chapter to have a comprehensive and complete story about LaNiGa$_2$. The gap structure and nonsymmorphic symmetry analysis performed by Valentin is omitted from this chapter. Copyright permission has been obtained and granted to use figures 4.1

and 4.2.

4.1   Background on μSR for spin-triplet Cooper pair Identification

When a spin polarized positive muon (spin $\frac{1}{2}$) becomes impregnated within a sample, the muon spin precesses with an angular frequency (ω_μ) proportional to the magnetic field $\omega_\mu = \gamma_\mu B$, where γ_μ is the gyromagnetic ratio for the muon [224]. After a muon decays with a mean lifetime of $\tau = 2.2\,\mu$s, a positron is then emitted. The length of the muon's lifetime and precession frequency will then determine the direction that the positron is emitted (see Fig. 4.1(a) for a schematic). In the end the internal magnetic behavior of a sample can be elucidated by counting the positron emission as a function of direction and time. More specifically, by performing the measurement with zero external magnetic field (ZF-μSR), this then provides experimentalists a great tool to probe subtle changes (like an additional magnetic source) in a sample's magnetic behavior. The nature of this technique, along with Polar Kerr effect measurements, then makes it one of the most powerful tools to investigate for spin-triplet Cooper pairs within a superconducting state [4].

An additional small internal magnetic moment should coincide with the onset of spin-triplet Cooper pairing. Therefore, in this scenario ZF-μSR measurements should show the muon spins precessing with a higher frequency. However, in polycrystalline samples, with a random static Gaussian distribution of fields, each muon will be exposed a different internal magnetic field magnitude. Therefore, instead of producing a typical oscillatory curve, the normalized decay positron asymmetry function (G(t)) will yield a Kubo-Toyabe type function, where the relaxation rate is directly proportional to the magnitude of internal
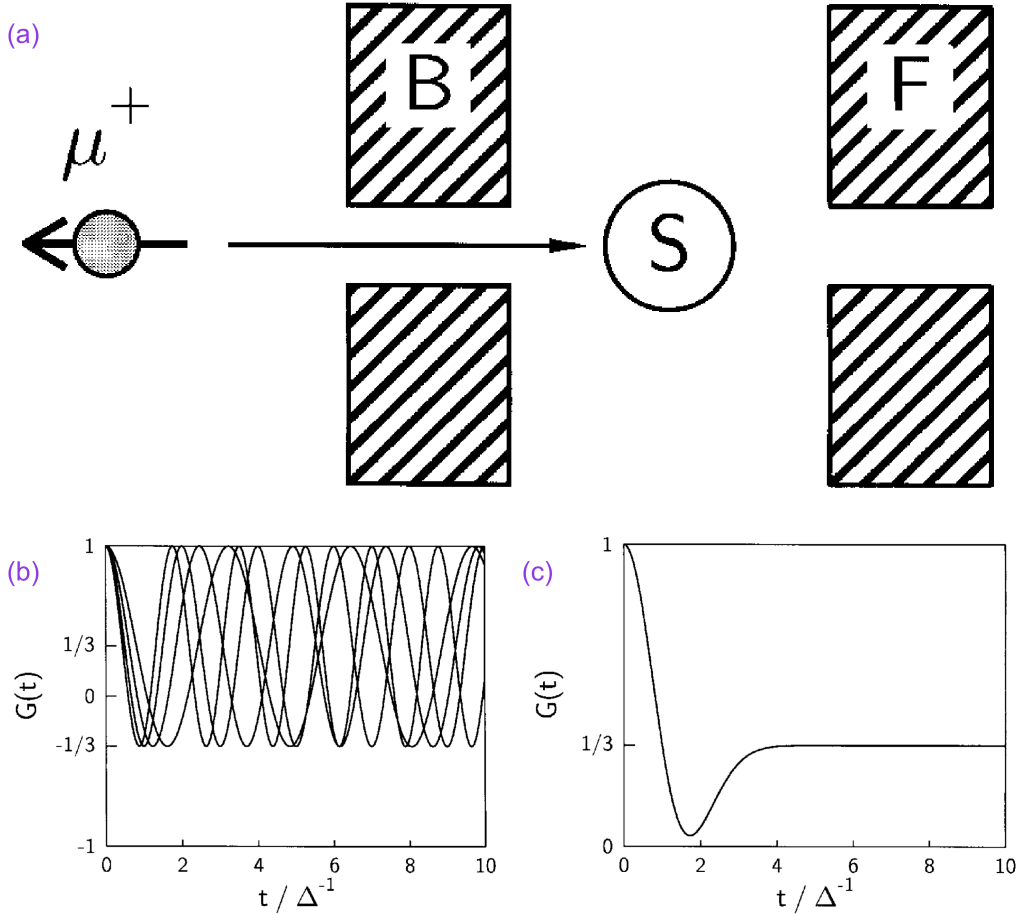
Figure 4.1: (a) Schematic illustration of a μSR experiment. A spin-polarized beam of muons is implanted in a sample **S**. The muons impregnated within the sample **S** will then precess when they are exposed to a magnetic field, either with an internal and/or a transverse external magnetic field. Following the muon decay, positrons are then detected in either a forward detector **F** or a backward detector **B**. (b) The time evolution (t) of the normalized decay positron asymmetry function ($G(t)$) for muons exposed to various internal magnetic field magnitudes. (c) The averaging of terms from (a) yields the Kubo-Toyabe relaxation function [225], where the relaxation rate is dependent upon the average magnetic field strength. Image and plots were originally published in [224] and can be found on the journal's web site: www.tandfonline.com.

magnetic field (Fig. 4.1(c)) [225]. As a result, plotting and fitting the ZF-μSR data to the

Kubo-Toyabe model above and below the superconducting transition will provide direct in-

sight as to whether there is an additional magnetic moment from spin-triplet Cooper pairing within a superconducting state. This $G(t)$ behavior is also expected within ZF-μSR experiments on single crystals with randomly orientated spin-triplet Cooper pairs or randomly orientated single crystals [226]. It should be noted that there is a slight difference between the magnitude of the relaxation rate when $P_\mu \parallel c$ and $P_\mu \perp c$ in ZF-μSR experiments on single crystals of Sr_2RuO_4 [227], however the nature of this material is still hotly debated to this day [228]. Yet to this day, there is no clear example of a superconductor with directionally dependent spin-triplet Cooper pairs. If a material were to exhibit this behavior then it could be determined by anisotropic ZF-μSR experiments. Overall, more can be learned about this technique and the experimental setup in the following sources [4, 84, 224].

4.2 Background and Motivation on LaNiGa$_2$

Interest in LaNiGa$_2$ started when a previous report on a polycrystalline sample used ZF-μSR experiments to show the onset of an additional magnetic source within the superconducting state [19]. Fig. 4.2(a) shows the modest shift of the ZF-μSR curves from LaNiGa$_2$ above and within the superconducting state. Since the strength of internal magnetic field is proportional to the Gaussian relaxation rate (σ) in the Kubo-Toyabe model [4, 224], Hillier et $al.$ used these ZF-μSR results to show that with the onset of superconductivity ($T_{sc} \approx 2\,K$) there is an additional source of magnetism within LaNiGa$_2$ (Fig. 4.2(b)). In the end it was calculated that the internal magnetic field increases by $0.02\,mT$ between the normal and superconducting states [4]. The broken time-reversal symmetry was then rationalized by the formation of spin-triplet Cooper pairs within the superconducting state. Similar conclusions were drawn from ZF-μSR experiments on other well-studied condensed matter systems such as UPt$_3$ [229], Sr_2RuO_4 [227], $Sr_{0.1}Bi_2Se_3$ [230], and LaNiC$_2$ [231].

After this ZF-μSR result, the D_{2h} characters tables in tables 2.1-2.4 were employed to originally propose four possible nonunitary spin-triplet order parameters [19]. Each of these possible order parameters could only occur with weak SOC (Table 2.3). Extending from each order parameter was that the single superconducting energy gap should contain nodal features. However, subsequent studies showed evidence for nodeless multigap behavior (Fig. 4.2(c)) [14], in contradiction with originally proposed single-band spin-triplet order parameters. Following these experimental results, an interband pairing model was proposed [14], wherein Cooper pairs form between electrons with the same spin but originating from different bands. This model was eventually expanded upon in the internally antisymmetric nonunitary triplet pairing (INT) state proposed by Ghosh *et al.* [232]. It was noted that for this pairing state to stabilize, the pairing amplitude between the electrons has to overcome the small band splitting of the quasi-degenerate FSs. As a result the Bogoliubov-deGennes (BdG) quasiparticle bands showed a small energy gap between electrons with the same spin but originating from different bands (Fig. 4.2(d)). Overall this INT state was shown to account for both the broken time-reversal symmetry and the nodeless two energy gaps within the superconducting state.

All previous experimental investigations were limited to polycrystalline samples and theoretical considerations were based on the previously reported symmorphic $Cmmm$ (#65) space group [209]. We reveal that single crystal X-ray diffraction (SCXRD) analysis improves upon previous powder X-ray diffraction (PXRD) work and properly assigns LaNiGa$_2$ to a nonsymmorphic $Cmcm$ (#63) unit-cell. Difficulty discerning the difference between $Cmmm$ and $Cmcm$ from PXRD data has historical precedent [233–235].

We now report that the time-reversal symmetry breaking superconductor LaNiGa$_2$ derives its unconventional superconducting pairing from the previously unknown existence of
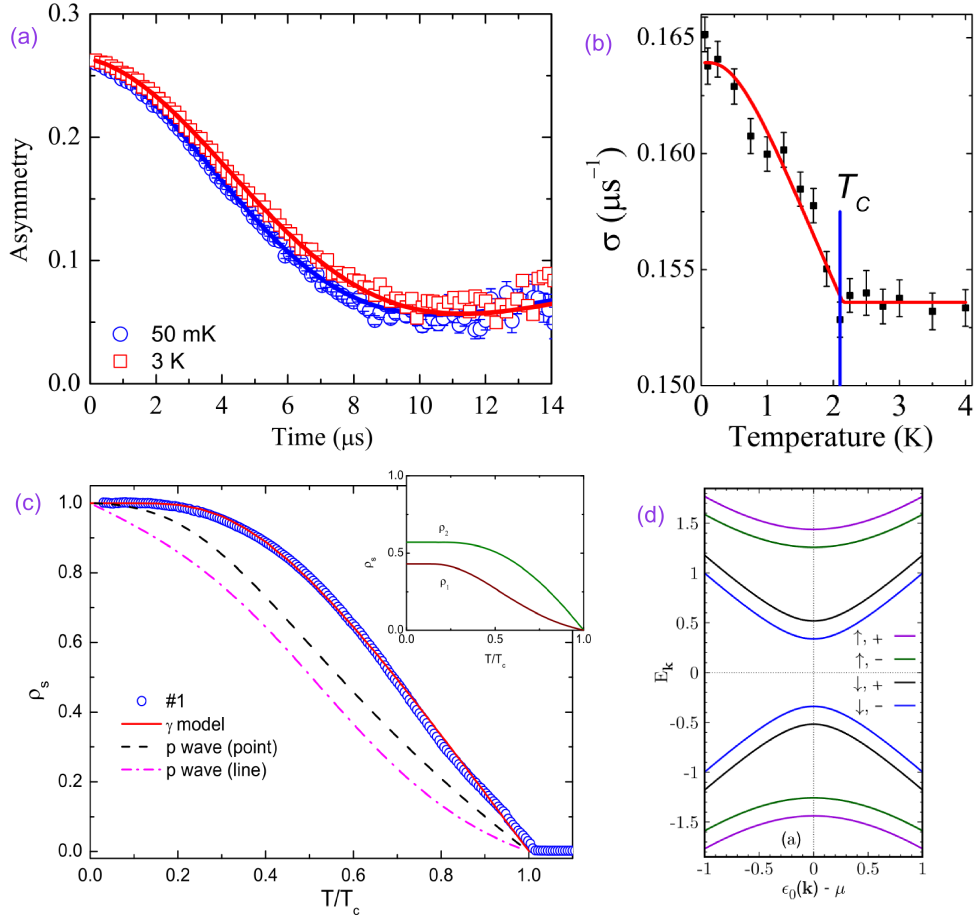
Figure 4.2: Compiled plots of previous experiments on LaNiGa$_2$. (a) The ZF-μSR spectra of LaNiGa$_2$ collected at 56 mK (blue circles) and at 3.0 K (red squares). Each spectra was fit to a least squares fitting (solid lines). The slight shift from 3.0 K$\rightarrow$ 56 mK indicates an additional source of magnetism within LaNiGa$_2$. Plot was originally published in [19]. (b) Shows the temperature dependence of the Gaussian relaxation rate (σ) in zero-field. σ is associated with the internal magnetic field strength and each value was calculated from a Kubo-Toyabe function [225]. The sharp and distinct uptick at the superconducting transition (vertical blue line) shows the onset of spontaneous fields as LaNiGa$_2$ enters the superconducting state. Plot was originally published in [19]. (c) Superfluid density ($\rho_s(T)$) against the normalized temperature (T/T_c). The solid line shows the fitted two-band model, while the dashed and dashed-dotted lines show p-wave models with point and lines nodes, respectively. The inset shows the individual components of the two-band model. Plot was originally published in [14]. (d) BdG quasiparticles from the INT state for the $+$ and $-$ bands for $\uparrow$ and $\downarrow$ spins. Plot was originally published in [232].

105

Dirac lines and Dirac loop in the normal state. The nonsymmorphic symmetries of this new unit cell transform the $k_z = \pi/c$ plane, of the Brillouin zone (BZ) into a node-surface which hosts four-fold degenerate bands [236]. Here, the band degeneracies form two distinct Dirac crossings between two sets of Fermi surfaces (FSs) precisely *at* the Fermi level, independent of chemical potential position. There are fluted lines closed by BZ periodicity and a closed loop. Of special note is that the Dirac loop contains two points which are protected against splitting from spin-orbit coupling (SOC). These features are pinned at the Fermi energy where they impact low energy properties including superconductivity. The rich topology of the electronic structure originates from the nonsymmorphic symmetry that guarantees band degeneracies, which in turn, enable interband and/or complex superconducting order parameters that can break time-reversal symmetry.

These "touchings" are shown from our band structure calculations, along with ARPES data. We note that, among non-magnetic materials and outside of intercalated Bi_2Se_3, no other time-reversal symmetry breaking superconductor has been shown to exhibit a topological band structure (see Table 4.4), thus making $LaNiGa_2$ unique amongst this small set of bulk superconductors. We also discuss the impact of the topology of $LaNiGa_2$ as a natural platform for interband pairing and/or complex superconducting order parameter that can break time-reversal symmetry.

As discussed in section 2.1, the combination of superconductivity with topology is expected to exhibit new types of quasiparticles such as non-Abelian Majorana zero modes [237, 238], or fractional charge and spin currents [239], and provide new platforms for quantum computation technologies [240]. Topological superconductivity can be artificially engineered in hybrid structures [48, 241–244] or it can exist intrinsically in certain unconventional superconductors [52, 53, 57, 71, 245, 246]. In most intrinsic TSCs, the unconventional nature

of superconductivity originates from the proximity to magnetic instabilities or strong electronic correlations [53]. Our results illustrate a novel method towards realizing intrinsic (single-material) topological superconductivity wherein the underlying space group symmetry intertwines the topology with the unconventional superconductivity.

4.3   Methods

4.3.1   Electronic Structure Methods

Density functional based electronic structures were produced by the precise linearized augmented planewave code WIEN2K using the generalized gradient functional for exchange and correlation. The sphere sizes were, in bohr: La, 2.50; Ni, 2.40; Ga, 2.12. The plane wave cutoff K_{max} was determined by $RK_{max} = 7$, and the k-point mesh for self-consistency was $14 \times 14 \times 14$. These calculations were completed by our collaborators Yundi Quan and Warren E. Pickett.

4.3.2   ARPES Measurements

ARPES measurements were performed at Stanford Synchrotron Radiation Lightsource National Laboratory beamline $5 - 2$ using a Scientia DA30 electron spectrometer. The crystal for ARPES was cleaved in the $a - c$ plane using the natural platelet shape of the crystals and a top post. Samples were cleaved *in-situ* at $20 \, \text{K}$ and with a pressure better than $5 \times 10^{-11} \, \text{Torr}$. These experiments were completed by our collaborators Matt C. Staab and Inna M. Vishik.

4.4 Physical and Superconducting Properties

4.4.1 Structural Characterization

Single Crystal X-ray Diffraction and Unit Cell

SCXRD data were collected on several samples and each dataset resolved to a $LaNiGa_2$ unit cell with a $Cmcm$ space group. Given the inherent similarities between the previously reported $Cmmm$ structure [209] in real space, nearly all diffraction spots within the reciprocal space are predicted by both structures. This is especially true for the most intense, low-angle diffraction spots. There are, however, a few observable differences amongst the weakly-diffracting high-angle spots that are sufficient to differentiate the two structures, as shown from the compiled $hk0$ precession image in Fig. 4.3(a).

These discrepancies are highlighted by the differing expected intensities along the normalized $h\bar{9}0$ line, red arrows in Fig. 4.3(a), between the two structures (Fig. 4.3(b)). It should be noted that all peaks along this line from both models are displayed, regardless of intensity. The insufficient intensities for the $Cmmm$ model at these high-angle spots reveal that the previously reported structure inadequately matches the observed diffraction data for this material. The data indicates that the more accurate structure for this material is that of the $Cmcm$ space group.

The new crystal structure retains a Z value of four (with two f.u. in the primitive cell) and contains four unique atom positions comprised of one La, one Ni, and two Ga. Details of the SCXRD experiment are highlighted in Table 4.2 and atomic positions in Table 4.3. When observing the crystal structure projected down the a and c-axes (Fig. 4.4), the structure can be viewed as layers of each element stacking along the b axis. These layers can be described as centrosymmetrically sandwiched together with (1) body-centered planes of Ga
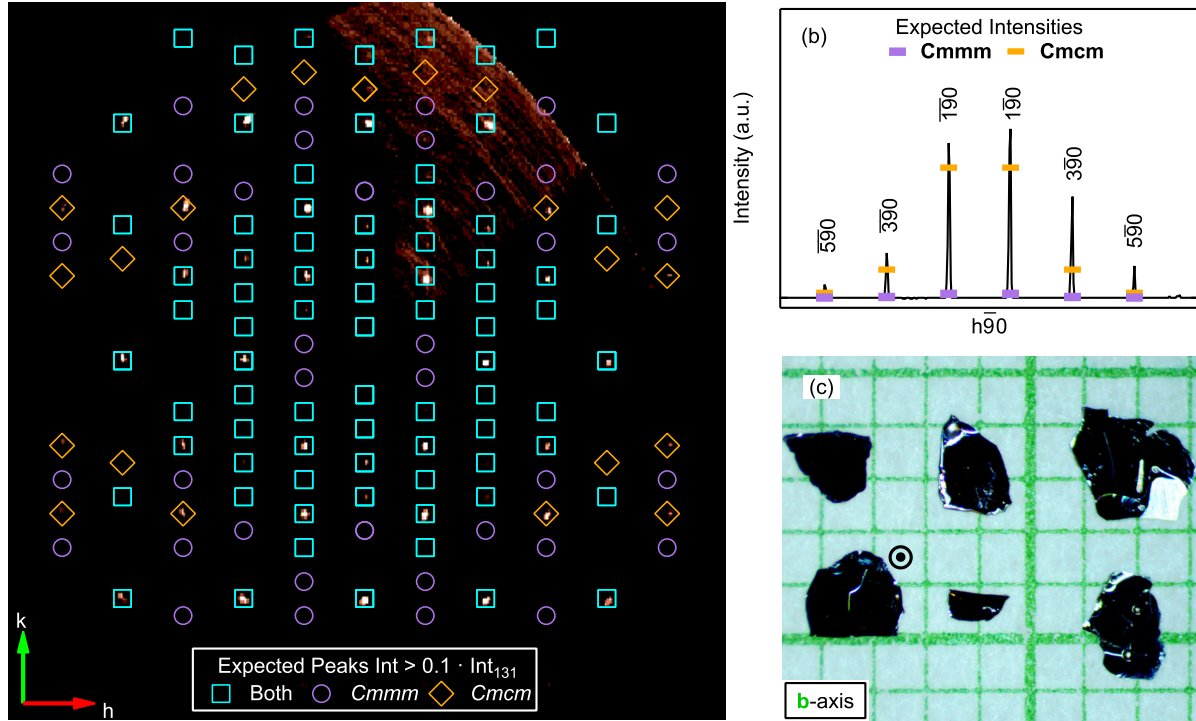
Figure 4.3: (a) Compiled precession image of the $hk0$ plane from a SCXRD data set of LaNiGa$_2$. Overlaid are the predicted diffraction spots with a normalized intensity above 0.1. The diffraction spots which are expected for both the original $Cmmm$ [209] and our newly proposed $Cmcm$ structures are denoted by the teal squares. While the spots which are only expected for the $Cmmm$ and $Cmcm$ structures are shown by the purple circles and orange diamonds, respectively. (b) A normalized linear cut of the $hk0$ precession image along the $h\bar{9}0$, shown by the red triangles in (a). All intensity data, raw and theoretical, from (a) and (b) are normalized to the 131 peak. (c) Picture of representative single crystal samples of LaNiGa$_2$. The plate-like samples have the b-axis normal to the surface of the crystals.

atoms encasing the motif. Moving inward there are planes of (2) Ni atoms, (3) La atoms, and (4) Ga atoms; each of which are transitionally offset from their respective counterpart plane by $(0, 0, \frac{1}{2})$. These structural projections also show the symmetry elements associated with the $Cmcm$ space group, as highlighted by the colored lines. These operations include the reflection and translation of the c glide plane.

This structure as a whole is bound together by interlayer bonding between the (1) Ga
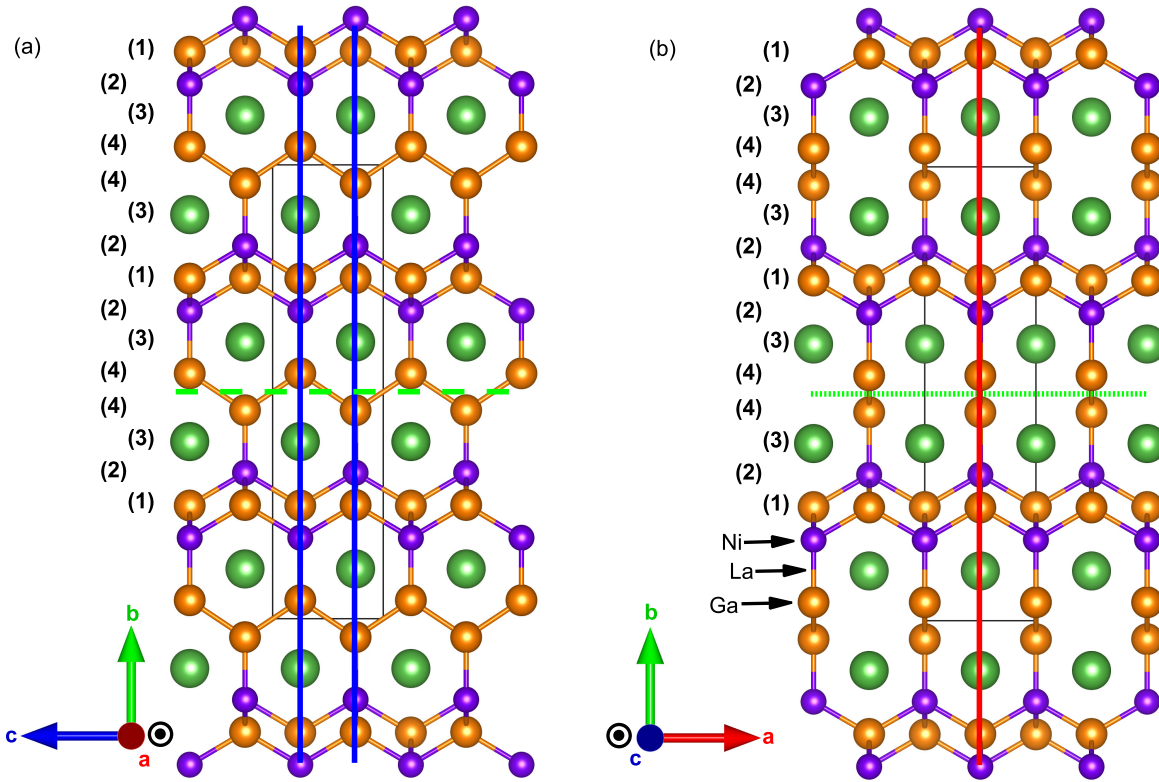
Figure 4.4: Projection of the new LaNiGa$_2$ structure along the a) a and b) c axis. The numbers denote the layers within the structure: (1) body-centered Ga plane, (2) Ni, (3) La, and (4) Ga. The vertical red and blue lines represent the location of the mirror planes, while the dashed green lines denote the c glide plane perpendicular to the b axis.

- (2) Ni, (2) Ni - (4) Ga, and the inner (4) Ga planes. The Ga-Ni bonds allow for the (1) body-centered Ga planes to form tetrahedral sheets with the (2) Ni atoms as the end caps. This motif is the same as in β-FeSe layers, except with the 3d and 4p elements swapped between the two structures. Differing from β-FeSe, the capped (2) Ni atoms bond to the inner (4) Ga layers. The (4) Ga is bonded to its offset counterpart to form a Ga-Ga zigzag chain extending in the c direction. Additionally, all these bonds between two (1) planes come together to form hexagonal sheets, which are shifted by $(\frac{1}{2}, 0, 0)$ every-other sheet

110
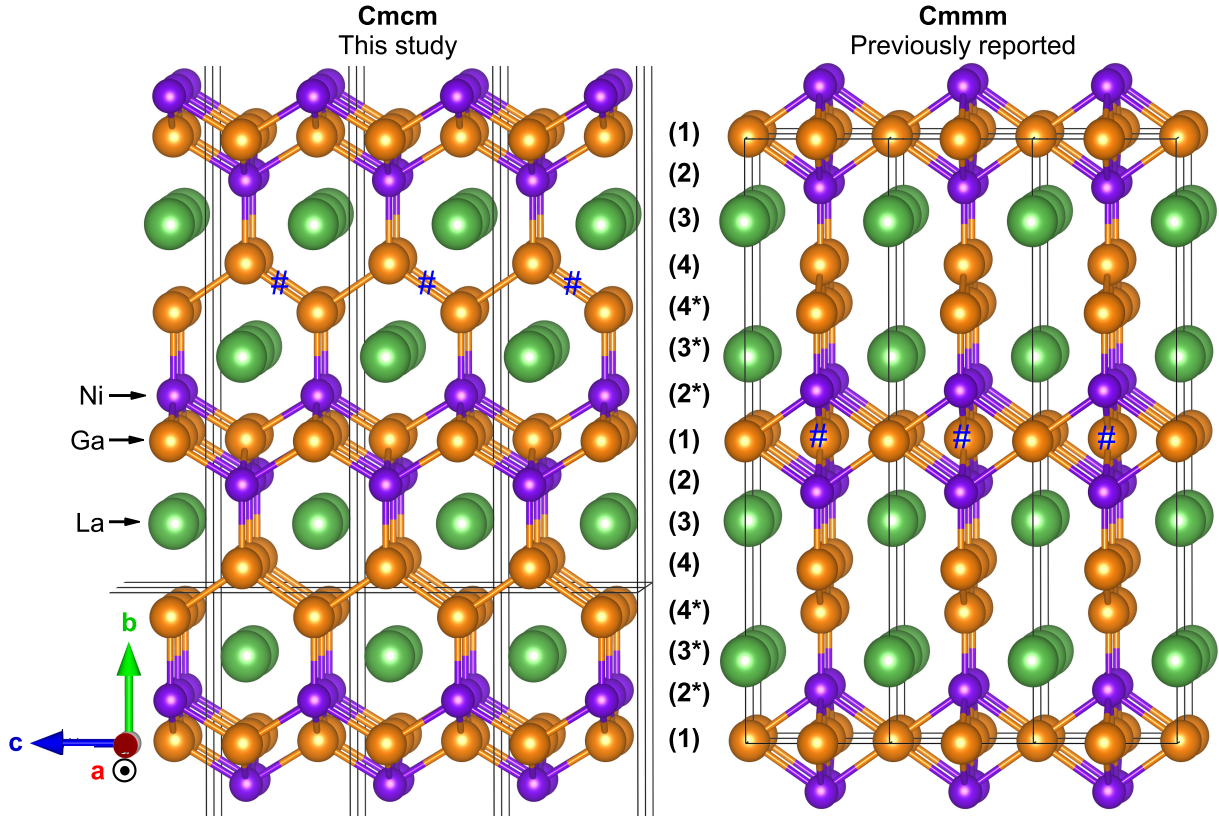
Figure 4.5: Comparison of the normalized *slabs* between the new *Cmcm* (left) and the old *Cmmm* (right) structures. The black lines represent the border of every present unit cell. The inversion center within each unit cell is denoted by the blue # symbol. The referenced axes apply to both structures.

along the *b* direction. In whole, these bonds allow for the formation of La channels both between the stacked hexagonal sheets along the *c* direction and within each hexagon along the *a* direction.

One feature of note is that within the (2), (3), and (4) layers the intraplanar atoms combine to form planar rectangular primitive cells. Despite the different elements, each of these planar cells have separations that are equivalent to the *a* and *c*-axes. In addition to highlighting the aforementioned layered motif, these structural projections also show the symmetry elements associated with the *Cmcm* space group, the colored lines. These

111

operations include the reflection and translation of the c glide plane perpendicular to the b-axis.

Not surprisingly, there are many structural features that overlap between the $Cmcm$ and $Cmmm$ unit cells. Beyond the obvious similarities in unit cell dimensions and point group, both structures comprise of the previously mentioned layers and *slabs*. The planes within these repeating motifs appear in the same sequence and the interlayer distances are very similar. When normalized, the largest difference is $0.2\,\text{Å}$. Since both structures contain these *slabs* and every other (1) body-centered Ga plane is positionally identical within the $a - c$ plane, we can easily compare the contents of the two structures. When these layers are normalized to the same positions, as can be observed in Fig. 4.5, we see that within the $Cmcm$ *slab* every other section of the (2), (3), and (4) is shifted by $(\frac{1}{2}, 0, \frac{1}{2})$, denoted by the starred numbers. While the $Cmmm$ *slab* does not exhibit any shifting. This simple translation is the only structural difference and is sufficient to cause the border of the unit cells to shift and subsequently the center of inversion to shift from the central Ga atom within (1) plane in $Cmmm$ to half-way between the (4) layers in $Cmcm$. With regards to the bonding, these shifted atoms transform the Ga-Ni tetrahedral sheets into pseudo-square planar atom sites and eliminate the translation shift between the hexagonal sheets.

Additionally of note, the $Cmmm$ to $Cmcm$ structures contain the same number of Ni and La sites, but a different number of Ga sites. Transforming from the $Cmmm$ to $Cmcm$, the first and second Ga site locations, comprising the (1) plane, converge to a single site location. Although there is an additional site location in $Cmmm$, both the first and the second sites fall on a Wyckoff position with a multiplicity of 2. In contrast, the converged site in $Cmcm$ falls on a Wyckoff position with a multiplicity of 4, thus retaining the stoichiometry between the two structures.

When thinking about the structural identification saga of $LaNiGa_2$, we could not help but be fascinated by the similarities with that of the superconducting ferromagnet UGe_2 [234, 235]. The initial structural misidentification of the two materials follows in nearly the same path, except in opposite directions. Originally thought to have a $Cmcm$ space group, it was not until single crystal structural experiments were performed on UGe_2 that the true $Cmmm$ space group was properly identified [233–235]. Beyond similar difficulties with identifying the proper space group, the structural framework of UGe_2 and $LaNiGa_2$ (ignoring Ni) would be identical if they were both $Cmmm$. However, this new space group identification changes the two structures in the manner previously mentioned.

Overall, while this new space group remains centrosymmetric, it adds nonsymmorphic symmetries: a c glide plane perpendicular to the b-axis and a 2_1 screw axis, $\mathcal{S}_2^z$, along the c-axis. First we will discuss the physical properties of the single crystals of $LaNiGa_2$ then discuss the influence of the new symmetry operations on the electronic structure and the ramifications on the superconducting pairing state.

Powder X-Ray Diffraction

Fig. 4.6 shows the powder X-ray diffraction (PXRD) results with a LeBail refinement using the previously reported structure [209, 247] and the new $Cmcm$ structure. The fittings were made using GSAS-II [248]. In addition to $LaNiGa_2$, there was a small amount of impurity flux that is either the LaNiGa or $LaNi_3Ga_2$ phase (blue triangles Fig. 4.6). The refined unit-cell parameters from the $Cmmm$ structure are $a = 4.278\,\text{Å}$, $b = 17.436\,\text{Å}$, and $c = 4.271\,\text{Å}$. The refined unit-cell parameters from the $Cmcm$ structure are $a = 4.273\,\text{Å}$, $b = 17.412\,\text{Å}$, and $c = 4.268\,\text{Å}$. Since both the $Cmmm$ and $Cmcm$ structures model well onto the PXRD data (wR= 7.026% and 7.084%, respectively), SCXRD is the best technique to experimentally
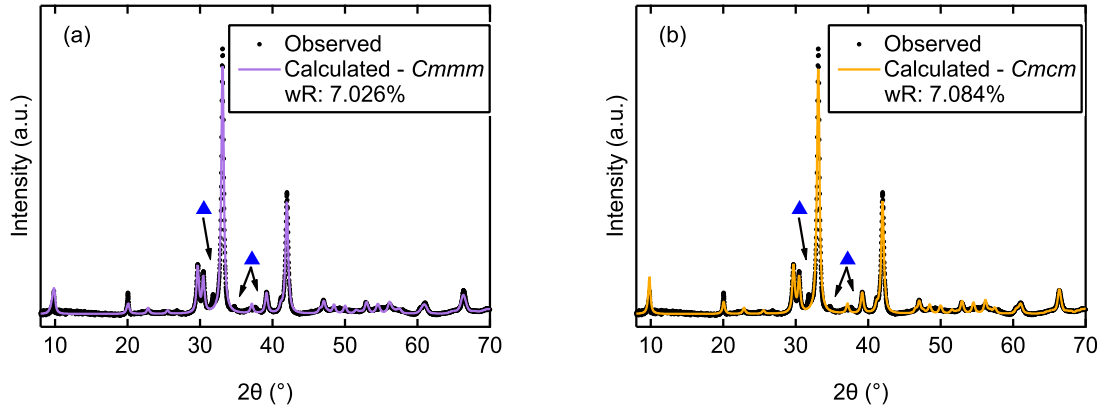
Figure 4.6: Background subtracted PXRD pattern of LaNiGa$_2$ that was collected from ground single crystals (black dots). The overlaid lines are the calculated models from GSAS-II using the (a) previously reported *Cmmm* and the (b) new *Cmcm* structures. The blue triangles denote the peaks from the unidentifiable flux.

distinguish the correct structure.

4.4.2 Magnetic Susceptibility

Magnetic susceptibility with a magnetic field of $1\,\mathrm{mT}$ along the *b*-axis is shown in Fig. 4.7. Temperature dependence was collected under zero-field cooled (ZFC) and field cooled (FC) conditions. A clear diamagnetic response is observed, with an almost complete expulsion of the external magnetic field for the ZFC curve. The superconducting transition, T_{sc}^{M}, is selected when the material reaches a 90% shielding fraction, at $1.92\,\mathrm{K}$. The combination of a sharp transition, $\Delta T = 0.1\,\mathrm{K}$, and the magnitude of the diamagnetic response is consistent with the bulk superconductivity confirmed from heat capacity measurements. The transition temperature is in good agreement with what had been previously reported from both AC and DC susceptibility measurements [14, 210]. The separation of the ZFC and FC curves indicates a moderate presence of flux pinning in a type-II superconductor, and the scale of

114
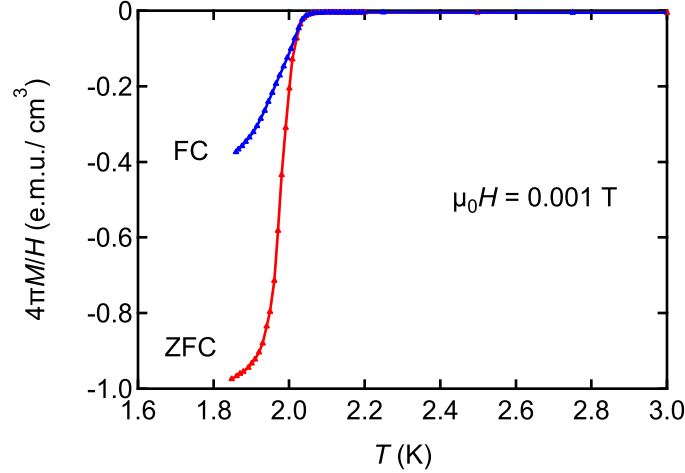
Figure 4.7: The temperature dependence of the zero-field cooled (ZFC) and field-cooled (FC) magnetic susceptibility ($4\pi\, M/H$) curves for LaNiGa$_2$ with a field of $1\,\mathrm{mT}$.

difference is less than previous polycrystalline measurements, which is expected for high-quality single-crystal susceptibility measurements with reduced pinning centers.

4.4.3 Electrical resistivity

Electrical resistivity measured in zero-field for a single crystal is shown in Fig. 4.8. The complete superconducting transition is observed with a $T_{\mathrm{sc}}^{\rho} = 2.06\,\mathrm{K}$ in the inset, while no other anomalies are observed. Fitting the normal state low-temperature region $(3 - 10\,\mathrm{K})$ by a Fermi-liquid behavior: $\rho(T) = \rho_0 + AT^2$ leads to $\rho_0 = 5.20\,\mu\Omega\,\mathrm{cm}$ and $A = 2.54 \times 10^{-4}\,\mu\Omega\,\mathrm{cm}\,\mathrm{K}^{-2}$. The residual resistivity ratio (RRR) for this sample is 9.57. Both ρ_0 and the RRR indicate a higher sample quality than data on polycrystalline samples [210]. Additionally of note, there is a slight negative curvature in the high-temperature region which has been observed in other La-Ni compounds [249, 250], and can arise from $s - d$ interband scattering [251]. The fitting for this scattering was modeled and is shown in Fig. 3.17.

Resistivity measurements under field were conducted to construct the anisotropic upper-
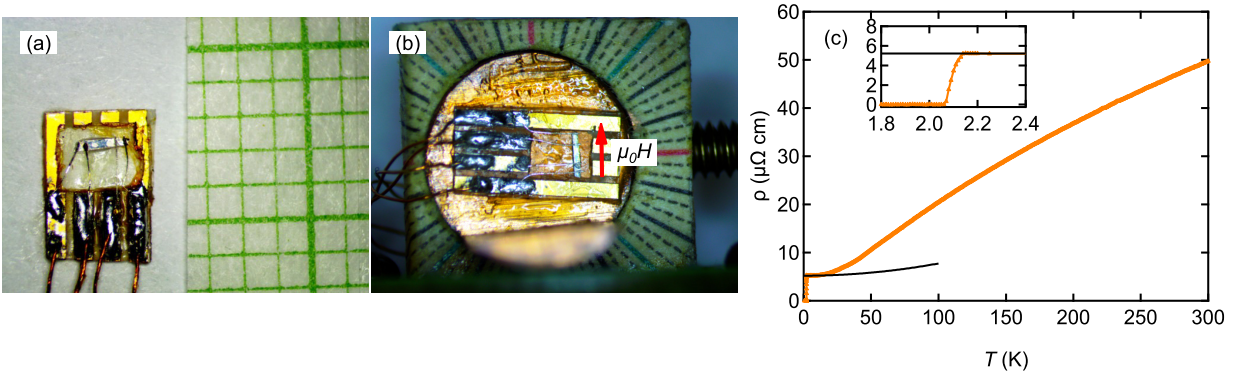
Figure 4.8: (a) Example of a LaNiGa$_2$ crystal with the four-point probe setup and the labeled wires. (b) The same crystal in (a) set up and aligned ($\mu_0 H \parallel c$-axis) for anisotropic $\rho(T)$ and $\rho(H)$ measurements using the ^{3}He probe. (c) Normal-state and superconducting transition in $\rho(T)$ for a representative sample of LaNiGa$_2$. The solid black curve is a fit from the Fermi liquid behaviour of the normal state between $3 - 10$ K. The inset shows the superconducting transition.

critical-field phase diagram. Measurements were completed by performing three sets of temperature-and field-sweeps. Each set had the external magnetic field aligned along a different crystallographic axis. Fig. 4.9 shows the resistivity data when the magnetic field ia aligned parallel to the c-axis.

4.4.4 Heat Capacity

Fig. 4.10(a) shows the heat capacity superconducting transition for LaNiGa$_2$ in zero-field and a suppressed transition down to 0.4 K with a magnetic field of 0.3 T. The normal-state low-temperature specific heat (C/T) shows a T^2 relationship and is fit according to the formula $C/T = \gamma_n + \beta T^2$. From the fit, a Debye temperature $\Theta_D^L = 166$ K and a Sommerfeld coefficient $\gamma_n = 14.1$ mJ/mol K^2 are obtained. These values indicate that LaNiGa$_2$ does not exhibit strong electronic correlations, as expected for a La-based material. Additionally, the high-temperature data is well fit to a weighted high-temperature Einstein-Debye model 3.11.

116
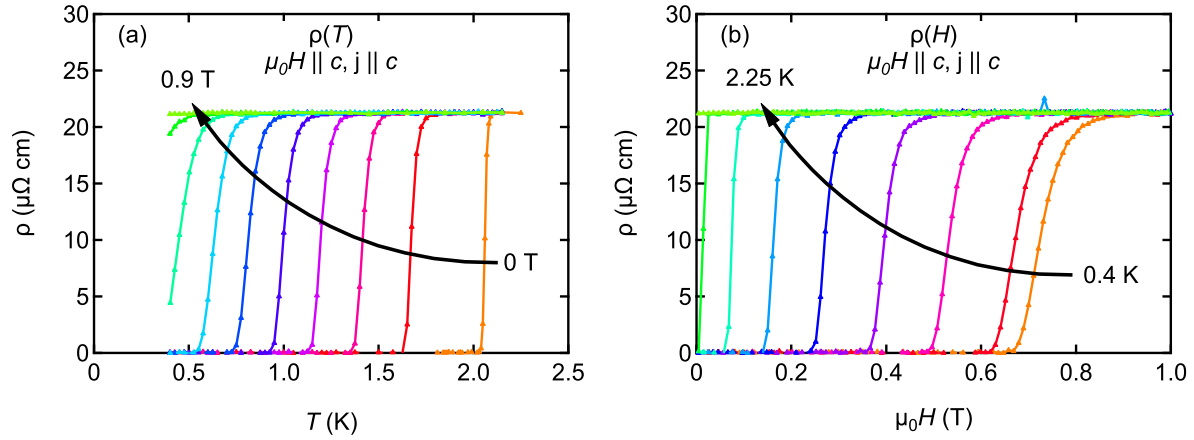
Figure 4.9: Low temperature resistivity data showing the superconducting transition with $\rho(T)$ (a) and $\rho(H)$ (b) sweeps. The $\rho(T)$ sweeps have a constant magnetic field $\mu_0 H = 0 - 0.9\,\text{T}$ in increments of $0.1\,\text{T}$. The $\rho(H)$ sweeps have a constant temperature $T = 0.5 - 2.25\,\text{K}$ and $0.4\,\text{K}$. These representative measurements were complected with $H \parallel c$ and $\text{j} \parallel c$.

In both models, C_{Debye} and C_{Einstein}, there is a single refineable parameter of Θ_D and T_E, respectively. Since the Einstein model is used to approximate the optical phonon contributions [6], it is best to calculate the total number of phonons branches to better estimate the weighted contribution of each heat capacity model. With the new structure, the primitive cell volume of LaNiGa$_2$ is half that of the unit cell, thus 8 atoms in the primitive cell. It follows that there are 24 phonon branches, three of which are acoustic and will have strong contributions from the heavy La atom. The effective Debye model contribution should be $x = 12.5\%$. The inset of Fig. 4.10(a) shows the fitting of the function which gives a Debye temperature, $\Theta_D = 83\,\text{K}$, and an Einstein temperature $T_E = 200\,\text{K}$.

A complete bulk superconducting transition is observed and shown in Fig. 4.10(b). The midpoint of the transition is $T_{\text{sc}}^C = 1.96\,\text{K}$. When normalized with the γ_n value from the low-temperature fit, this specific heat jump equates to $\Delta C / \gamma_n T_{\text{sc}}^C = 1.33$, slightly higher than previously reported value from [14] on polycrystals. Though the specific heat near
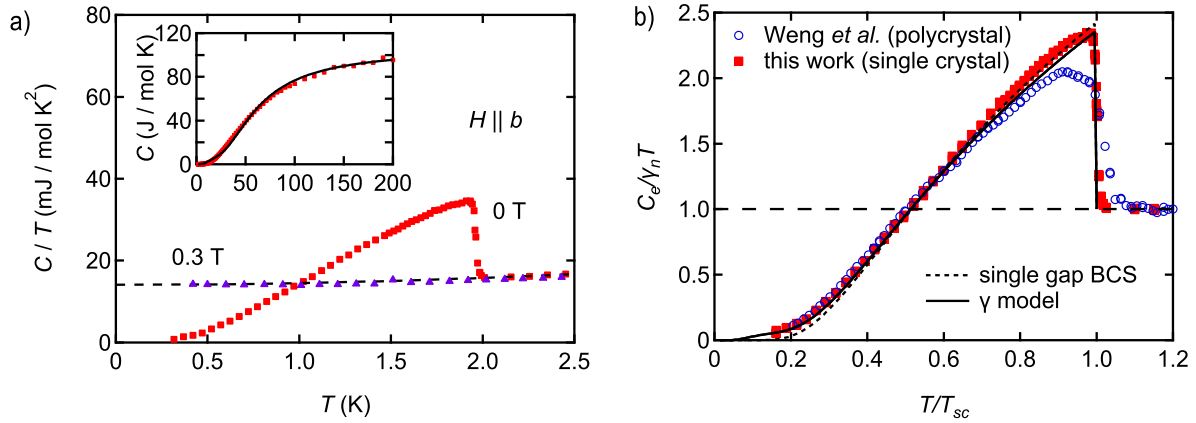
Figure 4.10: (a) Zero-field specific heat (C/T) against T shows the complete superconducting transition. The purple curve shows that a $0.3\,\mathrm{T}$ external field is sufficient to suppress superconductivity below $0.4\,\mathrm{K}$ in heat capacity measurements, a lower value than in resistivity measurements. The dashed black line is the low-temperature T^2 phonon contribution. The inset shows the high-temperature heat capacity, which is fitted to the weighted high-temperature Einstein-Debye model, Eq.3.11. (b) Comparison of the electronic heat capacity measured on polycrystal [14] with our measurement on single crystal. The single gap BCS and a two-gap model based on Ref. [13] (γ-model) are shown. The parameters used for the γ-model are $n_1 = 0.95$, $\lambda_{12} = 0.1$, $\lambda_{11} = \lambda_{22} = 0.45$.

T_{sc} seems to be well described by the single-gap BCS theory, the low temperature data can be better described by a two-gap model [13] (see Fig. 4.10(b)) as already reported for polycrystals [14]. We note that the heat capacity is reported down to $0.4\,\mathrm{K}$, which is significantly higher than the reported penetration depth measurements down to $0.05\,\mathrm{K}$ upon which the nodeless multigap behavior was inferred [14]. Heat capacity measurements at lower temperatures are necessary to better assess the superconducting gap structure.

The Kadowaki-Woods ratio (KWR)[252, 253] calculated as A/γ_n^2 is equal to $1.28\,\mu\Omega\,\mathrm{cm}\,\mathrm{mol}^2\,\mathrm{K}^2\,\mathrm{J}^{-2}$ confirming that LaNiGa$_2$ is not a strongly correlated material.
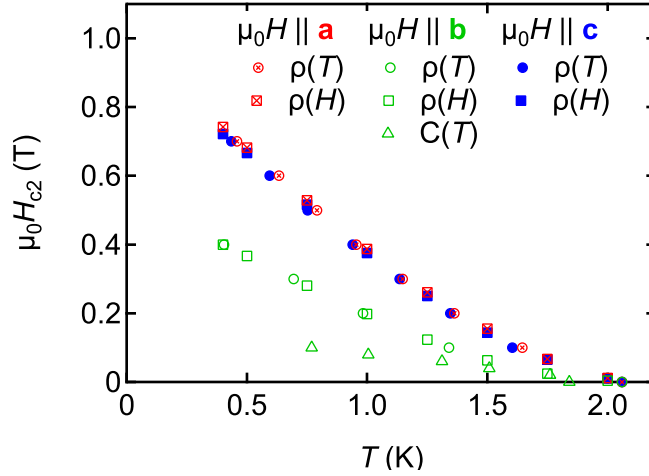
Figure 4.11: Anisotropic field-temperature $\mu_0 H_{c2}$ phase diagrams of LaNiGa$_2$ when H is applied along each of the three crystallographic axes.

4.4.5 Upper Critical Field Phase Diagram

The anisotropic H_{c2} phase diagram is constructed by tracking the superconducting transition across resistivity and heat capacity temperature- and field-sweeps for an aligned LaNiGa$_2$ crystal. These measurements were collected with an external magnetic field carefully oriented along particular crystallographic axes (Fig. 4.11). Regardless of the orientation, there is a clear upward curvature of the H_{c2}, which is a common feature for multiband superconductivity and was previously noted on polycrystalline samples of LaNiGa$_2$ [14].

Additionally, from the Helfand-Werthamer model the critical field at $0\,$K can be approximated for a single band system:

$$\mu_0 H_{c2}(0) = -A T_{\text{sc}} \frac{d\mu_0 H_{c2}(T_{\text{sc}})}{dT}, \tag{4.1}$$

where $A = 0.73$ and 0.69 for the clean and dirty limits, respectively [254]. Estimated values of $H_{c2}(0)$ from the slope near T_{sc} are lower than $0.275\,$T for all three field directions,

119

and lower than the experimental values near $0.4\,\mathrm{K}$. Thus indicating that a single band model, either in the clean or dirty limit, cannot accurately model this system. This is further evidence for the suggestion that multi-band effects are important. The experimental and calculated superconducting properties are summarized in Table 4.1. Additionally, from the critical temperature, T_{sc}^C, the Pauli paramagnetic limit is calculated by $\mu_0^p H_{c2}(0) = 1.84 T_{\mathrm{sc}}^C = 3.66\,\mathrm{T}$ [255]. Since all three axes have critical fields below this limit, an orbital pair-breaking mechanism may be operating. As shown in section 4.4.4, LaNiGa$_2$ is not a heavy fermion material ($\gamma_n = 14.1\,\mathrm{mJ\ mol^{-1}\ K^{-2}}$) and interband pairing is suppressed by the application of a strong magnetic field. Thus the upper-critical field in LaNiGa$_2$ remains orbital limited, even though time-reversal symmetry breaking superconductivity was observed at zero field in μSR experiments.

4.4.6 Superconducting and Physical Properties

Within the superconducting state, we can start by calculating the anisotropic Ginzburg-Landau (GL) coherence lengths, ξ_{GL}, by using the relation:

$$\frac{d(\mu_0 H_{c2}^a(T_{\mathrm{sc}}))}{dT} = \frac{-\Phi_0}{2\pi \xi_{GL}^b \xi_{GL}^c T_{\mathrm{sc}}} \tag{4.2}$$

where Φ_0 is the quantum flux, $\mu_0 H_{c2}^a$ is the of the $\mu_0 H_{c2}$ curve when field is parallel to the crystallographic a-axis, and ξ_{GL}^b andξ_{GL}^c are the coherence lengths along the b- and c-axes [5, 256]. Given the orthorhombic nature, by measuring the slope of H_{c2} along each axis near T_{sc} we can find the corresponding coherence lengths. From this linear system of equations, ξ_{GL}^a, ξ_{GL}^b, ξ_{GL}^c are calculated out to 51.5, 17.6, and $47.3\,\mathrm{nm}$, respectively.

With the $H_c(0)$ and the anisotropic ξ_{GL} values, the anisotropic penetration depths can be calculated with [5, 256]:

Property (Unit)	Value
T_{sc} (K)	1.96
γ_n (mJ mol^{-1} K^{-2})	14.1
Θ_D (low temp.) (K)	166
Θ_D (K)	82.7
T_E (K)	200
$\Delta C/\gamma_n T_{sc}$	1.33
ρ_0 ($\mu\Omega$ cm)	5.20
A ($\mu\Omega$ cm T^{-2})	2.54×10^{-4}
$\mu_0 H_{c2}^{HW}(0)$ (Clean limit) (T)	0.275, 0.094, and 0.253
$\mu_0 H_{c2}^{HW}(0)$ (Dirty limit) (T)	0.260, 0.089, and 0.239
$\mu_0 H_{c2}^{p}(0)$ (T)	3.66
$\mu_0 H_c(0)$ (mT)	23
ξ_{GL} (nm)	51.5, 17.6, and 47.3
λ_{GL} (nm)	174, 509, and 189
κ	3.37, 28.9, 4.00
KWR $= A/\gamma_n^2$ ($\mu\Omega$ cm mol^2 K^2 J^{-2})	1.28

Table 4.1: Measured and calculated relevant normal and superconducting-state properties for LaNiGa$_2$. All anisotropic parameters have entries in the following order: a-, b-, and c-axis. The T_{sc} was selected as the mid-point from the heat capacity transition.

$$\mu_0 H_c(0) = \frac{\Phi_0}{2\sqrt{2}\pi\xi_{GL}^a\lambda_{GL}^a}$$

From this λ_{GL} for each crystallographic axis is calculated to 174, 509, and 189 nm for the a-, b-, and c-axes, respectively. When averaged across the three penetration depths $\lambda_{GL}^{avg} = 291$ nm, which is in great agreement with the previoulsy reported penetration depth $\lambda_0 = 350$ nm [14]. Lastly, with λ_{GL} and ξ_{GL}, the κ ratio can be determined along each axis: $\kappa^a = 3.37$, $\kappa^b = 28.9$, and $\kappa^c = 4.00$.

Using both the normal and superconducting-state heat capacity data, the isotropic thermodynamic critical field, $H_c(T)$, can be calculated using equations 3.15, 3.16, and 3.17. The $H_c(T)$ curve can be fit to a Taylor expansion equation 3.18 to give a $H_c(0) = 23$ mT

(Fig. 3.25(c).

Lastly, the Kadowaki-Woods ratio (KWR) [252, 253] calculated as A/γ_n^2 is equal to $1.28\,\mu\Omega\,\mathrm{cm}\,\mathrm{mol}^2\,\mathrm{K}^2\,\mathrm{J}^{-2}$ confirming that $LaNiGa_2$ is not a strongly correlated material. All of these superconducting and physical properties are highlighted in Table 4.1.

4.4.7 Electronic Structure

Despite the new structure, Fig. 4.12(a) shows that there remain 5 FSs [232, 257]. Highlighted with the previous space-group, there are several regions within the BZ where pairs of FSs are parallel and quasi-degenerate [14, 232]. A crucial difference now is that the nonsymmorphic symmetry operations force the previously quasi-degenerate FS pairs to "touch" on the $k_z = \pi/c$ plane (red plane) in the absence of SOC, turning this plane into a node-surface [236]. The combination of $\mathcal{S}_2^z$, parity operation, and time-reversal symmetry force bands on the node-surface to be 4-fold degenerate. This symmetry enforced degeneracy results in two disjoint sets of Dirac crossings directly at the Fermi level. Both are between bulk bands crossing the node-surface: fluted lines across the BZ face between FS4/5 and a closed-loop between FS2/3 (highlighted lines top panel Fig. 4.12(a)). That these crossings occur *at* the Fermi level make $LaNiGa_2$ uncommon compared to other superconductors with topologically non-trivial band structures [57, 63–65, 67–69, 71–73] (see 4.4)

The Dirac crossings can be observed in the linear band dispersion plots without SOC along $\vec{k} = (0, 0.516\frac{\pi}{b}, k_z)$ (green arrow) for the Dirac loop (Fig. 4.12(b)) and $\vec{k} = (0.232\frac{\pi}{a}, 0, k_z)$ (blue arrow) for the Dirac lines (Fig. 4.12(d)). We note that small shifts of the Fermi energy will shift the k-space location of the Dirac lines and loop. However, these features will persist at the Fermi level as long as the FSs cross the node-surface. When accounting for SOC, most band crossings become gapped (by a few to $40\,\mathrm{meV}$), as pictured in Fig. 4.12(e). Remarkably,
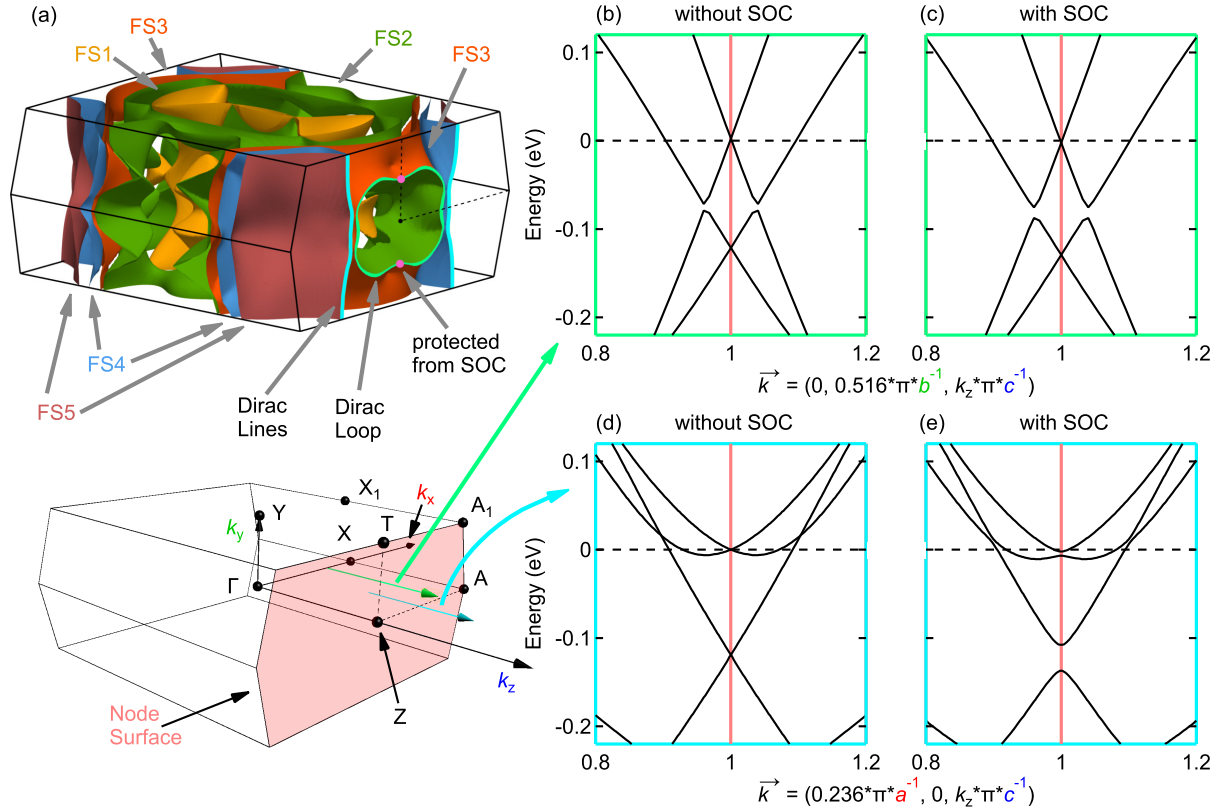
Figure 4.12: (a) Fermi surfaces within the BZ that highlight the Dirac lines (blue lines) and Dirac loop (green line) on the node-surface. The crossings along $Z - T$ (magenta dots) are protected from SOC. Below is the BZ showing several high symmetry points and highlights the node-surface (red plane). The green arrow, $k_y = 0.516\pi/b$, shows where FS2/3 become degenerate on the node-surface. The Dirac crossing is shown to remain with (c) and without SOC (b), where the SOC contribution to anticrossing is seen to be very small. The blue arrow shows the dispersion along $k_x = 0.236\pi/a$ without SOC (d) shows the Dirac lines between FS4/5. Once SOC is added (e), the crossing becomes gapped at the node-surface.

the Dirac points between FS2/3 survive along the $Z-T$ symmetry line under SOC, as seen in Fig. 4.12(c), creating two true-Dirac points at the Fermi level. This protected feature results from the presence of the mirror reflection, $\mathcal{M}_x$, along the $Z - T$ line, therefore, remaining 4-fold degenerate even when accounting for SOC (see Supplementary Information in [223] for derivation), illustrating that this degeneracy lies precisely at E_F, and is robust rather

123

than accidental.

To provide a clear picture of the effect of the nonsymmorphic symmetry operations on the band structure, we show both (without SOC) the band structure from the previous $Cmmm$ space group (bottom panel) and the updated $Cmcm$ unit-cell for LaNiGa$_2$ (top panel) in Fig. 4.13. As previously highlighted both band structures have several bands which cross E_F to produce five FSs. The key difference can be observed at and between the high-symmetry points on the $k_z=\pi/c$ plane. For example, along $\Gamma-Z-A$ in Fig. 4.13 the bands in the $Cmcm$ structure become degenerate on the node-surface (Z and A points). Whereas in the $Cmmm$ structure the bands remain separated on this plane. In the $Cmcm$ electronic structure, the bands 'stick together' as a direct result the previously undetected nonsymmorphic symmetry operations.

4.4.8 ARPES

For ARPES experiments, the crystal was cleaved in the a—c plane along the natural platelet shape of the crystals. With this cleavage plane, photon energy dependence probes the electronic structure along the k_y axis [258]. Fig. 4.14(a) shows a section of a photon energy-dependence sweep from 100 to 184 eV in steps of 2 eV along the BZ diagonal ($k_\parallel$), in the k_z—k_x plane. Each spectrum was integrated ± 50 meV around the Fermi energy for each photon energy. The ARPES data can be compared to calculated dispersions along the same cut and yield qualitative agreement (Fig. 4.14(b)). Although we note that photoemission matrix elements can be a function of photon energy and can cause features to be weaker or absent at some photon energies. Both data and theory have consistent features that largely do not disperse as a function of photon energy or k_y for the chosen cut geometry, corresponding to FS3 and FS4. Near these minimally-dispersing features, but closer to the
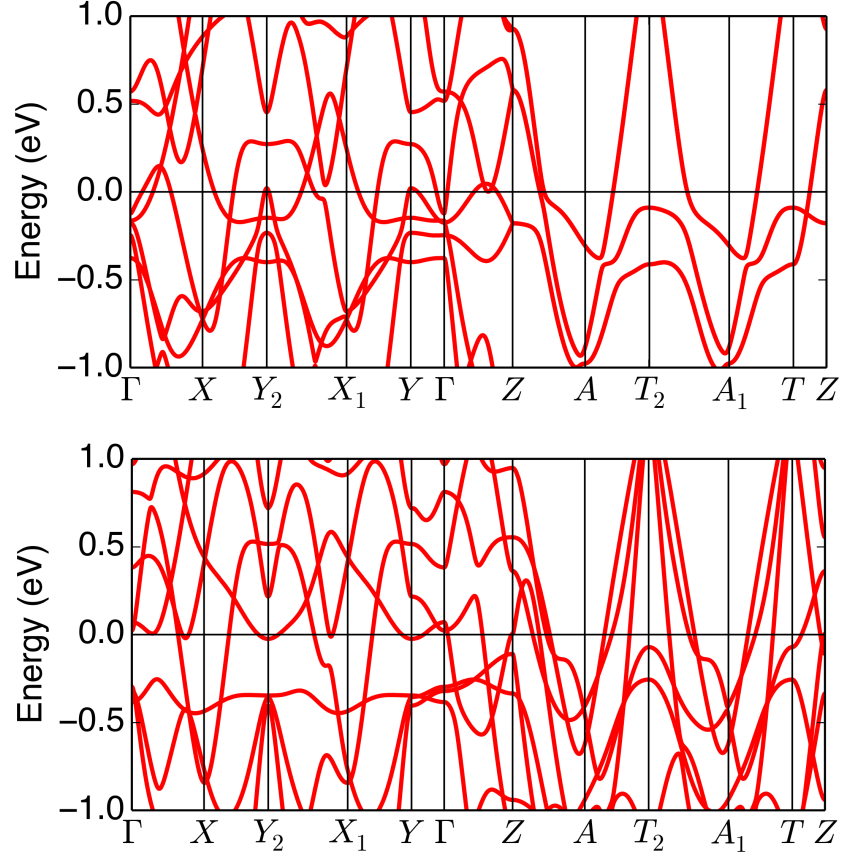
Figure 4.13: Band structure of nonsymmorphic $Cmcm$ (top panel) versus symmorphic $Cmmm$ LaNiGa$_2$ (bottom panel), on a fine scale near E$_F$. See Fig. 4.12 for symmetry points. Fermi level band crossings are different for $Cmcm$, resulting in different Fermi surfaces than those shown by Singh [257] Although 5 FSs remain for both structures.

zone corner, is FS5, which moves closer to surfaces FS3 and FS4 at the $k_y = 0$ plane, and further away at the edge of the BZ. FS2, which is closer to the zone center, also moves closer to the minimally-dispersing surfaces at the $k_y = 0$ plane. This is one way we identify $144\,\text{eV}$ as the $k_y = 0$ plane. The other way we correspond photon energy with k_y value is at the BZ boundaries. In the DFT calculation, there is more spectral weight at the BZ boundaries at $k_\parallel = 0$, which is consistent with the enhanced intensity observed at 122 and $166\,\text{eV}$ in ARPES data near $k_\parallel = 0$. The $k_y = 0$ ($144\,\text{eV}$) plane is schematically shown in Fig. 4.14(a)
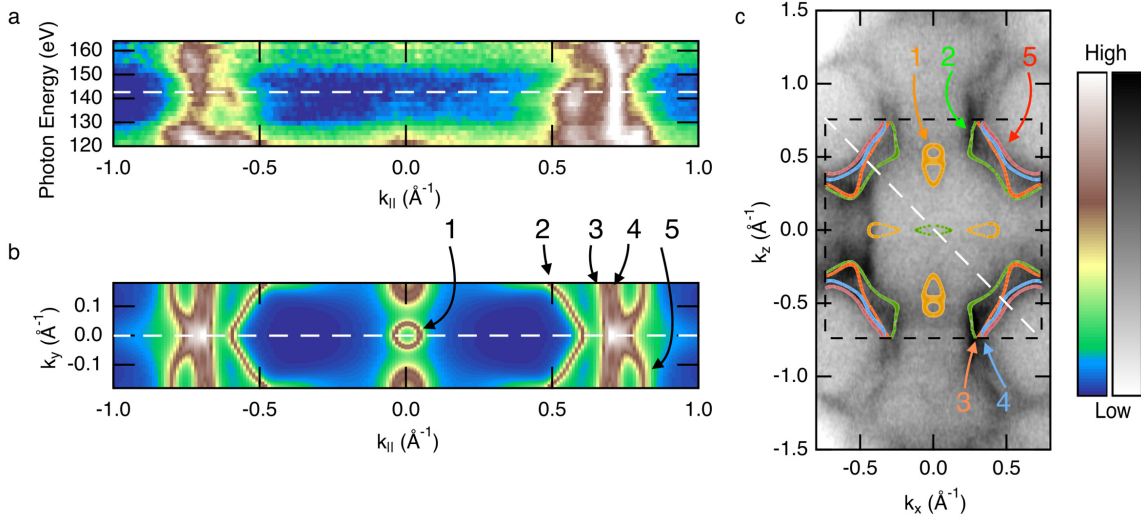
Figure 4.14: Comparison of ARPES to DFT. (a) Photon energy dependence of ARPES intensity along the Γ-A diagonal, $k_\parallel$, through the BZ. (b) DFT calculation of spectral weight $A(\vec{k}, \omega)$ along the same plane as (a). Comparing the structure of (a) and (b) indicates that the $k_y = 0$ plane of the BZ can be accessed with a photon energy of 144 eV. (c) Shows the overlay of Fig. 4.12(a) and (b) to visualize the agreement of the DFT with the measurements. The white dashed line in (c) shows the corresponding cut location from (a) and (b)

and (b) by the white dashed line. The overlaid data of Fig. 4.15(a) and (b) is shown in Fig. 4.14(c) and the white dashed line in this plot corresponds to the BZ diagonal $k_\parallel$.

Single crystals of LaNiGa$_2$ do not naturally cleave perpendicular to the crystallographic c-axis, making a direct observation of the Dirac dispersion by ARPES measurements challenging. However, with a photon energy of 144 eV we can probe the $k_y = 0$ plane and confirm the presence of the band touchings. Fig. 4.15(a) shows the constant energy map centered at E_F and reveals the most prominent features of the spectra: the ruffled cylindrical bands centered on the BZ corners. Given that, near the corner of the BZ, the calculated FSs are very close to each other (see Fig. 4.15(b)), it is difficult to discern which bands are observed in the ARPES measurements from just this plane. Overlaid on Fig. 4.15(c) are the respec-

126

tive DFT band calculations (dashed lines) which reveal that the most prominent bands in the ARPES data originate from the bands associated with FS2 and FS3. The three parallel horizontal cuts on and near the node-surface show the band dispersion plots at and below E_F (Fig. 4.15(c)). The green line, spectrum 2, represents the cut exactly on the node-surface, while the blue, spectrum 1, and red, spectrum 3, lines are parallel cuts in the first and second BZs, respectively.

Each of these linear cuts was integrated within $50\,\mathrm{meV}$ of E_F to produce momentum distribution curves (MDCs) shown in Fig. 4.15(d). On the node-surface, spectrum 2 shows a single clear peak representing the degeneracy of FS2/3. Off the node-surface, the MDCs for spectra 1 and 3 show that FS2 and FS3 separate and are no longer degenerate. Thus providing direct evidence for the band degeneracy between FS2/3 on the node-surface. As mentioned above, we expect SOC to split the FS2/3 crossing on the $k_y = 0$ plane of the node-surface. We note, however, that the SOC gap cannot be resolved because the peaks have a smaller calculated momentum separation than the fitted experimental widths. This result is further evidence for the minimal impact of SOC on the electronic structure of LaNiGa$_2$ in the normal state.

In the normal state and in the absence of SOC, the *Cmcm* space group makes LaNiGa$_2$ a *topological nodal line metal*. The line (or loop) is topological [259]. Nodal lines (lines or loops of degeneracies) in band structures have been found to be rather common [260, 261]. However, LaNiGa$_2$ is so far unique in having the nodal lines lie *precisely at the Fermi level*. However, this confluence of bands will occur in any nonsymmorphic metal with Fermi surfaces crossing the node-surface where bands are guaranteed to be orbitally degenerate.
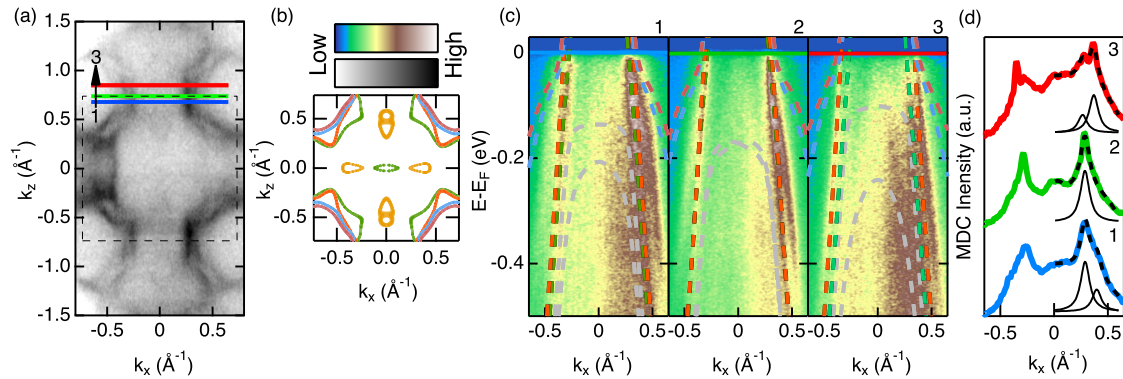
Figure 4.15: ARPES characterization of LaNiGa$_2$. (a) Constant energy map an integration window of ± 10 meV around E_F. The black line indicates the boundary of the BZ in the $k_y = 0$ plane. The colored curves within the BZ are the calculated FSs, with colors corresponding to 4.12(a). The blue, green, and red solid vertical lines indicate cuts (1), (2), and (3) in panel (b), respectively. (b) Energy vs momentum spectra along cuts indicated in (a). The dotted lines are the overlay of DFT calculations and the colors show which FSs are associated with each band. The grey bands are low energy bands which do not cross E_F. (c) MDCs at E_F from the cuts in panel (b). Spectra are fit to one (two) Lorentzian peaks (dotted black curve) for cuts 2 (1,3), with a Gaussian background centered on $k_x = 0$ (red). The black curves below the experimental data are the individual Lorentzian peaks marking where the bands cross E_F. The peak width for the Gaussian fit on 2 is a free fitting parameter and fixed width for cuts 1 and 3.

4.5   Pairing model and quasiparticles

Now we will examine the consequences of the *Cmcm* space group assignment for the superconducting state. LaNiGa$_2$ has low symmetry and previous symmetry analysis based on the D_{2h} point group revealed only 4 possible gap functions that break time-reversal symmetry [18, 19]. All of them have nodes inside the BZ, which is incompatible with thermodynamic measurements on polycrystals [14], as well as our heat capacity measurements on single crystals which indicate nodeless fully gapped superconductivity (Fig. 4.3(d)). The presence of nonsymmorphic symmetries modifies the nodal behavior on the $k_z = \pi/c$ plane

with or without SOC (see Supplementary Information in [223] for our classification), but does not provide a scenario for the absence of nodes inside the BZ. The five FSs in Fig. 4.12 indicate that the full FS is large and pervasive throughout the zone, thus any superconducting gap nodes in a direction $\hat{k}$ would produce a gap node on the FS and thus be detectable in thermodynamic measurements. This observation limits the possible superconducting states to A_{1g} with or without SOC, but these states do not break time-reversal symmetry. The superconducting properties of LaNiGa$_2$ cannot be understood without involving interband pairing [14, 232]. The topological properties of the normal state now provide a natural platform for such unconventional superconductivity.

As mentioned earlier, the Dirac lines and Dirac loop are gapped by SOC, *except* for the true-Dirac points surviving on the $Z - T$ line where SOC vanishes. A feature of more interest for the superconducting phase is that, unlike the case for conventional FSs, in Dirac (or Weyl) metals interband transitions persist all the way to zero energy. Any single band model breaks down, and a two-band model is a minimal model [262]. LaNiGa$_2$ thereby becomes an intrinsically two, degenerate and topological, band superconductor.

If the interband pairs are symmetric in the band index, then the Cooper-pair wave function will have the same symmetry as the intraband pairs do, s-wave will be spin-singlet and p-wave will be spin-triplet. But if the interband pairs are antisymmetric in the band index, we can have s-wave spin-triplet, or p-wave spin-singlet pairing while still satisfying the overall fermionic nature required for a superconducting order parameter [263]. If both symmetric and antisymmetric pairing exists simultaneously on the node surface (weak SOC) or on the true-Dirac points on the $Z - T$ line (strong SOC), time-reversal symmetry could be broken in two ways: the band (orbital) channel or the spin channel.

In the band-orbital channel, two gap functions (for example s-wave spin singlet A_{1g}^s

and s'-wave spin-triplet A_{1g}^t) could form a complex combination similar to $s + is'$ to break time-reversal symmetry. Another possibility is to combine several triplet components. For example, the B_{1g}^t triplet will be split by SOC into A_g, B_{2g}, and B_{3g}. The complex combination could also break time-reversal symmetry. However, a first order transition or multiple transitions are expected in these cases [14], but there is no such evidence in our heat-capacity measurements (Fig. 4.12(d) and Fig. 4.10). Time-reversal symmetry breaking in the band-orbital channel is therefore unlikely.

Because of the possibility of s-wave spin-triplet pairing on the Dirac lines, loop, or points, time-reversal symmetry could also be broken in the spin-channel from the INT state [232]. The power of symmetry analysis is remarkable in the sense that, even with the incorrect space group, the correct point group (D_{2h}) already led to the conclusion that the INT pairing is the only reasonable solution [14, 232]. However, the necessary degeneracy was not identified because of the wrong space group. An orbital-singlet equal-spin pairing has also been proposed for doped Dirac semimetals [264].

The INT model has also been proposed to explain time-reversal symmetry breaking and fully gapped superconductivity in LaNiC$_2$ [232, 265, 266]. While LaNiGa$_2$ and LaNiC$_2$ are compositionally related, our results on LaNiGa$_2$ highlight new significant differences between the two compounds. LaNiC$_2$ has a symmorphic and non-centrosymmetric space group ($Amm2$, #38), and thus far no topological band-crossing have been reported [265, 267–272]. In addition, electrical resistivity measurements under pressure showed the proximity to a different state characterized by a high-energy scale [273], and magnetic penetration-depth measurements under pressure suggested the proximity of a quantum critical point in LaNiC$_2$ [274]. Further studies remain needed on both materials to confirm the validity of the INT model, and the mechanism of time-reversal symmetry breaking. Our discovery of

symmetry imposed band crossing, even under SOC, in LaNiGa$_2$, reinforce the relevance of the INT model for this compound, as well as for other nonsymmorphic superconductors.

Breaking of time-reversal symmetry requires a nonunitary triplet pairing potential $\hat{\Delta} = i(\Delta_o \tilde{\eta} \cdot \tilde{\sigma})\sigma_y \otimes i\tau_y$ where the tensor products include the first (spin, σ matrices) channel $\sigma = \uparrow, \downarrow$ and the second (band, τ matrices) channel, with the bands labeled by $m = \pm$ being degenerate along the Dirac loops, taken to be at $k_\perp = 0$.

Note that the spontaneous vector field $\Delta_o \vec{\eta}$ couples to spin like a magnetic moment. The pairing matrix describes triplet pairing but is antisymmetric in the band channel $(i\tau_y)$ to ensure the fermionic antisymmetry of the pair wavefunction [14]. The experimentally observed time-reversal symmetry breaking is ensured by the nonunitarity, which is characterized by a nonvanishing real vector $\vec{\omega} = i(\vec{\eta} \times \vec{\eta}^*)$ which satisfies $|\vec{\omega}| \leq |\vec{\eta}|^2 = 1$. A noteworthy difference with previous INT proposals [14, 232] is that the true two-band situation in LaNiGa$_2$ is enforced by symmetry, and persists in the BdG quasiparticle bands. Accounting for the linear band coupling $\beta k_\perp$ away from the node-surface, the dispersion of the eight BdG quasiparticles (two bands, two spins, electrons and holes) becomes

$$\varepsilon_k = \pm\left[\sqrt{\{vk_\perp - \mu\}^2 + |\Delta_o|^2(1 \pm |\vec{\omega}|)} \pm \beta k_\perp\right] \tag{4.3}$$

with degenerate eigenvalues on the node-surface of $|\Delta_o|\sqrt{1 \pm |\vec{\omega}|}$.

The spectrum, shown in Fig. 4.16, illustrates the 8-band behavior versus the strength of nonunitarity. The nonsymmorphic operations guarantee that pairs of BdG quasiparticle bands persist in "sticking together" on both sides of the gap at $k_\perp = 0$, thereby retaining topological character. However, now massive points of degeneracy arise in the BdG band structure, unlike the bands of Ghosh *et al.* [232] which retain no degeneracies and hence no topological character. The linear band mixing results in the gap edges lying slightly away from
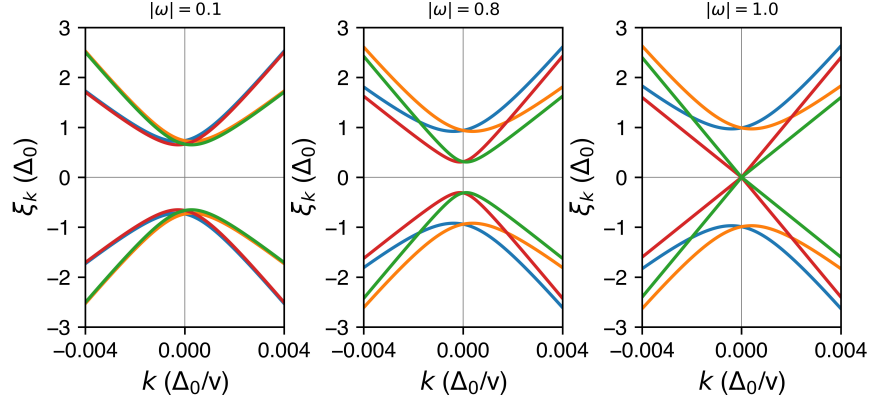
Figure 4.16: BdG quasiparticle bands near the Dirac point for three values of the $|\vec{\omega}| = 0.1, 0.8, 1.0$. Left to right: gapped, weakly nonunitary to the gapless fully nonunitary limit. Energy units correspond to $\Delta_o = 0.7\,\text{meV}$, $v = 500$ and $\beta = 100$, see Eq.4.3.

the plane $k_\perp = 0$. Unit values of $|\vec{\omega}|$ lead to gaplessness, with unusual Weyl dispersion of the BdG quasiparticles. The measured magnetic moment of $0.012\,\mu_B$, if from spin, corresponds to a small conventional band exchange splitting $\Delta_{ex} = m/N(E_F) = 1.8\,\text{meV}$. This splitting is comparable to (larger than) the superconducting gap $2\Delta_o \sim 3.5 - 4k_BT_c \sim 0.7\,\text{meV}$, suggesting it may be central to the exotic pairing mechanism.

In contrast to the INT state, conventional p-wave spin-triplet superconductivity is expected to lead to high upper critical fields, because equal spin-pairing is not subject to Pauli limiting, and because most proposed p-wave superconductors are heavy fermion systems with high orbital limit [55, 140, 142, 275–277]. LaNiGa$_2$, however, is not a heavy fermion material ($\gamma_n = 14.1\,\text{mJ mol}^{-1}\,\text{K}^{-2}$) and interband pairing is suppressed by the application of a strong magnetic field. Thus the upper-critical field in LaNiGa$_2$ remains low (see Fig. 4.11), even though time-reversal symmetry breaking superconductivity was observed at zero field in μSR experiments.

Our findings reveal that LaNiGa$_2$ is a topological nonsymmorphic crystalline superconductor [77, 79, 80, 278]. The normal state electronic structure features Dirac lines and Dirac

loop at the Fermi energy enforced by nonsymmorphic symmetries, as well as true-Dirac points that retain their degeneracy under SOC. These findings are expected to be common to a large number of materials with similar crystalline symmetries. In general, when topological materials become superconducting, the superconducting state is unconventional. LaNiGa$_2$ was previously reported as a time-reversal symmetry breaking superconductor with evidence for a fully gapped superconducting state, but the topological properties were unknown. The topological character now provides a natural platform for the INT state to exist. Further experiments and theoretical proposals are necessary to further elucidate the time-reversal symmetry breaking mechanism.

4.6 Outlook

As discussed in section 2.1.3, realizing topological superconductivity in candidate hosts is critical towards potentially discovering Majorana fermions within condensed matter systems. Also mentioned is that single-material TSCs are especially promising because they do not require special heterostructure engineering, they lack an overlapping magnetic ordering, and inducing superconductivity in known Dirac materials is difficult to predict. Our work on LaNiGa$_2$ now shows a predictive model towards discovering other single-material TSCs which break time-reversal symmetry.

Overall our work shows that nonsymmorphic symmetry operations are critical towards establishing a robust connection between the crystal structure, the topological properties, and the unconventional superconducting state. Therefore future work should focus on discovering other unconventional superconductors with similar properties or characterizing other nonsymmorphic topological metals for superconductivity [81–83]. To do this, one needs to first find focus on superconductors with nonsymmorphic unit cells. Since LaNiGa$_2$ was initially

thought to be a conventional BCS superconductor, it is important to include overlooked conventional superconductors with nonsymmorphic space groups.

This will yield an extremely lengthy list, so the candidates can be narrowed down by examining their electronic band structures. As highlighted above, the topological features of $LaNiGa_2$ are consequences of multiple bands crossing the node-surface. Therefore the focus should be on materials that contain multiple bands that cross a node-surface in their first BZ. Since there is currently not a definitive list of space groups that contain node-surfaces, immediate work should focus on materials that crystallize in space groups with known node-surfaces. Thus far some known examples include $P6_3mmc$ (No. 194) [236], $P\bar{4}2_13$ (No. 114) [279], and of course $Cmcm$. Although a deeper examination into the recent work done by Yu *et al.* could provide more space groups to examine [280].

An initial search for known superconductors with the same $Cmcm$ space group as $LaNiGa_2$ yields two promising candidates: $LaRhSi_2$ ($T_{sc} = 3.42\,\text{K}$) and $LaIrSi_2$ ($T_{sc} = 2.03\,\text{K}$) [281]. These materials should now be synthesized and fully characterized, including ZF-μSR and Kerr effect experiments to check if time-reversal symmetry is broken. Additionally, there are several other superconductors with different $Cmcm$ structure types that should also be examined such as $CaBi_2$ [282]. And lastly, as shown by UTe_2 [53], materials with the appropriate space group and electronic behavior but do not exhibit superconductivity down to $2\,\text{K}$, should be reexamined below that temperature threshold to see if low-temperature superconductivity exists.

4.7 LaNiGa$_2$ Appendix

4.7.1 Crystallography Tables

Tables 4.2 and 4.3 show the results from the SCXRD results on the LaNiGa$_2$ crystals.

4.7.2 Comparison with other potential intrinsic topological superconductors

Table 4.4 is a compiled list of potential intrinsic (single material) TSCs. We indicate whether the topological features are reported for bulk bands and/or for surface states, if Band-crossings (BC) are located at E_F, if time-reversal symmetry breaking (TRS) is broken (B) or preserved (P) upon entering the superconducting state or if a magnetic (M) state preceded the superconductivity, if the space group is centrosymmetric (CS) or non-centrosymmetric (NC). As can be seen, LaNiGa$_2$ is unique in that it is the only intrinsic TSC which breaks time-reversal symmetry in the superconducting state and has topological features at E_F without any overlapping magnetic state/fluctuations - antiferromagnetic (AFM) or ferromagnetic (FM). Additionally with our work, LaNiGa$_2$ is thus far the only material in this list to show experimental evidence for both broken time-reversal symmetry and topological features.

Identification code	JB10M4FMI (JF3040)
Empirical formula	Ga2 La Ni
Formula weight	$337.04\,\mathrm{g\,mol^{-1}}$
Temperature	$100(2)\,\mathrm{K}$
Wavelength	$0.71073\,\text{Å}$
Crystal system	Orthorhombic
Space group	Cmcm
Unit cell dimensions	a = $4.2818(14)\,\text{Å}$
	b = $17.468(6)\,\text{Å}$
	c = $4.2582(15)\,\text{Å}$
Volume	$318.48(19)\,\text{Å}^3$
Z	4
Density (calculated)	$7.030\,\mathrm{Mg/m^3}$
Absorption coefficient	$35.380\,\mathrm{mm^{-1}}$
F(000)	588
Crystal size	$0.159 \times 0.112 \times 0.081\ \mathrm{mm^3}$
Crystal color and habit	Silver Block
Diffractometer	Bruker Photon100 CMOS
Theta range for data collection	2.332 to 27.464°
Index ranges	$-5 \leq h \leq 5$, $-21 \leq k \leq 22$, $-5 \leq l \leq 5$
Reflections collected	1017
Independent reflections	234 [R(int) = 0.0216]
Observed reflections $(I > 2\sigma(I))$	232
Completeness to theta = 25.242°	100%
Absorption correction	Semi-empirical from equivalents
Max. and min. transmission	0.0326 and 0.0072
Solution method	SHELXT (Sheldrick, 2014)
Refinement method	SHELXL-2017/1 (Sheldric,2017)
	Full-matrix least-squares on F^2
Data / restraints / parameters	234 / 0 / 18
Goodness-of-fit on F^2	1.345
Final R indices $[I > 2\sigma(I)]$	$R_1 = 0.0222$, w$R_2 = 0.0620$
R indices (all data)	$R_1 = 0.0223$, w$R_2 = 0.0621$
Extinction coefficient	0.0025(4)
Largest diff. peak and hole	2.287 and -1.393 e. Å^{-3}

Table 4.2: Crystal data and structure refinement for LaNiGa$_2$.

Atom	Wyckoff Sites	x	y	z	U(eq)
La(1)	4c	1	0.3903(1)	0.75	15(1)
Ga(1)	4c	0.5	0.2495(1)	−0.25	19(1)
Ga(2)	4c	0.5	0.4593(1)	0.25	16(1)
Ni(1)	4c	0.5	0.3216(1)	0.25	16(1)

Table 4.3: Atomic coordinates and equivalent isotropic displacement parameters ($Å^2 x 10^3$) for LaNiGa$_2$. U(eq) is defined as one third of the trace of the orthogonalized U^{ij} tensor.

Table 4.4: Compiled list of intrinsic (single material) TSC materials. All properties are exhibited at ambient pressure. NP: nodal point, NL: nodal line. The highlighted red rows are materials with band-crossings at E_F, the orange rows show the U-based materials which have overlapping magnetic ordering/fluctuations and superconductivity, the blue rows show materials which breaks time-reversal symmetry, and the purple row shows LaNiGa$_2$ as the only material to date with broken time-reversal symmetry and band-crossings at E_F. †FeTe$_{1-x}$Se$_x$: recently reported to break time-reversal symmetry using a method other than μSR or Polar Kerr effect [283]. *K$_2$Cr$_3$As$_3$: possible very weak internal field (0.003 G) [284].

List of Single Material Topological Superconductors						
Material	Bulk or SSs?	at E_F?	TRS?	CS?	Refs.	Comments
LaNiGa$_2$	Bulk	✓	B	CS	[19]	
UPt$_3$	Both	✓	B	CS	[227, 278, 285–289]	AFM fluctuations
UCoGe, URhGe	Bulk	✓	M	CS	[54, 55, 290]	FM
URu$_2$Si$_2$	Bulk	×	M	CS	[291–294]	Hidden Order
UTe$_2$	-	-	B?	CS	[295–298]	FM-AFM fluctuations

137

List of Single Material Topological Superconductors						
Material	Bulk or SSs?	at E_F?	TRS?	CS?	Refs.	Comments
HfRuP	Bulk	✓	-	NC	[299]	NLs cross E_F
NbIr$_2$B$_2$,TaIr$_2$B$_2$	Bulk	✓	-	NC	[300]	NLs at E_F
NaAlSi	Bulk	✓	P	CS	[301, 302]	NLs cross E_F
TaOsSi	Bulk	✓	-	CS	[303]	NP at E_F
MgB$_2$	Bulk	✓	P	CS	[72, 304]	NL crosses E_F
CaSb$_2$	Bulk	✓	-	CS	[305, 306]	NLs cross E_F
SnTaS$_2$	Bulk	✓	-	CS	[307, 308]	NL crosses E_F
PbTaS$_2$	Bulk	×	-	CS	[309]	
Sr$_2$RuO$_4$	-	-	B	CS	[47, 227, 246, 310]	
Sr$_x$Bi$_2$Se$_3$	SS	×	B	CS	[230, 311]	
Cu$_x$Bi$_2$Se$_3$, Nb$_x$Bi$_2$Se$_3$	SS	×	- (P for Nb)	CS	[57, 312– 315]	
Tl$_x$Bi$_2$Te$_3$	SS	×	-	NC	[316]	
α-PdBi$_2$	SS	×	-	CS	[317]	

List of Single Material Topolcors Superconductors						
Material	Bulk or SSs?	at E_F?	TRS?	CS?	Refs.	Comments
α-BiPd	SS	$\times$	-	NC	[69, 318, 319]	
β-PdBi$_2$	SS	$\times$	P	CS	[67, 320]	
FeTe$_{1-x}$Se$_x$	SS	$\times$	P†	CS	[71, 321, 322]	
LiFeAs	Both	$\times$	P	NC	[321, 323]	
(Li$_{0.84}$Fe$_{0.16}$)OHFeSe	SS	$\times$	-	NC	[324]	
CaKFe$_4$As$_4$	SS	$\times$	-	CS	[325]	
In$_x$TaS$_2$, In$_x$TaSe$_2$	Bulk	$\times$	-	NC	[326, 327]	
Cu$_x$ZrTe$_{1.2}$	Bulk	$\times$	-	CS	[328]	
NiTe$_2$, PdTe$_2$	Both	$\times$	- (P for Pd)	CS	[329–333]	
PbTaSe$_2$	Both	$\times$	P	NC	[68, 334–337]	
NbC, TaC	Bulk	$\times$	P	CS	[338, 339]	
Mo$_2$C, W$_2$C	SS	$\times$	-	CS	[340]	
CaSn$_3$, BaSn$_3$	Bulk	$\times$	-	CS	[341, 342]	
YRuB$_2$, LuRuB$_2$	Bulk	$\times$	P	CS	[73, 343]	
YIn$_3$ (M=In,Pb,Tl)	SS (Both for Tl)	$\times$	-	CS	[344]	

						List of Single Material Topological Superconductors	
Material	Bulk or SSs?	at E_F?	TRS?	CS?	Refs.	Comments
$NbAl_3$	Bulk	×	-	CS	[345]	
$TaSe_3$	SS	×	-	CS	[346, 347]	
Ta_3Sb, Ta_3Sn	SS (Both for Sn)	×	-	CS	[348–350]	
Nb_3M (M=Al,Os,Au)	Bulk	×	-	CS	[350–352]	
LaNiSi, LaPtSi, LaNiGe	Bulk	×	P	NC	[353–355]	
$TlBiTe_2$	SS	×	-	CS	[356]	
Tl_5Te_3	SS	×	-	CS	[357]	
YPtBi, LuPtBi	SS	×	- (P for Y)	NC	[358–362]	other half-Heuslers
KV_3Sb_5, CsV_3Sb_5	Both	×	-	CS	[363–365]	
$Sn_{1-x}In_xTe$	SS	×	P	CS	[62, 366–369]	
$MoTe_2$	Bulk	×	-	NC	[370–373]	T_d phase
WS_2	SS	×	-	CS	[65]	2M phase.
$A_2Cr_3As_3$ (A=Na,K,Rb,Cs)	Bulk	×	- (P* for K)	NC	[284, 374]	
$ZrInPd_2, HfInPd_2$	Bulk	×	-	CS	[375]	

	List of Single Material Topological Superconductors					
Material	Bulk or SSs?	at E_F?	TRS?	CS?	Refs.	Comments
MM'$_2$Al (M=Zr,Hf; M'=Ni,Pd)	Bulk	$\times$	-	CS	[376]	
MPd$_2$Sn (M=Sc,Y,Lu)	Both	$\times$	- (P for Y)	CS	[376–378]	

Chapter 5

Separation of Kondo Lattice Coherence from Crystal Electric Field in CeIn$_3$ with Nd substitutions

This work was performed in collaboration with Rumika Miyawaki, Zach Brubaker, Peter Klavins, Rena Zieve, Tatsuma Matsuda, and Valentin Taufour. The manuscript is currently under review for publication. Copyright permission has been obtained and granted to use figures 5.1 and 5.2.

5.1   Background and Motivation

Explorations of heavy fermion phase diagrams through chemical substitution, hydrostatic pressure, and/or magnetic fields have revealed interesting low-temperature physics like superconductivity, quantum criticality, and non-Fermi liquid behavior [53, 55, 379, 380]. Furthermore, the phase diagrams of some Ce-based heavy fermion materials also reveal an

interplay between Kondo lattice coherence and crystal electric field (CEF) physics. Unfortunately, both phenomena result from the proximity of the Ce f-bands to the Fermi level and therefore make it quite difficult to conclusively discern the origin of one or both features in any particular system.

The CeMIn$_5$ (M = Co, Rh, Ir) family contains many examples of tunable ground states. In these cases the heavy fermion unconventional superconductivity or quantum criticality could result from the different energy scales of the heavy fermionic Kondo lattice coherence and CEF interactions. Inelastic neutron studies have found that these tetragonal materials have two clear and well separate CEF splittings [114]. $\rho_{mag}(T)$ measurements on CeMIn$_5$ samples only show evidence for a single maximum (Fig. 5.1(a) and (c)) [121–123]. Although it should be noted that in anisotropic $\rho(T)$ measurements, there does appear to be limited evidence for at least two separate $-ln(T)$ regions [131]. Either way the one clear $\rho_{mag}(T)$ maximum observed in these materials has been attributed to the Kondo lattice coherence [101, 103, 105, 128, 381].

Within other tetragonal materials with well separated Kondo lattice coherence and CEF resistivity features, it has been well established that the evolution of hydrostatic pressure can change the Kondo lattice coherence energy scale (k_BT_{coh}) [118, 119, 125, 130, 135, 382, 383]. In many of these cases k_BT_{coh} increases to converge with a CEF depopulation scattering maximum to form a single broad feature. Pressure studies on the CeMIn$_5$ have also shown that k_BT_{coh} and the associated maximum in $\rho_{mag}(T)$ can shift to higher temperatures (Fig 5.1(a) and (b)) [121, 131, 384, 385]. Yet there is no clear evidence that it is possible to separate the Kondo lattice coherence and CEF depopulation features through hydrostatic pressure. Another way to alter k_BT_{coh} in CeMIn$_5$ is by chemical substitution (Fig. 5.1(c)) [95, 103–105, 127, 128, 386–388].
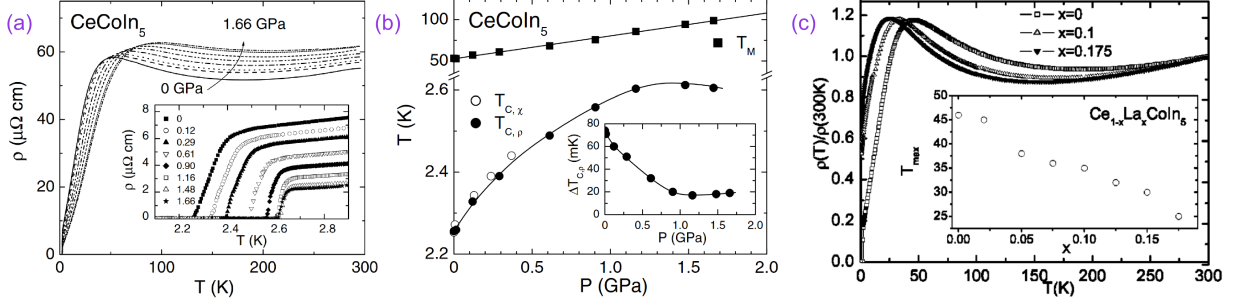
Figure 5.1: (a) $\rho(T)$ curves for CeCoIn$_5$ at various pressures. These curves show how the single maximum T_M and the superconducting transition T_C (inset) develop as a function of pressure. (b) The T-P phase diagram for CeCoIn$_5$ which shows T_M increasing and the dome shape of T_C as a function of pressure. Plots (a) and (b) were originally published in [384]. (c) Normalized $\rho(T)$ curves for La substituted CeCoIn$_5$. These curves show the single maximum $T_{\max}$ decreasing as a function La concentration. The inset shows the $T - x_{La}$ phase diagram for $T_{\max}$. Plot was originally published in [103].

In the base compound of the CeMIn$_5$ — CeIn$_3$ — $\rho_{mag}(T)$ experiments also reveal a single broad maximum, $T_{max} \sim 50\,\mathrm{K}$. However, this feature has been attributed to the combination of both the Kondo lattice coherence and the CEF depopulation effects [158, 165, 169, 389], wherein the Kondo lattice coherence is only achieved when the $4f$ electrons condense from a high energy Γ_8 quartet to the Γ_7 doublet ground-state ($\Delta_{\mathrm{CEF}} \sim 100 - 200\,\mathrm{K}$) [86, 87, 112, 390]. Similar to CeMIn$_5$, pressure and substitution studies on CeIn$_3$ have shown that this single maximum can be driven to higher (Fig. 2.14) [88, 89, 155, 158] and lower (Fig. 5.2) [165, 167, 170] temperatures, respectively. What remains constant throughout each of these experiments is that only a single resistivity maximum is observed for CeIn$_3$.

Here we report a thorough exploration of Ce$_{1-x}$Nd$_x$In$_3$ to reveal the separation of the Kondo lattice coherence and the CEF depopulation features. Similar to Nd substitutions in CeRhIn$_5$, we argue that the substituted Nd atoms act as Kondo holes and weaken $k_B T_{coh}$ [105]. However, in CeIn$_3$ this results in the Kondo lattice coherence maximum to

144
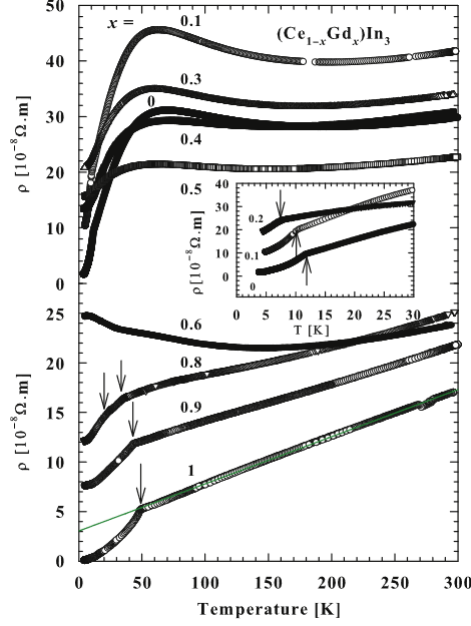
Figure 5.2: $\rho(T)$ curves for various concentrations of Gd substituted CeIn$_3$. From $x_{Gd} = 0 \to 0.5$ the maximum in $\rho(T)$ can be seen decreasing to lower temperatures as x_{Gd} increases. Plot was originally published in [170].

be driven to lower temperatures. This results in two distinct $-ln(T)$ regions, along with two broad humps, in $\rho_{mag}(T)$. Where the low- and high-temperature features stem from the weakened $k_B T_{coh}$ and the persistent CEF energy splitting (Δ_{CEF}), respectively. The Kondo lattice coherence of CeIn$_3$ also seems to follow percolation theory principles because the Nd concentration ($x = 0.65$) that suppresses the Kondo lattice coherence matches with the theoretical percolation limit of a simple 3D cubic system [172]. While a double maximum $\rho_{mag}(T)$ curve has been experimentally observed in other cubic Ce-based materials [106, 120], this is the first time the Kondo lattice coherence and CEF depopulation features have shown to separate in the well studied Ce$_m$M$_n$In$_{3m+2n}$ ($m = 1, 2; n = 0, 1$) family.

Previous reports have found that both CeIn$_3$ and NdIn$_3$ have AFM ordering transitions around 10.1 K and 5.9 K, respectively [86, 390–392]. The AFM ordering within CeIn$_3$ has

a propagation vector of $\mathbf{Q} = (\frac{1}{2}, \frac{1}{2}, \frac{1}{2})$ where the Ce atoms are ferromagnetically aligned in the (111) plane and anti-parallel amongst adjacent planes [86]. Investigations of the $NdIn_3$ magnetic ordering reveal a complex magnetic phase diagram with several different AFM structures. Upon the first AFM transition, the Nd moments align in an incommensurate structure. After two additional transitions a commensurate structure with a propagation vector of $\mathbf{Q} = (\frac{1}{2}, \frac{1}{2}, 0)$ stabilizes below 4.83 K [90]. It is also well established that the cubic crystal field of $CeIn_3$ splits the Ce $J = \frac{5}{2}$ into a ground-state Γ_7 doublet and Γ_8 quartet with a CEF splitting, Δ, of the order 120 K [86, 87, 112, 390]. As highlighted in section 2.2.5, $CeIn_3$ exhibits heavy fermion superconductivity when the AFM state is suppressed with hydrostatic pressure [89, 156–158] and strange magnetic behavior when exposed to large external magnetic fields [163] (Fig. 2.14).

Through powder X-ray diffraction (PXRD), energy-dispersive spectroscopy (EDS), magnetization, and electrical resistivity measurements we construct a comprehensive phase diagram, including two antiferromagnetic (AFM) regions. We also discuss the interactions between the two different AFM structures of $CeIn_3$ and $NdIn_3$. Lastly, in the low concentration region of Nd, $x \leq 0.4$ we show how the paramagnetic signal from the Nd^{3+} ions mask the small AFM signature in magnetic susceptibility measurements.

5.2 Results and Discussion

Phase identification for each PXRD pattern is shown in Fig. 5.3(a). Regardless of the nominal Nd concentration, x_{Nom}, each synthesis produces single crystals that fit to the cubic Cu_3Au structure. The PXRD patterns reveal nearly phase pure products with the only other phases consisting of trace amounts of In flux and the internal Si standard. Unit-cell parameter a, obtained from Pawley refinements, shows a smooth linear decrease as a function of x_{Nom},

146
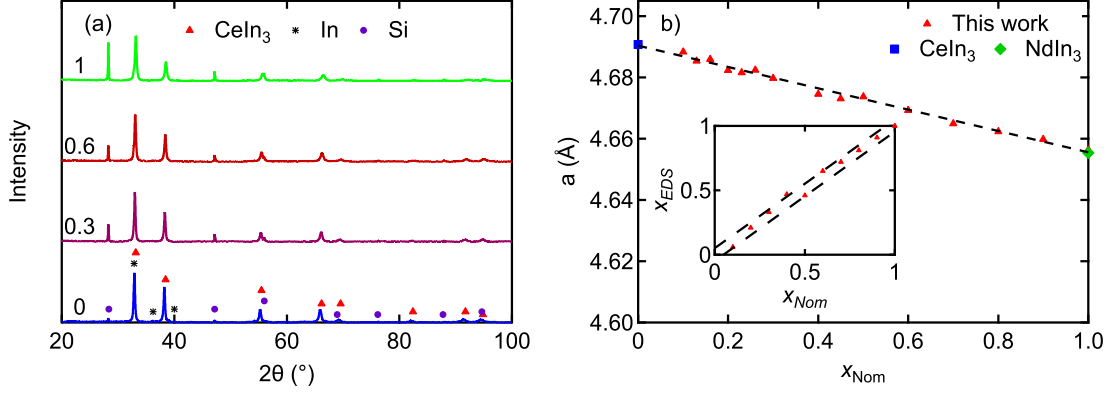
Figure 5.3: a) PXRD patterns for single crystals when $x_{Nom} = 0$, 0.3, 0.6, and 1. b) Cubic lattice parameter a as a function of x_{Nom} within the $Ce_{1-x}Nd_xIn_3$ series. The unit-cell parameter a for $CeIn_3$ and $NdIn_3$ are from [393] and [394], respectively. The inset shows the relationship between x_{Nom} and x_{EDS}. The two dotted lines are the $\pm 5\%$ error region.

in agreement with Vegard's law (Fig. 5.3(b)). This linear relationship indicates that the Nd and Ce atoms homogeneously incorporate into the parent structures at the ends of the substitution range.

Atomic compositions were also obtained from EDS spectra on selected crystals. The substitution percentages obtained from these measurements, x_{EDS}, show good agreement with x_{Nom} (inset of Fig. 5.3(b)). However, the two values can differ by up to about 5%, as shown by the dotted lines. Since x_{EDS} and x_{Nom} are in good agreement with one another, henceforth, all values of x_{Nd} will refer to x_{Nom}.

In Fig. 5.4(a) we present the temperature dependence of the normalized electrical resistivity, $\rho(T)/\rho(300K)$, for single crystals from representative batches of $Ce_{1-x}Nd_xIn_3$. As previously highlighted, the resistivity curve for $CeIn_3$ shows a maximum, $T_{max} \sim 50\,K$, which has been associated to the combination of the Kondo lattice coherence and the CEF depopulation effects [158, 165, 169, 389]. Tracking T_{max} across the $Ce_{1-x}Nd_xIn_3$ alloys, we find that this feature shifts slightly to lower temperatures with increasing Nd concentration (orange
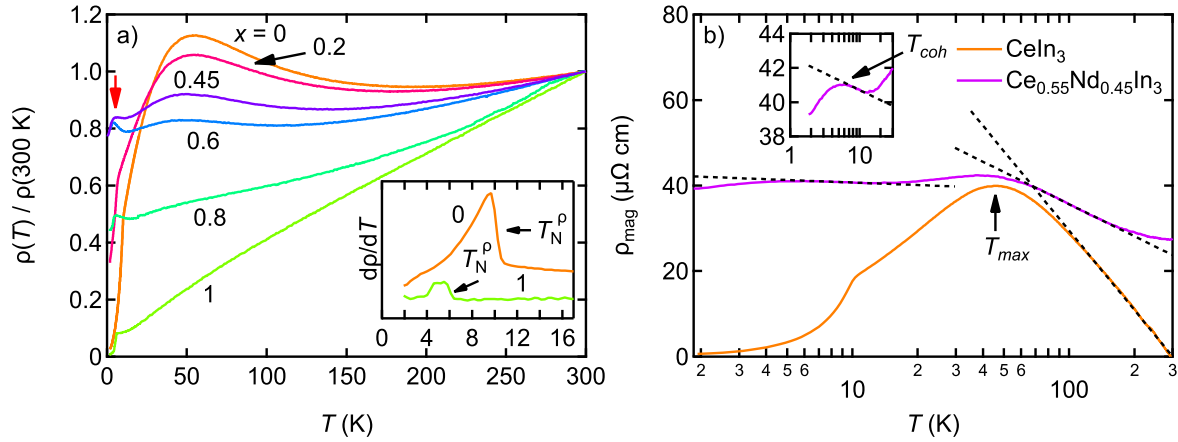
Figure 5.4: a) Normalized temperature dependence of $\rho(T)/\rho(300K)$ for representative single crystals of $Ce_{1-x}Nd_xIn_3$. The red arrow shows the low-temperature maximum T_{coh} for $x = 0.45$. The inset shows examples of the peak associated with the AFM transition in the first-derivative curve, $d\rho(T)/dT$, from $CeIn_3$ and $NdIn_3$. The arrows show the mid-point that was selected for T_N^ρ. b) $\rho_{mag}(T)$ for $CeIn_3$ and $Ce_{0.55}Nd_{0.45}In_3$. The log scale is used to show the regions with a $-ln(T)$ relationship (dashed black lines) indicating the CEF depopulation and/or the Kondo lattice coherence effects. The inset shows the zoomed-in low-temperature region for $Ce_{0.55}Nd_{0.45}In_3$ where the second maximum, T_{coh}, and $-ln(T)$ region are more easily observed.

crosses in Fig. 5.7). This is similar to other substitution studies on $CeIn_3$ [165, 166, 169, 170]. Nd substitution, however, differs because in the most disordered region, $x = 0.4 - 0.5$, a clear and distinct second maximum arises, T^* shown by the red arrow in Fig. 5.4(a), and then sharply drops in temperature.

This double maximum behavior can more easily be observed in Fig. 5.5, where $\rho(T)$ and $M(T)/H$ curves are shown for $x = 0.4 - 0.5$. Interestingly, we find that the low-temperature maximum (black arrows in Fig. 5.5) sharply decreases in temperature and seems to approach $0\,K$ near the theoretical percolation threshold for a simple 3D cubic system ($x = 0.65$) (solid black line in Fig. 5.7) [172]. Often an enhancement in resistivity is observed because of magnetic scattering, however Fig. 5.5 makes clear that the low-temperature maximum

148

$x = 0.4 - 0.5$ is distinct from the magnetic ordering (denoted by the purple vertical lines). By contrast, the maximum resistivity in the range $x = 0.6 - 0.8$ corresponds to a magnetic transition for the Nd ordering, which is shown in Fig. 5.5 for $x = 0.6$.

Fig. 5.4(b) shows $\rho_{mag}(T)$ for CeIn$_3$ and Ce$_{0.55}$Nd$_{0.45}$In$_3$ where the phonon scattering was subtracted out by their respective La analogues: LaIn$_3$ and La$_{0.55}$Nd$_{0.45}$In$_3$. By substituting Nd into the CeIn$_3$ structure, the high-temperature $-ln(T)$ relationship and T_{max} are preserved. While for the most disorder substitution concentrations (e.g. Ce$_{0.55}$Nd$_{0.45}$In$_3$) a second maximum, T^*, arises which also contains a temperature region with the $-ln(T)$ relationship (inset Fig. 5.4(b)). These $-ln(T)$ regions in $\rho_{mag}(T)$ are expected for both features [101, 102].

Here we argue that this double maximum occurs due to the separation of the Kondo lattice coherence and CEF depopulation features. More specifically the Nd ions act as Kondo holes and lower k_BT_{coh} [395, 396]. The Nd substitution drives the Kondo lattice coherence crossover of CeIn$_3$ to lower temperatures until this feature disjoins from the CeIn$_3$ CEF depopulation feature. Meanwhile the incoherent Kondo scattering from the CEF interaction operates at the local level on the Ce ions, so Δ_{CEF} is not expected to change much with varying the Ce concentration. Therefore, the persistent T_{max} remains associated with the CEF depopulation effect feature and the second maximum, $T^* = T_{coh}$, at lower temperature is attributed to the weakened Kondo lattice coherence. Overall this data shows that the Kondo lattice coherence and the CEF depopulation effects are independent and can be separated by Nd substitutions. In the parent compound CeIn$_3$, the overlap of the two features results from the accidental similarity of the two energy scales. Additionally, since T_{coh} is completely suppressed near the theoretical percolation limit for a simple 3D cubic system it then follows that the Kondo lattice coherence follows percolation theory principles.
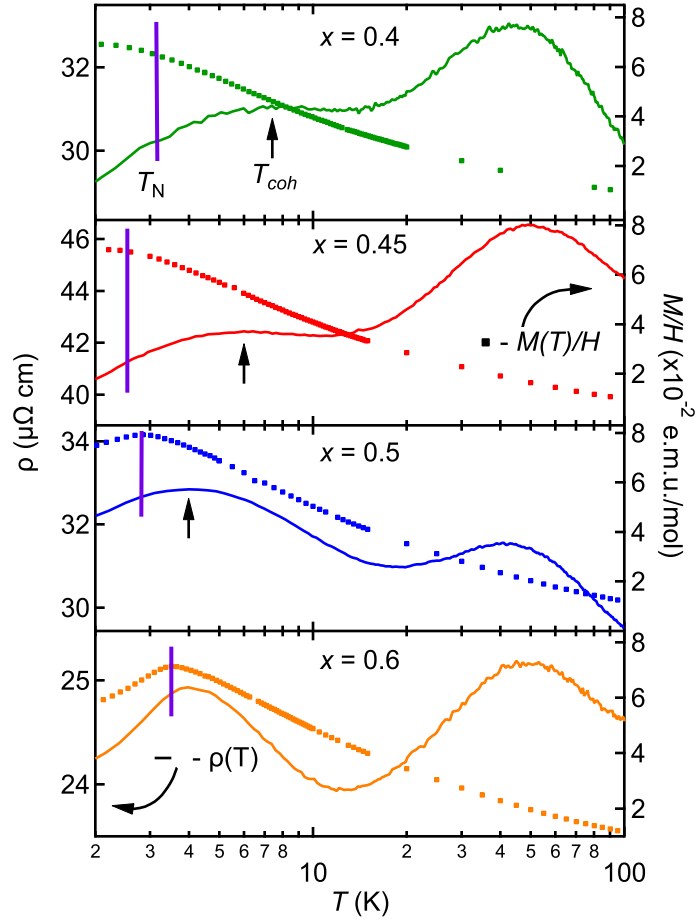
Figure 5.5: $\rho(T)$ (lines) and $M(T)/H$ (squares) for $x = 0.4$ (green), 0.45 (red), 0.5 (blue), and 0.6 (orange). The purple vertical lines show the location of the T_N from $\rho(T)$ data and the black arrows shows the location of T_{coh}.

In Fig. 2.11 we show different schematics of $\rho_{mag}(T)$ curves for Ce-based systems, with each schematic representing one of the possible scaling iterations between $k_B T_{coh}$ and Δ_{CEF}. Panels (c) and (d) show the difference between a cubic and tetragonal/hexagonal system when $k_B T_{coh} << \Delta_{CEF}$, respectively. If a system, like CeIn$_3$, has $\Delta_{CEF} \sim k_B T_{coh}$ then the $\rho_{mag}(T)$ curve has one maximum (label T_{max} in Fig. 2.11(b)). When $k_B T_{coh} << \Delta_{CEF}$ (like in CeAl$_2$ [106] or CeMg$_3$ [120]) then each Δ_{CEF} should be observed as a depopulation

150

maximum and the lowest temperature maximum can be associated with the Kondo lattice coherence (Fig. 2.11(c) and (d)). These curve shapes could also be achieved by lowering $k_B T_{coh}$ with chemical substitution. But this can only be achieved if the parent compound had $\Delta_{\mathrm{CEF}} \sim k_B T_{coh}$. However, if $k_B T_{coh} >> \Delta_{\mathrm{CEF}}$ then only one maximum is expected when the system undergoes a Kondo lattice coherence crossover (Fig. 2.11(a)). Given the similarities between the curves of Fig. 2.11(a) and (b) it is not possible to infer the relative nature of $k_B T_{coh}$ and Δ_{CEF} in a Ce-based compound from just a resistivity measurement on the parent compound. However, by performing chemical substitution it is possible to elucidate the relative nature of the two.

We can use tetragonal CeMIn$_5$ as an example. In all compounds amongst this family only one maximum is observed in $\rho(T)$ [121–123]. Based on our schematics this would then indicate that either $\Delta_{CEF,high}/\Delta_{CEF,low} << k_B T_{coh}$ or that $\Delta_{CEF,high} \sim k_B T_{coh}$. In the latter situation performing chemical substitution would weaken $k_B T_{coh}$ and eventually give rise to at least one additional well-separated maximum in $\rho_{mag}(T)$. Since this has not been observed in any Ce site chemical substitution study on these tetragonal systems it indicates that the former situation ($\Delta_{CEF,high}/\Delta_{CEF,low} << k_B T_{coh}$) is the most likely scenario [95, 103–105, 128, 388, 397]. Hence, as previously suggested, the single maximum in $\rho_{mag}(T)$ observed in CeMIn$_5$ can be attributed to the Kondo lattice coherence [101, 103, 105, 128]. It should be noted that this assessment does appear to be in conflict with the large Δ_2 values in these materials [114]. However, in many systems the Kondo exchange makes it such that $\Delta_{\mathrm{CEF}} \neq k_B T_{CEF}$. So it is also possible that in CeMIn$_5$ the Kondo exchange lowers T_{CEF} below T_{coh}.

Ultimately our work shows that it is possible to separate the Kondo lattice coherence and CEF features within the Ce$_m$M$_n$In$_{3m+2n}$ family. We highlight that a double maximum
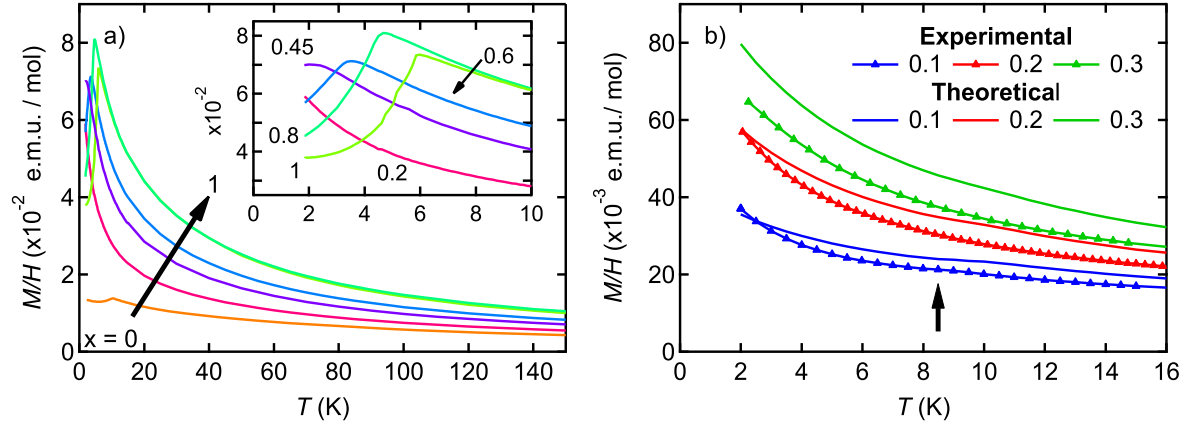
151

Figure 5.6: a) Temperature dependence of $M(T)/H$ from selected samples in the $Ce_{1-x}Nd_xIn_3$ series. These measurements were collected in a $\mu_0 H = 1\,T$ field. Given the cubic nature of structure, crystal orientation was not accounted for. Inset shows the low-temperature region of the susceptibility curves for $x_{Nd} = 0.2 - 1$. b) The experimental data for $x_{Nd} = 0.1, 0.2$, and 0.3 are shown by the lines with triangles. The solids lines represent the simulated data for the respective values of x_{Nd}. For these simulations, the calculated μ_{eff} for a Nd^{3+} of $3.62\,\mu_B$ and a Curie-Weiss constant of $\theta = -5\,K$ were employed to represent the Nd magnetic contributions. The arrow shows the slight kink where the Ce^{3+} AFM transition is experimentally observed from $Ce_{0.9}Nd_{0.1}In_3$.

feature has been observed in previous substitution studies on $CeIn_3$ and our work makes clear the underlying mechanism behind this unique feature [167, 169].

It should be noted that previous Kondo holes were strictly associated with nonmagnetic atoms [395, 396]. Although it is well established that Nd^{3+} ions produce magnetic materials, from a Kondo/CEF physics perspective these ions act more similar to their nonmagnetic counterparts, La^{3+}. This is due to the low-lying $4f$ Nd bands [398] and their inability to induce the Kondo effect with the conduction electrons. Similar arguments have been made about magnetic substitution studies on $CeMIn_5$ [105, 387, 399, 400].

Evidence for the AFM ordering transition is observed as a downward kink in the resistivity (inset Fig. 5.4(a)) and magnetic susceptibility, $M(T)/H$, curves (inset Fig. 5.6(a)). The

152
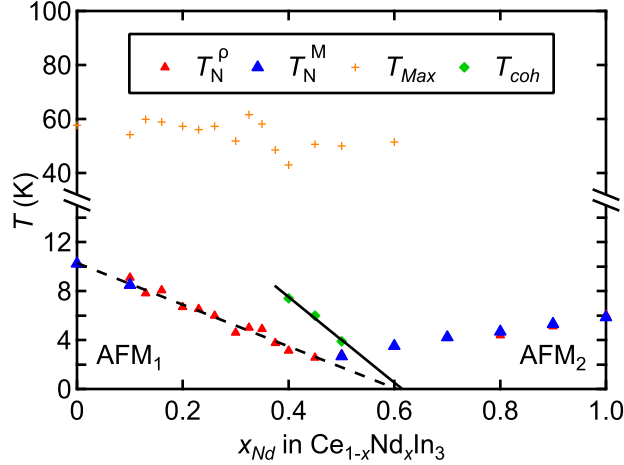
Figure 5.7: Observed features from $\rho(T)$ and $M(T)/H$ curves as a function of x_{Nd} for $Ce_{1-x}Nd_xIn_3$. The two AFM regions, AFM_1 and AFM_2, show the Nd concentrations where the $CeIn_3$ and $NdIn_3$ AFM structures, respectively, are dominant. The dotted black line is the linear fit of T_N^ρ and T_N^M for the $CeIn_3$ region when $x_{Nd} \leq 0.4$. The solid black line is the linear fit of the second maximum, T_{coh}, for $x = 0.4, 0.45$, and 0.5.

mid-point of the first-derivative peak, $d\rho/dT$, matches well with the magnetic susceptibility AFM transitions. For the two parent compounds, $CeIn_3$ and $NdIn_3$, the transitions, T_N^ρ and T_N^M, match the T_N^M temperatures from previous reports: $T_N^M = 10.2\,\mathrm{K}$ and $5.9\,\mathrm{K}$, respectively [86, 390–392].

Interestingly, unlike the magnetic data, $\rho(T)$ data shows evidence for a single T_N^ρ in the Nd dilute region, $x_{Nd} \leq 0.4$. This T_N^ρ is then suppressed to lower temperatures as a function of x_{Nd} until the transition temperature is reduced down to $\sim 2.5\,\mathrm{K}$ when $x_{Nd} = 0.45$. Above this concentration of Nd, both resistivity and magnetic susceptibility measurements reveal a clear single AFM transition which increases with x_{Nd}. Samples with low Nd substitution show no obvious AFM transitions in magnetization measurements. Rather samples within this region appear to have a large paramagnetic signal at low temperatures. The lone exception, when $x_{Nd} = 0.1$ there is a small kink around $8.5\,\mathrm{K}$, as denoted by the arrow in Fig. 5.6(b).

Similar magnetic susceptibility results — lack of AFM transition — were observed when Gd, Tb, and Dy were separately alloyed into CeIn$_3$ at low concentrations [170]. In the Ce-concentrated regions of these materials, however, electrical transport measurements also revealed the continued presence and suppression of the CeIn$_3$ AFM transition. The authors did not directly comment on this discrepancy in the Gd, Tb, and Dy alloys. However, when substituted with nonmagnetic La atoms, clear CeIn$_3$ AFM transitions are observed in magnetic susceptibility measurements with similar Ce concentrations in Ce$_{1-x}$La$_x$In$_3$ [167]. Therefore, to explain the absence of a visible AFM anomaly from our samples, we hypothesize that the large magnetic signal from paramagnetic Nd^{3+} ions dominates the smaller signal associated with the antiferromagnetic ordering of the CeIn$_3$ lattice.

To test this hypothesis we calculated theoretical curves by taking a weighted sum between the antiferromagnetically aligned CeIn$_3$ lattice (with the same T_N) and the paramagnetic Nd ions. These calculations require two key assumptions about these alloys: (1) the Ce moments aligned antiferromagnetically in accordance with the CeIn$_3$ lattice and (2) the Nd moments are too dilute to order magnetically and thus remain paramagnetic throughout the temperature region. Using the raw data of CeIn$_3$ and the theoretical μ_{eff} of Nd, a weighted sum was applied across the entire temperature range (Fig. 5.6(b)). When $x_{Nd} = 0.1$, both the simulated and experimental curves show a slight kink in the upward susceptibility curves, originating from the CeIn$_3$ AFM ordering. The simulated curves for $x_{Nd} = 0.2$ and 0.3 appear in reasonable agreement with the experimental data and show that the CeIn$_3$ AFM transitions are indiscernible. Therefore, across this region, $x_{Nd} \leq 0.4$, we conclude that the Nd ions do not participate in the magnetic ordering of CeIn$_3$ and remain paramagnetic, leading to the larger Nd paramagnetic signal masking the magnetic signature from the CeIn$_3$ AFM ordering.

154

The AFM transitions from the magnetic susceptibility and electrical transport measurements are combined with the resistivity features discussed above to create a comprehensive $T - x_{\mathrm{Nd}}$ phase diagram (Fig. 5.7). Instead of adopting the other's AFM structure, the CeIn$_3$ and NdIn$_3$ AFM orderings appear to be in competition with one another and each weakens the magnetic ordering of the other lattice. Similar to the La substituted system, there is a linear dependence of T_{N} with x_{Nd} in the Ce-concentrated region which extrapolates to give a critical concentration of $x_c \sim 0.6$ (dotted black line Fig. 5.7) [104]. Like the critical concentration for the Kondo lattice coherence, x_c is in good agreement for the percolation threshold, $x = 0.65$, for a simple cubic lattice [172]. However, the slight drop from $x_c = 0.65$ to 0.6 indicates that there could be an additional mechanism at play like magnetic frustration due to the different AFM structures of CeIn$_3$ and NdIn$_3$. This behavior was observed in the Nd-substituted CeRhIn$_5$ system [105].

5.3   Conclusions

We have shown that Nd can successfully substitute into the parent CeIn$_3$ compound via a self-flux technique with excess In. Our PXRD and EDS results reveal a direct relationship between the nominal and actual substitution concentrations as Nd homogenously incorporates into the structure until it becomes fully NdIn$_3$. Our electrical resistivity measurements reveal that as Nd incorporates into the CeIn$_3$ structure, the Kondo lattice coherence and CEF depopulation features disjoin to reveal double maximum curves with two distinct $-ln(T)$ regions. We argue that the high-temperature maximum results from CEF depopulation effect from the splitting Δ_{CEF} in CeIn$_3$ and in the most disordered region ($x = 0.4 - 0.5$) the Nd ions act as Kondo holes to weaken $k_{\mathrm{B}}T_{coh}$ and push the Kondo lattice coherence crossover to lower temperatures. It appears that the Kondo lattice coherence feature disappears near

the theoretical percolation limit for a simple 3D cubic system, which suggests that this Kondo lattice coherence abides by percolation theory principles. This is the first time the Kondo lattice coherence and CEF depopulation phenomena have been shown to separate for a material within the $Ce_mM_nIn_{3m+2n}$ ($m = 1, 2; n = 0, 1$) family. Magnetic and resistivity measurements also reveal that across the substitution values, there is an interesting competition between the magnetic orderings of the two parent structures $CeIn_3$ and $NdIn_3$. Rather than adopting the AFM structure of the end parent structures Ce and Nd ions act as free paramagnets, when in dilute concentrations. The comprehensive phase diagram reveals a $x_c \sim 0.6$ which is slightly lower than observed for non-magnetically substituted $CeIn_3$. Future neutron diffraction and pressure studies on $Ce_{1-x}Nd_xIn_3$ would be valuable to further understand the interplay between these two AFM orders.

Bibliography

[1] P. Goldstein, Computing power of apollo 11 & the tech behind it (2019).

[2] Critical materials strategy (2011), U.S. Department of Energy:https://www.energy.gov/node/349057 .

[3] B. Rohrig, Smartphones: Smart chemistry (2015).

[4] S. K. Ghosh, M. Smidman, T. Shang, J. F. Annett, A. D. Hillier, J. Quintanilla, and H. Yuan, Journal of Physics: Condensed Matter **33**, 033001 (2020).

[5] J. F. Annett, *Superconductivity, Superfluids, and Condensates*, 1st ed. (Oxford University Press, 2004).

[6] C. Kittel, *Introduction to solid state physics*, 8th ed. (Wiley, Hoboken, NJ, 2005).

[7] J. Bardeen, L. N. Cooper, and J. R. Schrieffer, Phys. Rev. **108**, 1175 (1957).

[8] A. Mackenzie and Y. Maeno, Physica B: Condensed Matter **280**, 148 (2000).

[9] M. Tinkham, *Introduction to Superconductivity: Second Edition*, Dover Books on Physics (Dover Publications, 2004).

[10] S. Yonezawa, Condensed Matter **4** (2018).

[11] M. Sigrist and K. Ueda, Rev. Mod. Phys. **63**, 239 (1991).

[12] F. Bouquet, Y. Wang, R. A. Fisher, D. G. Hinks, J. D. Jorgensen, A. Junod, and N. E. Phillips, EPL (Europhysics Letters) **56**, 856 (2001).

[13] V. G. Kogan, C. Martin, and R. Prozorov, Phys. Rev. B **80**, 014507 (2009).

[14] Z. F. Weng, J. L. Zhang, M. Smidman, T. Shang, J. Quintanilla, J. F. Annett, M. Nicklas, G. M. Pang, L. Jiao, W. B. Jiang, Y. Chen, F. Steglich, and H. Q. Yuan, Phys. Rev. Lett. **117**, 027001 (2016).

[15] A. J. Leggett, Rev. Mod. Phys. **47**, 331 (1975).

[16] P. W. Anderson, Phys. Rev. B **30**, 4000 (1984).

[17] K. Ueda and T. M. Rice, Phys. Rev. B **31**, 7114 (1985).

[18] J. F. Annett, Advances in Physics **39**, 83 (1990).

[19] A. D. Hillier, J. Quintanilla, B. Mazidian, J. F. Annett, and R. Cywinski, Phys. Rev. Lett. **109**, 097001 (2012).

[20] C. Bradley and A. Cracknell, *The Mathematical Theory of Symmetry in Solids : Representation Theory for Point Groups and Space Groups* (Oxford University Press, Incorporated, 2010).

[21] V. G. Yarzhemsky and E. N. Muravev, Journal of Physics: Condensed Matter **4**, 3525 (1992).

[22] M. R. Norman, Phys. Rev. B **52**, 15093 (1995).

[23] V. G. Yarzhemsky, physica status solidi (b) **209**, 101 (1998).

[24] V. G. Yarzhemsky, International Journal of Quantum Chemistry **80**, 133 (2000).

[25] V. G. Yarzhemsky and V. I. Nefedov, International Journal of Quantum Chemistry **100**, 519 (2004).

[26] V. G. Yarzhemsky and V. I. Nefedov, Physics of the Solid State **51**, 448 (2009).

[27] T. Micklitz and M. R. Norman, Phys. Rev. B **80**, 100506 (2009).

[28] T. Micklitz and M. R. Norman, Phys. Rev. B **95**, 024508 (2017).

[29] T. Micklitz and M. R. Norman, Phys. Rev. Lett. **118**, 207001 (2017).

[30] T. Nomoto and H. Ikeda, Journal of the Physical Society of Japan **86**, 023703 (2017).

[31] S. Sumita and Y. Yanase, Phys. Rev. B **97**, 134512 (2018).

[32] S. Kobayashi, S. Sumita, Y. Yanase, and M. Sato, Phys. Rev. B **97**, 180504 (2018).

[33] S. Sumita, T. Nomoto, K. Shiozaki, and Y. Yanase, Phys. Rev. B **99**, 134513 (2019).

[34] B. A. Bernevig, T. L. Hughes, and S.-C. Zhang, Science **314**, 1757 (2006).

[35] C. L. Kane and E. J. Mele, Phys. Rev. Lett. **95**, 226801 (2005).

[36] M. König, S. Wiedmann, C. Brüne, A. Roth, H. Buhmann, L. W. Molenkamp, X.-L. Qi, and S.-C. Zhang, Science **318**, 766 (2007).

[37] Y. L. Chen, J. G. Analytis, J.-H. Chu, Z. K. Liu, S.-K. Mo, X. L. Qi, H. J. Zhang, D. H. Lu, X. Dai, Z. Fang, S. C. Zhang, I. R. Fisher, Z. Hussain, and Z.-X. Shen, Science **325**, 178 (2009).

[38] Y. Xia, D. Qian, D. Hsieh, L. Wray, A. Pal, H. Lin, A. Bansil, D. Grauer, Y. S. Hor, R. J. Cava, and M. Z. Hasan, Nature Physics **5**, 398 (2009).

[39] A. P. Schnyder, S. Ryu, A. Furusaki, and A. W. W. Ludwig, Phys. Rev. B **78**, 195125 (2008).

[40] A. Kitaev, AIP Conference Proceedings **1134**, 22 (2009).

[41] J. Alicea, Reports on Progress in Physics **75**, 076501 (2012).

[42] C. Beenakker, Annual Review of Condensed Matter Physics **4**, 113 (2013).

[43] M. Sato and S. Fujimoto, Journal of the Physical Society of Japan **85**, 072001 (2016).

[44] C. Nayak, S. H. Simon, A. Stern, M. Freedman, and S. Das Sarma, Rev. Mod. Phys. **80**, 1083 (2008).

[45] M. Leijnse and K. Flensberg, Semiconductor Science and Technology **27**, 124003 (2012).

[46] X.-L. Qi and S.-C. Zhang, Rev. Mod. Phys. **83**, 1057 (2011).

[47] M. Sato and Y. Ando, Reports on Progress in Physics **80**, 076501 (2017).

[48] L. Fu and C. L. Kane, Phys. Rev. Lett. **100**, 096407 (2008).

[49] Y. Li and Z.-A. Xu, Advanced Quantum Technologies **2**, 1800112 (2019).

[50] Y. Tsutsumi, M. Ishikawa, T. Kawakami, T. Mizushima, M. Sato, M. Ichioka, and K. Machida, Journal of the Physical Society of Japan **82**, 113707 (2013).

[51] A. K. C. Cheung and S. Raghu, Phys. Rev. B **93**, 134516 (2016).

[52] S. Kobayashi, Y. Yanase, and M. Sato, Phys. Rev. B **94**, 134512 (2016).

[53] S. Ran, C. Eckberg, Q.-P. Ding, Y. Furukawa, T. Metz, S. R. Saha, I.-L. Liu, M. Zic, H. Kim, J. Paglione, and N. P. Butch, Science **365**, 684 (2019).

[54] A. Daido, T. Yoshida, and Y. Yanase, Phys. Rev. Lett. **122**, 227001 (2019).

[55] D. Aoki, K. Ishida, and J. Flouquet, Journal of the Physical Society of Japan **88**, 022001 (2019).

159

[56] L. Fu and E. Berg, Phys. Rev. Lett. **105**, 097001 (2010).

[57] L. A. Wray, S.-Y. Xu, Y. Xia, Y. S. Hor, D. Qian, A. V. Fedorov, H. Lin, A. Bansil, R. J. Cava, and M. Z. Hasan, Nature Physics **6**, 855 (2010).

[58] Y. S. Hor, A. J. Williams, J. G. Checkelsky, P. Roushan, J. Seo, Q. Xu, H. W. Zandbergen, A. Yazdani, N. P. Ong, and R. J. Cava, Phys. Rev. Lett. **104**, 057001 (2010).

[59] S. Sasaki, M. Kriener, K. Segawa, K. Yada, Y. Tanaka, M. Sato, and Y. Ando, Phys. Rev. Lett. **107**, 217001 (2011).

[60] J. L. Zhang, S. J. Zhang, H. M. Weng, W. Zhang, L. X. Yang, Q. Q. Liu, S. M. Feng, X. C. Wang, R. C. Yu, L. Z. Cao, L. Wang, W. G. Yang, H. Z. Liu, W. Y. Zhao, S. C. Zhang, X. Dai, Z. Fang, and C. Q. Jin, Proceedings of the National Academy of Sciences **108**, 24 (2011).

[61] T. V. Bay, T. Naka, Y. K. Huang, H. Luigjes, M. S. Golden, and A. de Visser, Phys. Rev. Lett. **108**, 057001 (2012).

[62] T. Sato, Y. Tanaka, K. Nakayama, S. Souma, T. Takahashi, S. Sasaki, Z. Ren, A. A. Taskin, K. Segawa, and Y. Ando, Phys. Rev. Lett. **110**, 206804 (2013).

[63] L. Zhao, H. Deng, I. Korzhovska, M. Begliarbekov, Z. Chen, E. Andrade, E. Rosenthal, A. Pasupathy, V. Oganesyan, and L. Krusin-Elbaum, Nature Communications **6**, 8279 (2015).

[64] G. Du, J. Shao, X. Yang, Z. Du, D. Fang, J. Wang, K. Ran, J. Wen, C. Zhang, H. Yang, Y. Zhang, and H.-H. Wen, Nature Communications **8**, 14466 (2017).

[65] Y. Fang, J. Pan, D. Zhang, D. Wang, H. T. Hirose, T. Terashima, S. Uji, Y. Yuan, W. Li, Z. Tian, J. Xue, Y. Ma, W. Zhao, Q. Xue, G. Mu, H. Zhang, and F. Huang, Advanced Materials **31**, 1901942 (2019).

[66] N. Hao and J. Hu, Phys. Rev. X **4**, 031053 (2014).

[67] M. Sakano, K. Okawa, M. Kanou, H. Sanjo, T. Okuda, T. Sasagawa, and K. Ishizaka, Nature Communications **6**, 8595 (2015).

[68] S.-Y. Guan, P.-J. Chen, M.-W. Chu, R. Sankar, F. Chou, H.-T. Jeng, C.-S. Chang, and T.-M. Chuang, Science Advances **2** (2016).

[69] M. Neupane, N. Alidoust, M. M. Hosen, J.-X. Zhu, K. Dimitri, S.-Y. Xu, N. Dhakal, R. Sankar, I. Belopolski, D. S. Sanchez, T.-R. Chang, H.-T. Jeng, K. Miyamoto, T. Okuda, H. Lin, A. Bansil, D. Kaczorowski, F. Chou, M. Z. Hasan, and T. Durakiewicz, Nature Communications **7**, 13315 (2016).

160

[70] Z. F. Wang, H. Zhang, D. Liu, C. Liu, C. Tang, C. Song, Y. Zhong, J. Peng, F. Li, C. Nie, L. Wang, X. J. Zhou, X. Ma, Q. K. Xue, and F. Liu, Nature Materials **15**, 968 (2016).

[71] P. Zhang, K. Yaji, T. Hashimoto, Y. Ota, T. Kondo, K. Okazaki, Z. Wang, J. Wen, G. D. Gu, H. Ding, and S. Shin, Science **360**, 182 (2018).

[72] K.-H. Jin, H. Huang, J.-W. Mei, Z. Liu, L.-K. Lim, and F. Liu, npj Computational Materials **5**, 57 (2019).

[73] Y. Gao, P.-J. Guo, K. Liu, and Z.-Y. Lu, Phys. Rev. B **102**, 115137 (2020).

[74] Y. Ueno, A. Yamakage, Y. Tanaka, and M. Sato, Phys. Rev. Lett. **111**, 087002 (2013).

[75] K. Shiozaki and M. Sato, Phys. Rev. B **90**, 165114 (2014).

[76] S. A. Yang, H. Pan, and F. Zhang, Phys. Rev. Lett. **113**, 046401 (2014).

[77] D. Varjas, F. de Juan, and Y.-M. Lu, Phys. Rev. B **92**, 195116 (2015).

[78] K. Shiozaki, M. Sato, and K. Gomi, Phys. Rev. B **91**, 155120 (2015).

[79] Q.-Z. Wang and C.-X. Liu, Phys. Rev. B **93**, 020505 (2016).

[80] K. Shiozaki, M. Sato, and K. Gomi, Phys. Rev. B **93**, 195413 (2016).

[81] F. Tang, H. C. Po, A. Vishwanath, and X. Wan, Nature **566**, 486 (2019).

[82] M. G. Vergniory, L. Elcoro, C. Felser, N. Regnault, B. A. Bernevig, and Z. Wang, Nature **566**, 480 (2019).

[83] T. Zhang, Y. Jiang, Z. Song, H. Huang, Y. He, Z. Fang, H. Weng, and C. Fang, Nature **566**, 475 (2019).

[84] S. Blundell, *Magnetism in Condensed Matter*, Oxford Master Series in Condensed Matter Physics (OUP Oxford, 2001).

[85] V. Pecharsky and P. Zavalij, *Fundamentals of Powder Diffraction and Structural Characterization of Materials* (Springer, 2003).

[86] A. Benoit, J. Boucherle, P. Convert, J. Flouquet, J. Palleau, and J. Schweizer, Solid State Communications **34**, 293 (1980).

[87] J. M. Lawrence and S. M. Shapiro, Phys. Rev. B **22**, 4379 (1980).

[88] P. Morin, C. Vettier, J. Flouquet, M. Konczykowski, Y. Lassailly, J. M. Mignot, and U. Welp, Journal of Low Temperature Physics **70**, 377 (1988).

[89] F. M. Grosche, I. R. Walker, S. R. Julian, N. D. Mathur, D. M. Freye, M. J. Steiner, and G. G. Lonzarich, Journal of Physics: Condensed Matter **13**, 2845 (2001).

[90] M. Amara, R. Galéra, P. Morin, J. Voiron, and P. Burlet, Journal of Magnetism and Magnetic Materials **140-144**, 1157 (1995).

[91] M. A. Ruderman and C. Kittel, Phys. Rev. **96**, 99 (1954).

[92] T. Kasuya, Progress of Theoretical Physics **16**, 45 (1956).

[93] K. Yosida, Phys. Rev. **106**, 893 (1957).

[94] J. Kondo, Progress of Theoretical Physics **32**, 37 (1964).

[95] S. Nakatsuji, S. Yeo, L. Balicas, Z. Fisk, P. Schlottmann, P. G. Pagliuso, N. O. Moreno, J. L. Sarrao, and J. D. Thompson, Phys. Rev. Lett. **89**, 106402 (2002).

[96] K. Satoh, T. Fujita, Y. Maeno, Y. Ōnuki, and T. Komatsubara, Journal of the Physical Society of Japan **58**, 1012 (1989).

[97] A. Sumiyama, Y. Oda, H. Nagano, Y. Ōnuki, K. Shibutani, and T. Komatsubara, Journal of the Physical Society of Japan **55**, 1294 (1986).

[98] K. G. Wilson, Rev. Mod. Phys. **47**, 773 (1975).

[99] P. Nozières, Journal of Low Temperature Physics **17**, 31 (1974).

[100] P. Schlottmann, Physics Reports **181**, 1 (1989).

[101] S. Jang, J. D. Denlinger, J. W. Allen, V. S. Zapf, M. B. Maple, J. N. Kim, B. G. Jang, and J. H. Shim, Proceedings of the National Academy of Sciences **117**, 23467 (2020).

[102] B. Cornut and B. Coqblin, Phys. Rev. B **5**, 4541 (1972).

[103] C. Petrovic, S. L. Bud'ko, V. G. Kogan, and P. C. Canfield, Physical Review B **66**, 5 (2002).

[104] P. G. Pagliuso, N. O. Moreno, N. J. Curro, J. D. Thompson, M. F. Hundley, J. L. Sarrao, Z. Fisk, A. D. Christianson, A. H. Lacerda, B. E. Light, and A. L. Cornelius, Phys. Rev. B **66**, 054433 (2002).

[105] P. F. S. Rosa, A. Oostra, J. D. Thompson, P. G. Pagliuso, and Z. Fisk, Phys. Rev. B **94**, 045101 (2016).

162

[106] Y. Ōnuki, Y. Furukawa, and T. Komatsubara, Journal of the Physical Society of Japan **53**, 2734 (1984).

[107] N. Sato, A. Sumiyama, S. Kunii, H. Nagano, and T. Kasuya, Journal of the Physical Society of Japan **54**, 1923 (1985).

[108] Y. Ōnuki and T. Komatsubara, Journal of Magnetism and Magnetic Materials **63-64**, 281 (1987).

[109] V. Taufour, H. Hodovanets, S. K. Kim, S. L. Bud'ko, and P. C. Canfield, Phys. Rev. B **88**, 195114 (2013).

[110] Crystal field theory (2021), Chem LibreTexts:https://chem.libretexts.org/@go/page/529 .

[111] V. Nikiforov, Y. Koksharov, A. Gribanov, M. Baran, and V. Irkhin, Journal of Magnetism and Magnetic Materials **383**, 215 (2015).

[112] W. Knafo, S. Raymond, B. Fåk, G. Lapertot, P. C. Canfield, and J. Flouquet, Journal of Physics: Condensed Matter **15**, 3741 (2003).

[113] P. Morin, J. Rouchy, Y. Miyako, and T. Nishioka, Journal of Magnetism and Magnetic Materials **76-77**, 319 (1988).

[114] A. D. Christianson, E. D. Bauer, J. M. Lawrence, P. S. Riseborough, N. O. Moreno, P. G. Pagliuso, J. L. Sarrao, J. D. Thompson, E. A. Goremychkin, F. R. Trouw, M. P. Hehlen, and R. J. McQueeney, Phys. Rev. B **70**, 134505 (2004).

[115] M. Nicolas-Francillon, A. Percheron, J. Achard, O. Gorochov, B. Cornut, D. Jerome, and B. Coqblin, Solid State Communications **11**, 845 (1972).

[116] A. Percheron, J. Achard, O. Gorochov, B. Cornut, D. Jérome, and B. Coqblin, Solid State Communications **12**, 1289 (1973).

[117] P. Link and D. Jaccard, Physica B: Condensed Matter **230-232**, 31 (1997).

[118] Y. Kawamura, T. Nishioka, H. Kato, M. Matsumura, K. Matsubayashi, and Y. Uwatoko, Journal of Physics: Conference Series **200**, 012082 (2010).

[119] Z. Ren, L. V. Pourovskii, G. Giriat, G. Lapertot, A. Georges, and D. Jaccard, Phys. Rev. X **4**, 031055 (2014).

[120] P. K. Das, N. Kumar, R. Kulkarni, and A. Thamizhavel, Phys. Rev. B **83**, 134416 (2011).

[121] H. Hegger, C. Petrovic, E. G. Moshopoulou, M. F. Hundley, J. L. Sarrao, Z. Fisk, and J. D. Thompson, Phys. Rev. Lett. **84**, 4986 (2000).

[122] C. Petrovic, P. G. Pagliuso, M. F. Hundley, R. Movshovich, J. L. Sarrao, J. D. Thompson, Z. Fisk, and P. Monthoux, Journal of Physics: Condensed Matter **13**, L337 (2001).

[123] C. Petrovic, R. Movshovich, M. Jaime, P. G. Pagliuso, M. F. Hundley, J. L. Sarrao, Z. Fisk, and J. D. Thompson, Europhysics Letters (EPL) **53**, 354 (2001).

[124] G. Knebel, C. Eggert, D. Engelmann, R. Viana, A. Krimmel, M. Dressel, and A. Loidl, Phys. Rev. B **53**, 11586 (1996).

[125] E. Vargoz and D. Jaccard, Journal of Magnetism and Magnetic Materials **177-181**, 294 (1998).

[126] H. Wilhelm and D. Jaccard, Phys. Rev. B **66**, 064428 (2002).

[127] E. D. Bauer, F. Ronning, C. Capan, M. J. Graf, D. Vandervelde, H. Q. Yuan, M. B. Salamon, D. J. Mixson, N. O. Moreno, S. R. Brown, J. D. Thompson, R. Movshovich, M. F. Hundley, J. L. Sarrao, P. G. Pagliuso, and S. M. Kauzlarich, Phys. Rev. B **73**, 245109 (2006).

[128] J. Paglione, T. A. Sayles, P.-C. Ho, J. R. Jeffries, and M. B. Maple, Nature Physics **3**, 703 (2007).

[129] H. Hidaka, S. M. Ramos, E. N. Hering, M. B. Fontes, E. B. Saitovitch, S. Otani, T. Wakabayashi, Y. Shimizu, T. Yanagisawa, and H. Amitsuka, Journal of Physics: Conference Series **391**, 012019 (2012).

[130] Y. Hayashi, S. Takai, T. Matsumura, H. Tanida, M. Sera, K. Matsubayashi, Y. Uwatoko, and A. Ochiai, Journal of the Physical Society of Japan **85**, 034704 (2016).

[131] Z. Ren, G. W. Scheerer, D. Aoki, K. Miyake, S. Watanabe, and D. Jaccard, Phys. Rev. B **96**, 184524 (2017).

[132] V. Taufour, U. S. Kaluarachchi, S. L. Bud'ko, and P. C. Canfield, Physica B: Condensed Matter **536**, 483 (2018).

[133] Phase diagram for water (2021), Chem LibreTexts:https://chem.libretexts.org/@go/page/53818 .

[134] F. Steglich, J. Aarts, C. D. Bredl, W. Lieke, D. Meschede, W. Franz, and H. Schäfer, Phys. Rev. Lett. **43**, 1892 (1979).

[135] D. Jaccard, K. Behnia, and J. Sierro, Physics Letters A **163**, 475 (1992).

[136] R. Movshovich, T. Graf, D. Mandrus, J. D. Thompson, J. L. Smith, and Z. Fisk, Phys. Rev. B **53**, 8241 (1996).

[137] S. S. Saxena, P. Agarwal, K. Ahilan, F. M. Grosche, R. K. W. Haselwimmer, M. J. Steiner, E. Pugh, I. R. Walker, S. R. Julian, P. Monthoux, G. G. Lonzarich, A. Huxley, I. Sheikin, D. Braithwaite, and J. Flouquet, Nature **406**, 587 (2000).

[138] D. Aoki, A. Huxley, E. Ressouche, D. Braithwaite, J. Flouquet, J.-P. Brison, E. Lhotel, and C. Paulsen, Nature **413**, 613 (2001).

[139] N. T. Huy, A. Gasparini, D. E. de Nijs, Y. Huang, J. C. P. Klaasse, T. Gortenmulder, A. de Visser, A. Hamann, T. Görlach, and H. v. Löhneysen, Phys. Rev. Lett. **99**, 067006 (2007).

[140] I. Sheikin, A. Huxley, D. Braithwaite, J. P. Brison, S. Watanabe, K. Miyake, and J. Flouquet, Phys. Rev. B **64**, 220503 (2001).

[141] F. Lévy, I. Sheikin, B. Grenier, and A. D. Huxley, Science **309**, 1343 (2005).

[142] D. Aoki, T. D. Matsuda, V. Taufour, E. Hassinger, G. Knebel, and J. Flouquet, Journal of the Physical Society of Japan **78**, 113709 (2009).

[143] S. Ran, I.-L. Liu, Y. S. Eo, D. J. Campbell, P. M. Neves, W. T. Fuhrman, S. R. Saha, C. Eckberg, H. Kim, D. Graf, F. Balakirev, J. Singleton, J. Paglione, and N. P. Butch, Nature Physics **15**, 1250 (2019).

[144] V. Taufour, D. Aoki, G. Knebel, and J. Flouquet, Phys. Rev. Lett. **105**, 217201 (2010).

[145] H. Kotegawa, V. Taufour, D. Aoki, G. Knebel, and J. Flouquet, Journal of the Physical Society of Japan **80**, 083703 (2011).

[146] V. Taufour, A. Villaume, D. Aoki, G. Knebel, and J. Flouquet, Journal of Physics: Conference Series **273**, 012017 (2011).

[147] V. Taufour, U. S. Kaluarachchi, R. Khasanov, M. C. Nguyen, Z. Guguchia, P. K. Biswas, P. Bonfà, R. De Renzi, X. Lin, S. K. Kim, E. D. Mun, H. Kim, Y. Furukawa, C.-Z. Wang, K.-M. Ho, S. L. Bud'ko, and P. C. Canfield, Phys. Rev. Lett. **117**, 037207 (2016).

[148] U. S. Kaluarachchi, S. L. Bud'ko, P. C. Canfield, and V. Taufour, Nature Communications **8**, 546 (2017).

[149] H. von Löhneysen, Journal of Physics: Condensed Matter **8**, 9689 (1996).

[150] K. Heuser, E.-W. Scheidt, T. Schreiner, and G. R. Stewart, Phys. Rev. B **57**, R4198 (1998).

[151] G. R. Stewart, Rev. Mod. Phys. **73**, 797 (2001).

[152] S. Kasahara, T. Shibauchi, K. Hashimoto, K. Ikada, S. Tonegawa, R. Okazaki, H. Shishido, H. Ikeda, H. Takeya, K. Hirata, T. Terashima, and Y. Matsuda, Phys. Rev. B **81**, 184519 (2010).

[153] H. v. Löhneysen, A. Rosch, M. Vojta, and P. Wölfle, Rev. Mod. Phys. **79**, 1015 (2007).

[154] Q. Si, physica status solidi (b) **247**, 476 (2010).

[155] T. Kagayama and G. Oomi, Japanese Journal of Applied Physics **32**, 318 (1993).

[156] I. Walker, F. Grosche, D. Freye, and G. Lonzarich, Physica C: Superconductivity **282-287**, 303 (1997).

[157] N. D. Mathur, F. M. Grosche, S. R. Julian, I. R. Walker, D. M. Freye, R. K. W. Haselwimmer, and G. G. Lonzarich, Nature **394**, 39 (1998).

[158] G. Knebel, D. Braithwaite, P. C. Canfield, G. Lapertot, and J. Flouquet, Phys. Rev. B **65**, 024425 (2001).

[159] S. Kawasaki, T. Mito, Y. Kawasaki, H. Kotegawa, G.-Q. Zheng, Y. Kitaoka, H. Shishido, S. Araki, R. Settai, and Y. Ōnuki, Journal of the Physical Society of Japan **73**, 1647 (2004).

[160] S. E. Sebastian, N. Harrison, C. D. Batista, S. A. Trugman, V. Fanelli, M. Jaime, T. P. Murphy, E. C. Palm, H. Harima, and T. Ebihara, Proceedings of the National Academy of Sciences of the United States of America **106**, 7741 (2008).

[161] T. Ebihara, N. Harrison, M. Jaime, S. Uji, and J. C. Lashley, Phys. Rev. Lett. **93**, 246401 (2004).

[162] N. Harrison, S. E. Sebastian, C. H. Mielke, A. Paris, M. J. Gordon, C. A. Swenson, D. G. Rickel, M. D. Pacheco, P. F. Ruminer, J. B. Schillig, J. R. Sims, A. H. Lacerda, M.-T. Suzuki, H. Harima, and T. Ebihara, Phys. Rev. Lett. **99**, 056401 (2007).

[163] P. J. W. Moll, T. Helm, S.-S. Zhang, C. D. Batista, N. Harrison, R. D. McDonald, L. E. Winter, B. J. Ramshaw, M. K. Chan, F. F. Balakirev, B. Batlogg, E. D. Bauer, and F. Ronning, npj Quantum Materials **2**, 46 (2017).

[164] Y. Tokunaga, A. Orlova, N. Bruyant, D. Aoki, H. Mayaffre, S. Krämer, M.-H. Julien, C. Berthier, M. Horvatić, N. Higa, T. Hattori, H. Sakai, S. Kambe, and I. Sheikin, Phys. Rev. B **99**, 085142 (2019).

[165] R. Elenbaas, C. Schinkel, and C. van Deudekom, Journal of Magnetism and Magnetic Materials **15-18**, 979 (1980).

[166] Pedrazzini, P., Gómez Berisso, M., Caroca-Canales, N., Deppe, M., Geibel, C., and Sereni, J. G., Eur. Phys. J. B **38**, 445 (2004).

[167] Y. Iwamoto, T. Ebihara, N. Harrison, M. Jaime, A. Silhanek, K. Tezuka, K. Morishita, T. Terashima, and A. Iyo, Journal of Magnetism and Magnetic Materials **310**, 300 (2007).

[168] E. Bittar, J. Duque, P. Venegas, C. Rettori, and P. Pagliuso, Physica B: Condensed Matter **404**, 2995 (2009).

[169] N. Berry, E. M. Bittar, C. Capan, P. G. Pagliuso, and Z. Fisk, Phys. Rev. B **81**, 174413 (2010).

[170] M. B. T. Tchokonté, K. G. Tshabalala, P. de Villiers du Plessis, and D. Kaczorowski, Journal of Physics and Chemistry of Solids **71**, 181 (2010).

[171] E. M. Bittar, C. Adriano, C. Giles, C. Rettori, Z. Fisk, and P. G. Pagliuso, Phys. Rev. B **86**, 125108 (2012).

[172] D. Stauffer and A. Aharony, *Introduction to Percolation Theory*, 2nd ed. (Taylor & Francis, 1992).

[173] K. Kato, S. Todo, K. Harada, N. Kawashima, S. Miyashita, and H. Takayama, Phys. Rev. Lett. **84**, 4204 (2000).

[174] H. Jin, J. Badger, P. Klavins, J.-T. Zhao, and V. Taufour, Journal of Alloys and Compounds **863**, 158354 (2021).

[175] K. P. Devlin, N. Kazem, J. V. Zaikina, J. A. Cooley, J. R. Badger, J. C. Fettinger, V. Taufour, and S. M. Kauzlarich, Chemistry of Materials **30**, 7067 (2018).

[176] P. C. Canfield and Z. Fisk, Philos. Mag. B-Phys. Condens. Matter Stat. Mech. Electron. Opt. Magn. Prop. **65**, 1117 (1992).

[177] P. C. Canfield and I. R. Fisher, Journal of Crystal Growth **225**, 155 (2001).

[178] M. G. Kanatzidis, R. Pöttgen, and W. Jeitschko, Angewandte Chemie International Edition **44**, 6996 (2005).

[179] E. L. Thomas, J. N. Millican, E. K. Okudzeto, and J. Y. Chan, Comments on Inorganic Chemistry **27**, 1 (2006).

[180] W. A. Phelan, M. C. Menard, M. J. Kangas, G. T. McCandless, B. L. Drake, and J. Y. Chan, Chemistry of Materials **24**, 409 (2012).

[181] M. Tachibana, Mechanisms of crystal growth from fluxed solutions, in *Beginner's Guide to Flux Crystal Growth* (Springer Japan, Tokyo, 2017) pp. 23–41.

[182] H. Okamoto, M. Schlesinger, and E. Mueller, *Alloy Phase Diagrams* (ASM International, 2016).

[183] S. B. Zhang, Y. P. Sun, X. D. Zhu, X. B. Zhu, B. S. Wang, G. Li, H. C. Lei, X. Luo, Z. R. Yang, W. H. Song, and J. M. Dai, Superconductor Science and Technology **22**, 015020 (2009).

[184] D. Braithwaite, B. Salce, G. Lapertot, F. Bourdarot, C. Marin, D. Aoki, and M. Hanfland, Journal of Physics: Condensed Matter **21**, 232202 (2009).

[185] R. Hu, H. Lei, M. Abeykoon, E. S. Bozin, S. J. L. Billinge, J. B. Warren, T. Siegrist, and C. Petrovic, Phys. Rev. B **83**, 224502 (2011).

[186] P. C. Canfield, T. Kong, U. S. Kaluarachchi, and N. H. Jo, Philosophical Magazine **96**, 84 (2016).

[187] U. Patel, J. Hua, S. H. Yu, S. Avci, Z. L. Xiao, H. Claus, J. Schlueter, V. V. Vlasko-Vlasov, U. Welp, and W. K. Kwok, Applied Physics Letters **94**, 082508 (2009).

[188] Y. Hara, K. Takase, A. Yamasaki, H. Sato, N. Miyakawa, N. Umeyama, and S. Ikeda, Physica C: Superconductivity and its Applications **470**, S313 (2010).

[189] A. E. Böhmer, F. Hardy, F. Eilers, D. Ernst, P. Adelmann, P. Schweiss, T. Wolf, and C. Meingast, Phys. Rev. B **87**, 180505 (2013).

[190] S. Karlsson, P. Strobel, A. Sulpice, C. Marcenat, M. Legendre, F. Gay, S. Pairis, O. Leynaud, and P. Toulemonde, Superconductor Science and Technology **28**, 105009 (2015).

[191] A. E. Böhmer, V. Taufour, W. E. Straszheim, T. Wolf, and P. C. Canfield, Physical Review B **94**, 024526 (2016).

[192] S. Bae, H. Kim, Y. S. Eo, S. Ran, I.-l. Liu, W. T. Fuhrman, J. Paglione, N. P. Butch, and S. M. Anlage, Nature Communications **12**, 2644 (2021).

[193] I. Vinograd, S. P. Edwards, Z. Wang, T. Kissikov, J. K. Byland, J. R. Badger, V. Taufour, and N. J. Curro, Phys. Rev. B **104**, 014502 (2021).

[194] R. Gruehn and R. Glaum, Angewandte Chemie International Edition **39**, 692 (2000).

[195] M. Binnewies, R. Glaum, M. Schmidt, and P. Schmidt, Zeitschrift für anorganische und allgemeine Chemie **639**, 219 (2013).

[196] P. Schmidt, M. Binnewies, R. Glaum, and M. Schmidt, in *Advanced Topics on Crystal Growth*, edited by S. O. Ferreira (IntechOpen, 2013) Chap. 9.

[197] M. Binnewies, M. Schmidt, and P. Schmidt, Zeitschrift für anorganische und allgemeine Chemie **643**, 1295 (2017).

[198] D. A. Chareev, Journal of Crystal Growth **429**, 63 (2015).

[199] D. Chareev, O. Volkova, N. Geringer, A. Koshelev, A. Nekrasov, V. Osadchii, E. Osadchii, and O. Filimonova, Crystallography Reports **61**, 682 (2016).

[200] D. A. Chareev, Crystallography Reports **61**, 506 (2016).

[201] D. A. Chareev, V. O. Osadchii, A. A. Shiryaev, A. N. Nekrasov, A. V. Koshelev, and E. G. Osadchii, Physics and Chemistry of Minerals **44**, 287 (2017).

[202] J.-Q. Yan, B. C. Sales, M. A. Susner, and M. A. McGuire, Phys. Rev. Materials **1**, 023402 (2017).

[203] M. Ladd and T. Palmer, *Structure Determination by X-ray Crystallography* (Springer, 2013).

[204] V. V. Gurzhiy, in *Materials Characterization* (ASM International, 2019).

[205] P. Luger, *Modern X-ray analysis on single crystals : a practical guide* (De Gruyter, 2014).

[206] W. Clegg, A. J. Blake, J. M. Cole, J. S. O. Evans, P. Main, S. Parsons, and D. J. Watkin, *Crystal Structure Analysis: Principles and Practice* (Oxford, 2009).

[207] P. Müller, R. Herbst-Irmer, A. L. Spek, T. R. Schneider, and M. R. Sawaya, *Crystal Structure Refinement: A Crystallographer's Guide to SHELXL* (Oxford University Press, 2006) p. 232.

[208] A. R. Denton and N. W. Ashcroft, Phys. Rev. A **43**, 3161 (1991).

[209] Y. Yarmolyuk and Y. Grin, Dopovidi Akademii nauk Ukrainskoi RSR, Seriya A: Fiziko-Matematichni ta Tekhnichni Nauki **44**, 71 (1982).

[210] N. L. Zeng and W. H. Lee, Phys. Rev. B **66**, 092503 (2002).

[211] W. contributors, Band filling diagram (2020), Wikimedia Commons:https://en.wikipedia.org/wiki/Electrical_resistivity_and_conductivity .

[212] J. Bass, W. P. Pratt, and P. A. Schroeder, Rev. Mod. Phys. **62**, 645 (1990).

[213] D. Cvijović, Theoretical and Mathematical Physics **166**, 37 (2011).

[214] A. H. Wilson, Proceedings of the Royal Society of London. Series A. Mathematical and Physical Sciences **167**, 580 (1938).

[215] P. Noziéres and D. Pines, *The theory of quantum liquids* (Perseus Books, Cambridge, Mass., 1999).

[216] F.-C. Hsu, J.-Y. Luo, K.-W. Yeh, T.-K. Chen, T.-W. Huang, P. M. Wu, Y.-C. Lee, Y.-L. Huang, Y.-Y. Chu, D.-C. Yan, and M.-K. Wu, Proceedings of the National Academy of Sciences **105**, 14262 (2008).

[217] S. Medvedev, T. M. McQueen, I. A. Troyan, T. Palasyuk, M. I. Eremets, R. J. Cava, S. Naghavi, F. Casper, V. Ksenofontov, G. Wortmann, and C. Felser, Nature Materials **8**, 630 (2009).

[218] S. Margadonna, Y. Takabayashi, Y. Ohishi, Y. Mizuguchi, Y. Takano, T. Kagayama, T. Nakagawa, M. Takata, and K. Prassides, Physical Review B **80**, 064506 (2009).

[219] W. contributors, Resistivity geometry (2021), Wikimedia Commons:https://en.wikipedia.org/wiki/Electrical_resistivity_and_conductivity .

[220] E. Gopal, *Specific heats at low temperatures*, International cryogenics monograph series (Plenum Press, New York, 1966).

[221] V. H. Tran and M. Sahakyan, Scientific Reports **7**, 15769 (2017).

[222] D. L. Decker, D. E. Mapother, and R. W. Shaw, Phys. Rev. **112**, 1888 (1958).

[223] J. R. Badger, Y. Quan, M. C. Staab, S. Sumita, A. Rossi, K. P. Devlin, K. Neubauer, D. S. Shulman, J. C. Fettinger, P. Klavins, S. M. Kauzlarich, D. Aoki, I. M. Vishik, W. E. Pickett, and V. Taufour, Dirac lines and loop at the fermi level in the time-reversal symmetry breaking superconductor laniga$_2$ (2021), arXiv:2109.06983 [cond-mat.supr-con] .

[224] S. J. Blundell, Contemporary Physics **40**, 175 (1999).

[225] R. S. Hayano, Y. J. Uemura, J. Imazato, N. Nishida, T. Yamazaki, and R. Kubo, Phys. Rev. B **20**, 850 (1979).

[226] E. M. Levenson-Falk, E. R. Schemm, Y. Aoki, M. B. Maple, and A. Kapitulnik, Phys. Rev. Lett. **120**, 187004 (2018).

[227] G. M. Luke, Y. Fudamoto, K. M. Kojima, M. I. Larkin, J. Merrin, B. Nachumi, Y. J. Uemura, Y. Maeno, Z. Q. Mao, Y. Mori, H. Nakamura, and M. Sigrist, Nature **394**, 558 (1998).

[228] A. P. Mackenzie, T. Scaffidi, C. W. Hicks, and Y. Maeno, npj Quantum Materials **2**, 40 (2017).

[229] G. M. Luke, A. Keren, L. P. Le, W. D. Wu, Y. J. Uemura, D. A. Bonn, L. Taillefer, and J. D. Garrett, Phys. Rev. Lett. **71**, 1466 (1993).

[230] P. Neha, P. K. Biswas, T. Das, and S. Patnaik, Phys. Rev. Materials **3**, 074201 (2019).

[231] A. D. Hillier, J. Quintanilla, and R. Cywinski, Phys. Rev. Lett. **102**, 117007 (2009).

[232] S. K. Ghosh, G. Csire, P. Whittlesea, J. F. Annett, M. Gradhand, B. Újfalussy, and J. Quintanilla, Phys. Rev. B **101**, 100506 (2020).

[233] E. Makarov and V. Bykov, Kristallografiya **4**, 183 (1959).

[234] K. Oikawa, T. Kamiyama, H. Asano, Y. Ōnuki, and M. Kohgi, Journal of the Physical Society of Japan **65**, 3229 (1996).

[235] P. Boulet, A. Daoudi, M. Potel, H. Noel, G. M. Gross, G. Andre, and F. Bouree, J. Alloy. Compd. **247**, 104 (1997).

[236] Q.-F. Liang, J. Zhou, R. Yu, Z. Wang, and H. Weng, Phys. Rev. B **93**, 085427 (2016).

[237] N. B. Kopnin and M. M. Salomaa, Phys. Rev. B **44**, 9667 (1991).

[238] N. Read and D. Green, Phys. Rev. B **61**, 10267 (2000).

[239] G. E. Volovik and V. M. Yakovenko, Journal of Physics: Condensed Matter **1**, 5263 (1989).

[240] A. Kitaev, Annals of Physics **303**, 2 (2003).

[241] V. Mourik, K. Zuo, S. M. Frolov, S. R. Plissard, E. P. A. M. Bakkers, and L. P. Kouwenhoven, Science **336**, 1003 (2012).

[242] S. Nadj-Perge, I. K. Drozdov, J. Li, H. Chen, S. Jeon, J. Seo, A. H. MacDonald, B. A. Bernevig, and A. Yazdani, Science **346**, 602 (2014).

[243] V. Fatemi, S. Wu, Y. Cao, L. Bretheau, Q. D. Gibson, K. Watanabe, T. Taniguchi, R. J. Cava, and P. Jarillo-Herrero, Science **362**, 926 (2018).

[244] E. Sajadi, T. Palomaki, Z. Fei, W. Zhao, P. Bement, C. Olsen, S. Luescher, X. Xu, J. A. Folk, and D. H. Cobden, Science **362**, 922 (2018).

[245] F. Kidwingira, J. D. Strand, D. J. Van Harlingen, and Y. Maeno, Science **314**, 1267 (2006).

[246] A. Pustogow, Y. Luo, A. Chronister, Y.-S. Su, D. A. Sokolov, F. Jerzembeck, A. P. Mackenzie, C. W. Hicks, N. Kikugawa, S. Raghu, E. D. Bauer, and S. E. Brown, Nature **574**, 72 (2019).

[247] V. Romaka, Y. Grin, Y. Yarmolyuk, R. Skolozdra, and A. Jartys, Ukrains'kii Fizichnii Zhurnal **28**, 227 (1983).

[248] B. H. Toby and R. B. Von Dreele, Journal of Applied Crystallography **46**, 544 (2013).

[249] R. J. Goetsch, V. K. Anand, A. Pandey, and D. C. Johnston, Phys. Rev. B **85**, 054517 (2012).

[250] A. Nakamura, F. Honda, Y. Homma, D. Li, K. Nishimura, M. Kakihana, M. Hedo, T. Nakama, Y. Ōnuki, and D. Aoki, Journal of Physics: Conference Series **807**, 052012 (2017).

[251] N. Mott, Advances in Physics **13**, 325 (1964).

[252] K. Kadowaki and S. Woods, Solid State Communications **58**, 507 (1986).

[253] A. C. Jacko, J. O. Fjærestad, and B. J. Powell, Nature Physics **5**, 422 (2009).

[254] E. Helfand and N. R. Werthamer, Phys. Rev. **147**, 288 (1966).

[255] A. M. Clogston, Phys. Rev. Lett. **9**, 266 (1962).

[256] M. Tinkham, *Introduction to superconductivity* (McGraw-Hill New York, 1975).

[257] D. J. Singh, Phys. Rev. B **86**, 174507 (2012).

[258] A. Damascelli, Physica Scripta **T109**, 61 (2004).

[259] P. B. Allen and W. E. Pickett, Physica C: Superconductivity and its Applications **549**, 102 (2018).

172

[260] C. Herring, Phys. Rev. **52**, 365 (1937).

[261] H.-S. Jin, Y.-J. Song, W. E. Pickett, and K.-W. Lee, Phys. Rev. Materials **3**, 021201 (2019).

[262] Y. Yanase, Phys. Rev. B **94**, 174502 (2016).

[263] A. M. Black-Schaffer and C. Honerkamp, Journal of Physics: Condensed Matter **26**, 423201 (2014).

[264] S. Kobayashi and M. Sato, Phys. Rev. Lett. **115**, 187001 (2015).

[265] G. Csire, B. Újfalussy, and J. F. Annett, The European Physical Journal B **91**, 217 (2018).

[266] S. Sundar, S. R. Dunsiger, S. Gheidi, K. S. Akella, A. M. Côté, H. U. Özdemir, N. R. Lee-Hone, D. M. Broun, E. Mun, F. Honda, Y. J. Sato, T. Koizumi, R. Settai, Y. Hirose, I. Bonalde, and J. E. Sonier, Phys. Rev. B **103**, 014511 (2021).

[267] A. Subedi and D. J. Singh, Phys. Rev. B **80**, 092506 (2009).

[268] J. Laverock, T. D. Haynes, C. Utfeld, and S. B. Dugdale, Phys. Rev. B **80**, 125111 (2009).

[269] I. Hase and T. Yanagisawa, Journal of the Physical Society of Japan **78**, 084724 (2009).

[270] T. Yanagisawa and I. Hase, Journal of the Physical Society of Japan **81**, SB039 (2012).

[271] B. Wiendlocha, R. Szczęśniak, A. P. Durajski, and M. Muras, Phys. Rev. B **94**, 134517 (2016).

[272] Y. Zhang, T. Usman, X.-m. Tao, and M.-q. Tan, Journal of Superconductivity and Novel Magnetism **31**, 995 (2018).

[273] S. Katano, H. Nakagawa, K. Matsubayashi, Y. Uwatoko, H. Soeda, T. Tomita, and H. Takahashi, Phys. Rev. B **90**, 220508 (2014).

[274] J. F. Landaeta, D. Subero, P. Machado, F. Honda, and I. Bonalde, Phys. Rev. B **96**, 174515 (2017).

[275] F. Levy, I. Sheikin, and A. Huxley, Nat. Phys. **3**, 460 (2007).

[276] G. Knebel, W. Knafo, A. Pourret, Q. Niu, M. Vališka, D. Braithwaite, G. Lapertot, M. Nardone, A. Zitouni, S. Mishra, I. Sheikin, G. Seyfarth, J.-P. Brison, D. Aoki, and J. Flouquet, Journal of the Physical Society of Japan **88**, 063707 (2019).

[277] B. S. Shivaram, T. F. Rosenbaum, and D. G. Hinks, Phys. Rev. Lett. **57**, 1259 (1986).

[278] Y. Yanase and K. Shiozaki, Phys. Rev. B **95**, 224514 (2017).

[279] W. Meng, Y. Liu, X. Zhang, X. Dai, and G. Liu, Phys. Chem. Chem. Phys. **22**, 22399 (2020).

[280] Z.-M. Yu, Z. Zhang, G.-B. Liu, W. Wu, X.-P. Li, R.-W. Zhang, S. A. Yang, and Y. Yao, Encyclopedia of emergent particles in three-dimensional crystals (2021), arXiv:2102.01517 [cond-mat.mes-hall] .

[281] B. Chevalier, P. Lejay, J. Etourneau, and P. Hagenmuller, Materials Research Bulletin **18**, 315 (1983).

[282] M. J. Winiarski, B. Wiendlocha, S. Gołąb, S. K. Kushwaha, P. Wiśniewski, D. Kaczorowski, J. D. Thompson, R. J. Cava, and T. Klimczuk, Phys. Chem. Chem. Phys. **18**, 21737 (2016).

[283] N. Zaki, G. Gu, A. Tsvelik, C. Wu, and P. D. Johnson, Proceedings of the National Academy of Sciences **118** (2021).

[284] D. T. Adroja, A. Bhattacharyya, M. Telling, Y. Feng, M. Smidman, B. Pan, J. Zhao, A. D. Hillier, F. L. Pratt, and A. M. Strydom, Phys. Rev. B **92**, 134505 (2015).

[285] E. R. Schemm, W. J. Gannon, C. M. Wishne, W. P. Halperin, and A. Kapitulnik, Science **345**, 190 (2014).

[286] K. E. Avers, W. J. Gannon, S. J. Kuhn, W. P. Halperin, J. A. Sauls, L. DeBeer-Schmitt, C. D. Dewhurst, J. Gavilano, G. Nagy, U. Gasser, and M. R. Eskildsen, Nature Physics **16**, 531 (2020).

[287] M. Lee, G. F. Moores, Y.-Q. Song, W. P. Halperin, W. W. Kim, and G. R. Stewart, Phys. Rev. B **48**, 7392 (1993).

[288] G. Aeppli, E. Bucher, C. Broholm, J. K. Kjems, J. Baumann, and J. Hufnagl, Phys. Rev. Lett. **60**, 615 (1988).

[289] S. M. Hayden, L. Taillefer, C. Vettier, and J. Flouquet, Phys. Rev. B **46**, 8675 (1992).

[290] S.-i. Fujimori, Y. Takeda, T. Okane, Y. Saitoh, A. Fujimori, H. Yamagami, Y. Haga, E. Yamamoto, and Y. Ōnuki, Journal of the Physical Society of Japan **85**, 062001 (2016).

[291] P. M. Oppeneer, J. Rusz, S. Elgazzar, M.-T. Suzuki, T. Durakiewicz, and J. A. Mydosh, Phys. Rev. B **82**, 205103 (2010).

174

[292] P. M. Oppeneer, S. Elgazzar, J. Rusz, Q. Feng, T. Durakiewicz, and J. A. Mydosh, Phys. Rev. B **84**, 241102 (2011).

[293] T. Das, Scientific Reports **2**, 596 (2012).

[294] J.-Q. Meng, P. M. Oppeneer, J. A. Mydosh, P. S. Riseborough, K. Gofryk, J. J. Joyce, E. D. Bauer, Y. Li, and T. Durakiewicz, Phys. Rev. Lett. **111**, 127002 (2013).

[295] T. Shishidou, H. G. Suh, P. M. R. Brydon, M. Weinert, and D. F. Agterberg, Phys. Rev. B **103**, 104504 (2021).

[296] Y. Tokunaga, H. Sakai, S. Kambe, T. Hattori, N. Higa, G. Nakamine, S. Kitagawa, K. Ishida, A. Nakamura, Y. Shimizu, Y. Homma, D. Li, F. Honda, and D. Aoki, Journal of the Physical Society of Japan **88**, 073701 (2019).

[297] S. Sundar, S. Gheidi, K. Akintola, A. M. Côté, S. R. Dunsiger, S. Ran, N. P. Butch, S. R. Saha, J. Paglione, and J. E. Sonier, Phys. Rev. B **100**, 140502 (2019).

[298] I. M. Hayes, D. S. Wei, T. Metz, J. Zhang, Y. S. Eo, S. Ran, S. R. Saha, J. Collini, N. P. Butch, D. F. Agterberg, A. Kapitulnik, and J. Paglione, Weyl superconductivity in ute$_2$ (2020), arXiv:2002.02539 [cond-mat.str-el] .

[299] Y. Qian, S. Nie, C. Yi, L. Kong, C. Fang, T. Qian, H. Ding, Y. Shi, Z. Wang, H. Weng, and Z. Fang, npj Computational Materials **5**, 121 (2019).

[300] Y. Gao, J.-F. Zhang, S. A. Yang, K. Liu, and Z.-Y. Lu, Phys. Rev. B **103**, 125154 (2021).

[301] L. Jin, X. Zhang, T. He, W. Meng, X. Dai, and G. Liu, J. Mater. Chem. C **7**, 10694 (2019).

[302] L. Muechler, Z. Guguchia, J.-C. Orain, J. Nuss, L. M. Schoop, R. Thomale, and F. O. von Rohr, APL Materials **7**, 121103 (2019).

[303] C. Q. Xu, B. Li, J. J. Feng, W. H. Jiao, Y. K. Li, S. W. Liu, Y. X. Zhou, R. Sankar, N. D. Zhigadlo, H. B. Wang, Z. D. Han, B. Qian, W. Ye, W. Zhou, T. Shiroka, P. K. Biswas, X. Xu, and Z. X. Shi, Phys. Rev. B **100**, 134503 (2019).

[304] P. Szabó, P. Samuely, J. Kačmarčík, T. Klein, J. Marcus, D. Fruchart, S. Miraglia, C. Marcenat, and A. G. M. Jansen, Phys. Rev. Lett. **87**, 137005 (2001).

[305] K. Funada, A. Yamakage, N. Yamashina, and H. Kageyama, Journal of the Physical Society of Japan **88**, 044711 (2019).

[306] A. Ikeda, M. Kawaguchi, S. Koibuchi, T. Hashimoto, T. Kawakami, S. Yonezawa, M. Sato, and Y. Maeno, Phys. Rev. Materials **4**, 041801 (2020).

[307] D.-Y. Chen, Y. Wu, L. Jin, Y. Li, X. Wang, J. Duan, J. Han, X. Li, Y.-Z. Long, X. Zhang, D. Chen, and B. Teng, Phys. Rev. B **100**, 064516 (2019).

[308] W. Chen, L. Liu, W. Yang, D. Chen, Z. Liu, Y. Huang, T. Zhang, H. Zhang, Z. Liu, and D. W. Shen, Phys. Rev. B **103**, 035133 (2021).

[309] J. J. Gao, J. G. Si, X. Luo, J. Yan, Z. Z. Jiang, W. Wang, C. Q. Xu, X. F. Xu, P. Tong, W. H. Song, X. B. Zhu, W. J. Lu, and Y. P. Sun, The Journal of Physical Chemistry C **124**, 6349 (2020).

[310] C. N. Veenstra, Z.-H. Zhu, B. Ludbrook, M. Capsoni, G. Levy, A. Nicolaou, J. A. Rosen, R. Comin, S. Kittaka, Y. Maeno, I. S. Elfimov, and A. Damascelli, Phys. Rev. Lett. **110**, 097004 (2013).

[311] C. Q. Han, H. Li, W. J. Chen, F. Zhu, M.-Y. Yao, Z. J. Li, M. Wang, B. F. Gao, D. D. Guan, C. Liu, C. L. Gao, D. Qian, and J.-F. Jia, Applied Physics Letters **107**, 171602 (2015).

[312] Y. Tanaka, Z. Ren, T. Sato, K. Nakayama, S. Souma, T. Takahashi, K. Segawa, and Y. Ando, Nature Physics **8**, 800 (2012).

[313] E. Lahoud, E. Maniv, M. S. Petrushevsky, M. Naamneh, A. Ribak, S. Wiedmann, L. Petaccia, Z. Salman, K. B. Chashka, Y. Dagan, and A. Kanigel, Phys. Rev. B **88**, 195107 (2013).

[314] K. Kobayashi, T. Ueno, H. Fujiwara, T. Yokoya, and J. Akimitsu, Phys. Rev. B **95**, 180503 (2017).

[315] D. Das, K. Kobayashi, M. P. Smylie, C. Mielke, T. Takahashi, K. Willa, J.-X. Yin, U. Welp, M. Z. Hasan, A. Amato, H. Luetkens, and Z. Guguchia, Phys. Rev. B **102**, 134514 (2020).

[316] C. X. Trang, Z. Wang, D. Takane, K. Nakayama, S. Souma, T. Sato, T. Takahashi, A. A. Taskin, and Y. Ando, Phys. Rev. B **93**, 241103 (2016).

[317] K. Dimitri, M. M. Hosen, G. Dhakal, H. Choi, F. Kabir, C. Sims, D. Kaczorowski, T. Durakiewicz, J.-X. Zhu, and M. Neupane, Phys. Rev. B **97**, 144514 (2018).

[318] Z. Sun, M. Enayat, A. Maldonado, C. Lithgow, E. Yelland, D. C. Peets, A. Yaresko, A. P. Schnyder, and P. Wahl, Nature Communications **6**, 6633 (2015).

[319] A. Pramanik, R. P. Pandeya, D. V. Vyalikh, A. Generalov, P. Moras, A. K. Kundu, P. M. Sheverdyaeva, C. Carbone, B. Joshi, A. Thamizhavel, S. Ramakrishnan, and K. Maiti, Phys. Rev. B **103**, 155401 (2021).

[320] P. K. Biswas, D. G. Mazzone, R. Sibille, E. Pomjakushina, K. Conder, H. Luetkens, C. Baines, J. L. Gavilano, M. Kenzelmann, A. Amato, and E. Morenzoni, Phys. Rev. B **93**, 220504 (2016).

[321] P. Zhang, Z. Wang, X. Wu, K. Yaji, Y. Ishida, Y. Kohama, G. Dai, Y. Sun, C. Bareille, K. Kuroda, T. Kondo, K. Okazaki, K. Kindo, X. Wang, C. Jin, J. Hu, R. Thomale, K. Sumida, S. Wu, K. Miyamoto, T. Okuda, H. Ding, G. D. Gu, T. Tamegai, T. Kawakami, M. Sato, and S. Shin, Nature Physics **15**, 41 (2019).

[322] P. K. Biswas, G. Balakrishnan, D. M. Paul, C. V. Tomy, M. R. Lees, and A. D. Hillier, Phys. Rev. B **81**, 092510 (2010).

[323] J. D. Wright, M. J. Pitcher, W. Trevelyan-Thomas, T. Lancaster, P. J. Baker, F. L. Pratt, S. J. Clarke, and S. J. Blundell, Phys. Rev. B **88**, 060401 (2013).

[324] Q. Liu, C. Chen, T. Zhang, R. Peng, Y.-J. Yan, C.-H.-P. Wen, X. Lou, Y.-L. Huang, J.-P. Tian, X.-L. Dong, G.-W. Wang, W.-C. Bao, Q.-H. Wang, Z.-P. Yin, Z.-X. Zhao, and D.-L. Feng, Phys. Rev. X **8**, 041056 (2018).

[325] W. Liu, L. Cao, S. Zhu, L. Kong, G. Wang, M. Papaj, P. Zhang, Y.-B. Liu, H. Chen, G. Li, F. Yang, T. Kondo, S. Du, G.-H. Cao, S. Shin, L. Fu, Z. Yin, H.-J. Gao, and H. Ding, Nature Communications **11**, 5688 (2020).

[326] Y. Li, Z. Wu, J. Zhou, K. Bu, C. Xu, L. Qiao, M. Li, H. Bai, J. Ma, Q. Tao, C. Cao, Y. Yin, and Z.-A. Xu, Phys. Rev. B **102**, 224503 (2020).

[327] Y. Li, Y. Wu, C. Xu, N. Liu, J. Ma, B. Lv, G. Yao, Y. Liu, H. Bai, X. Yang, L. Qiao, M. Li, L. Li, H. Xing, Y. Huang, J. Ma, M. Shi, C. Cao, Y. Liu, C. Liu, J. Jia, and Z.-A. Xu, Science Bulletin **66**, 243 (2021).

[328] A. J. S. Machado, N. P. Baptista, B. S. de Lima, N. Chaia, T. W. Grant, L. E. Corrêa, S. T. Renosto, A. C. Scaramussa, R. F. Jardim, M. S. Torikachvili, J. A. Aguiar, O. C. Cigarroa, L. T. F. Eleno, and Z. Fisk, Phys. Rev. B **95**, 144505 (2017).

[329] H. Huang, S. Zhou, and W. Duan, Phys. Rev. B **94**, 121117 (2016).

[330] F. Fei, X. Bo, R. Wang, B. Wu, J. Jiang, D. Fu, M. Gao, H. Zheng, Y. Chen, X. Wang, H. Bu, F. Song, X. Wan, B. Wang, and G. Wang, Phys. Rev. B **96**, 041201 (2017).

177

[331] H.-J. Noh, J. Jeong, E.-J. Cho, K. Kim, B. I. Min, and B.-G. Park, Phys. Rev. Lett. **119**, 016401 (2017).

[332] D. Singh, P. K. Biswas, S. Yoon, C. H. Lee, A. D. Hillier, R. P. Singh, A. Y. Singh, and K. Y. Choi, Coexistence of type-i and type-ii superconductivity in topological superconductor pdte$_2$ (2019), arXiv:1910.13773 [cond-mat.supr-con] .

[333] J. Zhang and G. Q. Huang, Journal of Physics: Condensed Matter **32**, 205702 (2020).

[334] T.-R. Chang, P.-J. Chen, G. Bian, S.-M. Huang, H. Zheng, T. Neupert, R. Sankar, S.-Y. Xu, I. Belopolski, G. Chang, B. Wang, F. Chou, A. Bansil, H.-T. Jeng, H. Lin, and M. Z. Hasan, Phys. Rev. B **93**, 245130 (2016).

[335] P.-J. Chen, T.-R. Chang, and H.-T. Jeng, Phys. Rev. B **94**, 165148 (2016).

[336] G. Bian, T.-R. Chang, R. Sankar, S.-Y. Xu, H. Zheng, T. Neupert, C.-K. Chiu, S.-M. Huang, G. Chang, I. Belopolski, D. S. Sanchez, M. Neupane, N. Alidoust, C. Liu, B. Wang, C.-C. Lee, H.-T. Jeng, C. Zhang, Z. Yuan, S. Jia, A. Bansil, F. Chou, H. Lin, and M. Z. Hasan, Nature Communications **7**, 10556 (2016).

[337] M. N. Wilson, A. M. Hallas, Y. Cai, S. Guo, Z. Gong, R. Sankar, F. C. Chou, Y. J. Uemura, and G. M. Luke, Phys. Rev. B **95**, 224506 (2017).

[338] T. Shang, J. Z. Zhao, D. J. Gawryluk, M. Shi, M. Medarde, E. Pomjakushina, and T. Shiroka, Phys. Rev. B **101**, 214518 (2020).

[339] D. Yan, D. Geng, Q. Gao, Z. Cui, C. Yi, Y. Feng, C. Song, H. Luo, M. Yang, M. Arita, S. Kumar, E. F. Schwier, K. Shimada, L. Zhao, K. Wu, H. Weng, L. Chen, X. J. Zhou, Z. Wang, Y. Shi, and B. Feng, Phys. Rev. B **102**, 205117 (2020).

[340] N.-N. Zhao, P.-J. Guo, X.-Q. Lu, Q. Han, K. Liu, and Z.-Y. Lu, Phys. Rev. B **101**, 195144 (2020).

[341] S. Gupta, R. Juneja, R. Shinde, and A. K. Singh, Journal of Applied Physics **121**, 214901 (2017).

[342] G. Zhang, X. Shi, X. Liu, W. Xia, H. Su, L. Chen, X. Wang, N. Yu, Z. Zou, W. Zhao, and Y. Guo, Chinese Physics Letters **37**, 087101 (2020).

[343] J. A. T. Barker, R. P. Singh, A. D. Hillier, and D. M. Paul, Phys. Rev. B **97**, 094506 (2018).

[344] X.-H. Tu, P.-F. Liu, and B.-T. Wang, Phys. Rev. Materials **3**, 054202 (2019).

[345] K.-W. Chen, X. Lian, Y. Lai, N. Aryal, Y.-C. Chiu, W. Lan, D. Graf, E. Manousakis, R. E. Baumbach, and L. Balicas, Phys. Rev. Lett. **120**, 206401 (2018).

[346] S. Nie, L. Xing, R. Jin, W. Xie, Z. Wang, and F. B. Prinz, Phys. Rev. B **98**, 125143 (2018).

[347] W. Xia, X. Shi, Y. Zhang, H. Su, Q. Wang, L. Ding, L. Chen, X. Wang, Z. Zou, N. Yu, L. Pi, Y. Hao, B. Li, Z. Zhu, W. Zhao, X. Kou, and Y. Guo, Phys. Rev. B **101**, 155117 (2020).

[348] B. Bradlyn, J. Cano, Z. Wang, M. G. Vergniory, C. Felser, R. J. Cava, and B. A. Bernevig, Science **353** (2016).

[349] M. Kim, C.-Z. Wang, and K.-M. Ho, Phys. Rev. B **99**, 224506 (2019).

[350] E. Derunova, Y. Sun, C. Felser, S. S. P. Parkin, B. Yan, and M. N. Ali, Science Advances **5** (2019).

[351] P. V. Sreenivasa Reddy, V. Kanchana, G. Vaitheeswaran, P. Modak, and A. Verma, Journal of Applied Physics **119**, 075901 (2016).

[352] M. I. Naher, F. Parvin, A. K. M. A. Islam, and S. H. Naqib, The European Physical Journal B **91**, 289 (2018).

[353] P. Zhang, H. Yuan, and C. Cao, Phys. Rev. B **101**, 245145 (2020).

[354] K. P. Sajilesh, D. Singh, P. K. Biswas, A. D. Hillier, and R. P. Singh, Phys. Rev. B **98**, 214505 (2018).

[355] K. P. Sajilesh, D. Singh, A. D. Hillier, and R. P. Singh, Phys. Rev. B **102**, 094515 (2020).

[356] Y. L. Chen, Z. K. Liu, J. G. Analytis, J.-H. Chu, H. J. Zhang, B. H. Yan, S.-K. Mo, R. G. Moore, D. H. Lu, I. R. Fisher, S. C. Zhang, Z. Hussain, and Z.-X. Shen, Phys. Rev. Lett. **105**, 266401 (2010).

[357] K. E. Arpino, D. C. Wallace, Y. F. Nie, T. Birol, P. D. C. King, S. Chatterjee, M. Uchida, S. M. Koohpayeh, J.-J. Wen, K. Page, C. J. Fennie, K. M. Shen, and T. M. McQueen, Phys. Rev. Lett. **112**, 017002 (2014).

[358] Z. K. Liu, L. X. Yang, S.-C. Wu, C. Shekhar, J. Jiang, H. F. Yang, Y. Zhang, S.-K. Mo, Z. Hussain, B. Yan, C. Felser, and Y. L. Chen, Nature Communications **7**, 12924 (2016).

[359] M. M. Hosen, G. Dhakal, K. Dimitri, H. Choi, F. Kabir, C. Sims, O. Pavlosiuk, P. Wiśniewski, T. Durakiewicz, J.-X. Zhu, D. Kaczorowski, and M. Neupane, Scientific Reports **10**, 12343 (2020).

[360] T. Bay, M. Jackson, C. Paulsen, C. Baines, A. Amato, T. Orvis, M. Aronson, Y. Huang, and A. de Visser, Solid State Communications **183**, 13 (2014).

[361] W. Al-Sawai, H. Lin, R. S. Markiewicz, L. A. Wray, Y. Xia, S.-Y. Xu, M. Z. Hasan, and A. Bansil, Phys. Rev. B **82**, 125208 (2010).

[362] Y. Nakajima, R. Hu, K. Kirshenbaum, A. Hughes, P. Syers, X. Wang, K. Wang, R. Wang, S. R. Saha, D. Pratt, J. W. Lynn, and J. Paglione, Science Advances **1** (2015).

[363] B. R. Ortiz, L. C. Gomes, J. R. Morey, M. Winiarski, M. Bordelon, J. S. Mangum, I. W. H. Oswald, J. A. Rodriguez-Rivera, J. R. Neilson, S. D. Wilson, E. Ertekin, T. M. McQueen, and E. S. Toberer, Phys. Rev. Materials **3**, 094407 (2019).

[364] B. R. Ortiz, S. M. L. Teicher, Y. Hu, J. L. Zuo, P. M. Sarte, E. C. Schueller, A. M. M. Abeykoon, M. J. Krogstad, S. Rosenkranz, R. Osborn, R. Seshadri, L. Balents, J. He, and S. D. Wilson, Phys. Rev. Lett. **125**, 247002 (2020).

[365] B. R. Ortiz, P. M. Sarte, E. M. Kenney, M. J. Graf, S. M. L. Teicher, R. Seshadri, and S. D. Wilson, Phys. Rev. Materials **5**, 034801 (2021).

[366] M. Saghir, J. A. T. Barker, G. Balakrishnan, A. D. Hillier, and M. R. Lees, Phys. Rev. B **90**, 064508 (2014).

[367] C. M. Polley, V. Jovic, T.-Y. Su, M. Saghir, D. Newby, B. J. Kowalski, R. Jakiela, A. Barcz, M. Guziewicz, T. Balasubramanian, G. Balakrishnan, J. Laverock, and K. E. Smith, Phys. Rev. B **93**, 075132 (2016).

[368] T. M. Schmidt and G. P. Srivastava, physica status solidi (RRL) – Rapid Research Letters **14**, 2000362 (2020).

[369] T. M. Schmidt and G. Srivastava, Computational Materials Science **182**, 109777 (2020).

[370] Y. Sun, S.-C. Wu, M. N. Ali, C. Felser, and B. Yan, Phys. Rev. B **92**, 161107 (2015).

[371] K. Deng, G. Wan, P. Deng, K. Zhang, S. Ding, E. Wang, M. Yan, H. Huang, H. Zhang, Z. Xu, J. Denlinger, A. Fedorov, H. Yang, W. Duan, H. Yao, Y. Wu, S. Fan, H. Zhang, X. Chen, and S. Zhou, Nature Physics **12**, 1105 (2016).

[372] L. Huang, T. M. McCormick, M. Ochi, Z. Zhao, M.-T. Suzuki, R. Arita, Y. Wu, D. Mou, H. Cao, J. Yan, N. Trivedi, and A. Kaminski, Nature Materials **15**, 1155 (2016).

[373] J. Jiang, Z. K. Liu, Y. Sun, H. F. Yang, C. R. Rajamathi, Y. P. Qi, L. X. Yang, C. Chen, H. Peng, C.-C. Hwang, S. Z. Sun, S.-K. Mo, I. Vobornik, J. Fujii, S. S. P. Parkin, C. Felser, B. H. Yan, and Y. L. Chen, Nature Communications **8**, 13973 (2017).

[374] C. Xu, N. Wu, G.-X. Zhi, B.-H. Lei, X. Duan, F. Ning, C. Cao, and Q. Chen, npj Computational Materials **6**, 30 (2020).

[375] C. Mondal, C. K. Barman, B. Pathak, and A. Alam, Phys. Rev. B **100**, 245151 (2019).

[376] P.-J. Guo, H.-C. Yang, K. Liu, and Z.-Y. Lu, Phys. Rev. B **95**, 155112 (2017).

[377] H. Saadaoui, T. Shiroka, A. Amato, C. Baines, H. Luetkens, E. Pomjakushina, V. Pomjakushin, J. Mesot, M. Pikulski, and E. Morenzoni, Phys. Rev. B **88**, 094518 (2013).

[378] P.-J. Guo, J.-F. Zhang, H.-C. Yang, Z.-X. Liu, K. Liu, and Z.-Y. Lu, Lnpd$_2$sn (ln=sc, y, lu) class of heusler alloys for topological superconductivity (2018), arXiv:1811.06401 [cond-mat.mtrl-sci] .

[379] P. Gegenwart, Q. Si, and F. Steglich, Nature Physics **4**, 186 (2008).

[380] T. Park, Y. Tokiwa, F. Ronning, H. Lee, E. D. Bauer, R. Movshovich, and J. D. Thompson, physica status solidi (b) **247**, 553 (2010).

[381] Y.-f. Yang, D. Pines, and G. Lonzarich, Proceedings of the National Academy of Sciences **114**, 6250 (2017).

[382] D. Jaccard, H. Wilhelm, K. Alami-Yadri, and E. Vargoz, Physica B: Condensed Matter **259-261**, 1 (1999).

[383] A. T. Holmes, D. Jaccard, and K. Miyake, Phys. Rev. B **69**, 024508 (2004).

[384] M. Nicklas, R. Borth, E. Lengyel, P. G. Pagliuso, J. L. Sarrao, V. A. Sidorov, G. Sparn, F. Steglich, and J. D. Thompson, Journal of Physics: Condensed Matter **13**, L905 (2001).

[385] Y. Takaesu, N. Aso, Y. Tamaki, M. Hedo, T. Nakama, K. Uchima, Y. Ishikawa, K. Deguchi, and N. K. Sato, Journal of Physics: Conference Series **273**, 012058 (2011).

[386] E. Bauer, N. Moreno, D. Mixson, J. Sarrao, J. Thompson, M. Hundley, R. Movshovich, and P. Pagliuso, Physica B: Condensed Matter **359-361**, 35 (2005).

[387] Y. P. Singh, D. J. Haney, I. K. Lum, B. D. White, M. B. Maple, M. Dzero, and C. C. Almasan, Journal of Physics: Conference Series **592**, 012078 (2015).

[388] N. Pouse, S. Jang, B. D. White, S. Ran, R. B. Adhikari, C. C. Almasan, and M. B. Maple, Phys. Rev. B **97**, 235149 (2018).

[389] M. Lavagna, C. Lacroix, and M. Cyrot, Journal of Physics F: Metal Physics **12**, 745 (1982).

[390] A. V. Diepen, R. Craig, and W. Wallage, Journal of Physics and Chemistry of Solids **32**, 1867 (1971).

[391] A. Czopnik, N. Iliew, B. Staliński, C. Bazan, H. Mädge, and R. Pott, Physica B+C **130**, 259 (1985).

[392] M. Amara, R. Galéra, P. Morin, J. Voiron, and P. Burlet, Journal of Magnetism and Magnetic Materials **131**, 402 (1994).

[393] E. G. Moshopoulou, R. M. Ibberson, J. L. Sarrao, J. D. Thompson, and Z. Fisk, Acta Crystallographica Section B **62**, 173 (2006).

[394] I. Harris and G. Raynor, Journal of the Less Common Metals **9**, 7 (1965).

[395] E. D. Bauer, Y.-f. Yang, C. Capan, R. R. Urbano, C. F. Miclea, H. Sakai, F. Ronning, M. J. Graf, A. V. Balatsky, R. Movshovich, A. D. Bianchi, A. P. Reyes, P. L. Kuhns, J. D. Thompson, and Z. Fisk, Proceedings of the National Academy of Sciences **108**, 6857 (2011).

[396] J. D. Thompson, Proceedings of the National Academy of Sciences **108**, 18191 (2011).

[397] R. Hu, Y. Lee, J. Hudis, V. F. Mitrovic, and C. Petrovic, Phys. Rev. B **77**, 165129 (2008).

[398] Y. Kubo, S. Asano, H. Harima, and A. Yanase, Physica B: Condensed Matter **186-188**, 132 (1993).

[399] C. Capan, G. Seyfarth, D. Hurt, A. D. Bianchi, and Z. Fisk, Journal of Physics: Conference Series **273**, 012027 (2011).

[400] M. Shimozawa, T. Watashige, S. Yasumoto, Y. Mizukami, M. Nakamura, H. Shishido, S. K. Goh, T. Terashima, T. Shibauchi, and Y. Matsuda, Phys. Rev. B **86**, 144526 (2012).